# Performance Enhancement of Space-Time Adaptive Processing for GPS and Microstrip Antenna Design Using Ferrite Rings

by

Alix Rivera-Albino

A Dissertation Presented in Partial Fulfillment
of the Requirements for the Degree
Doctor of Philosophy

Approved November 2013 by the
Graduate Supervisory Committee:

Constantine A. Balanis, Chair
Cihan Tepedelenlioglu
Sayfe Kiaei
James T. Aberle

ARIZONA STATE UNIVERSITY

December 2013

# ABSTRACT

Global Positioning System (GPS) is a navigation system widely used in civilian and military application, but its accuracy is highly impacted with consequential fading, and possible loss of communication due to multipath propagation and high power interferences. This dissertation proposes alternatives to improve the performance of the GPS receivers to obtain a system that can be reliable in critical situations. The basic performance of the GPS receiver consists of receiving the signal with an antenna array, delaying the signal at each antenna element, weighting the delayed replicas, and finally, combining the weighted replicas to estimate the desired signal. Based on these, three modifications are proposed to improve the performance of the system. The first proposed modification is the use of the Least Mean Squares (LMS) algorithm with two variations to decrease the convergence time of the classic LMS while achieving good system stability. The results obtained by the proposed LMS demonstrate that the algorithm can achieve the same stability as the classic LMS using a small step size, and its convergence rate is better than the classic LMS using a large step size. The second proposed modification is to replace the uniform distribution of the time delays (or taps) by an exponential distribution that decreases the bit-error rate (BER) of the system without impacting the computational efficiency of the uniform taps. The results show that, for a BER of $10^{-3}$, the system can operate with a 1 to 2 dB lower signal-to-noise ratio (SNR) when an exponential distribution is used rather than a uniform distribution. Finally, the third modification is implemented in the design of the antenna array. In this case, the gain of each microstrip element is enhanced by embedding ferrite rings in the substrate, creating a *hybrid* substrate. The ferrite rings generates constructive interference between the incident and reflected fields; consequently, the gain of a single microstrip element is enhanced by up to 4 dB. When hybrid substrates are used in microstrip element arrays, a significant enhancement in angle range is achieved for a given reflection coefficient compared to using a conventional substrate.

To my husband, Edgar

for the victory of another stage that we conquered together.

ACKNOWLEDGEMENTS

Each step of this beautiful stage of my life has been accompanied by wonderful people who have helped me and given all their support. First, I would like to thank my husband for his patience and unconditional support. Second, thanks to my mom who always believes in me and gives me the support I need. To my father and siblings, thanks for being there with your immeasurable love.

I am especially grateful for my advisor, Dr. Constantine A. Balanis, for the opportunity to be a part of his incredible research group. His advice is an invaluable tool for my professional career. In addition, I would like to thank my committee members, Dr. Cihan Tepedelenlioglu, Dr. James Aberle, and Dr. Sayfe Kiaei for their time.

Thanks to Craig Birtcher for his suggestions and time. Thanks to those who have shared this stage with me and made this time so joyful: Nivia Colon, Manpreet Saini, Victor Kononov, Ahmet Durgun, Nafati Aboserwal, Mikal Askarian Amiri, Wengang Chen, and Sivaseetharaman Pandi.

This work was supported by AFRL/RYDX (Electronics Exploration Branch), Wright-Patterson Air Force Base, Dayton, OH.

TABLE OF CONTENTS

CHAPTER Page

LIST OF TABLES

LIST OF FIGURES

Figure Page

# Chapter 1

# INTRODUCTION

The Global Positioning System, or GPS, is a navigation system widely used in civilian and military applications in which the environment generally has high-power interference and multipath propagation [1], as shown in Figure 1.1. As can be observed from the figure, the signal that the GPS receives is the superposition of different replicas caused by the direct path and three main propagation mechanisms:

- *Reflection*: The signal impinges on a surface with dimensions much larger than a wavelength (e.g., ground)
- *Scattering*: The signal passes through a surface with variations much smaller than the wavelength (e.g., rain and foliage)
- *Diffraction*: The signal bends after impinging on the edge of an object (e.g., a building).

Because of the environment, the accuracy of the system is highly impacted with consequential fading and possible loss of communication. Therefore, this research focuses on improving the GPS signal reception in high-power interference and multipath environments. The motivation is to improve the system performance so that it can be reliable in critical situations, such as in country defense and emergencies.

Several techniques have already been suggested to mitigate interference and multipath environments. These techniques can be grouped into:

- Null steering: The antenna radiation pattern is controlled; it requires an adaptive antenna array that makes the system expensive [2–5].

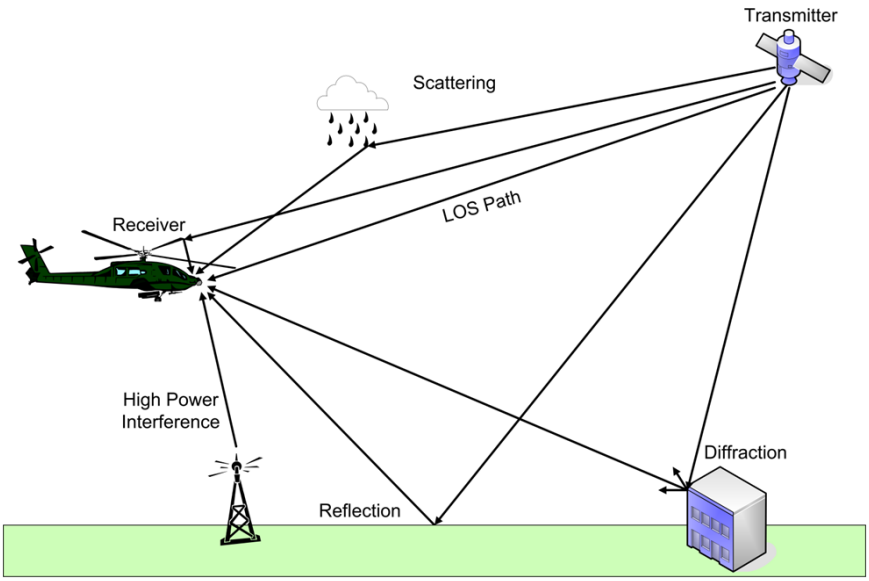


Figure 1.1: GPS communication channel. The received signal at a GPS mounted on a helicopter arrives from multiple trajectories caused by the line-of-sight (LOS), reflection, scattering, and reflection.

- Beam steering: Adaptive arrays control the beam shape; this requires large antenna arrays and electronic packages [6–11].
- Polarization anti-jam: A single aperture technique based on E-field vector cancellation [12].
- Frequency domain filtering: Suppresses narrow band interferences and is a low cost system [13–15].
- Temporal filtering: Suppresses interferences greater than 30 dB and is a low cost method [12].
- Spatial filtering: Each one of the replicas that arrives to the elements undergoes different fading [16].

Recently, combinations of two or more of these methods have become very popular to improve the performance of receivers. Space-Time Adaptive Processing (STAP) is one of

the most commonly used due to its ability to simultaneously null interferers and multipath propagation [17–25]. Therefore, the STAP was selected as the main system configuration for this project.

The next sections will explain the typical space-time processing, its advantages, and the objectives of this research.

## 1.1 STAP Configuration

STAP has been widely used to mitigate multipath and high-power interference in wireless communications because of its simplicity and excellent performance compared with other systems. Figure 1.2 is a block diagram of a typical STAP system configuration. As shown, this system provides two diversities to improve the reception of the desired signal. The first diversity is space, which is provided by the antenna array. Its performance improves as the number of elements is increased, the gain of the elements is enhanced, or a different ground plane geometry is used. The second diversity in STAP is time, and it is implemented to mitigate multipath propagation.

The basic concept of STAP is to have different replicas of the signal of interest (SOI) in space and time by using several antenna elements and tap delays. Ideally, each one of these replicas experiences independent fading, which makes possible the estimation of the desired signal with fewer bit errors.

The first step in this system consists of the reception of the signal by $N$ antenna elements, separated by at least a half wavelength, to produce space diversity. In some GPS receivers, these elements are positioned on a planar surface. However, the planar surface limits the LOS coverage; so a spherical array has been suggested to increase the LOS of the system [26].

Once the received signal is obtained, it is digitally processed to estimate the SOI. The first step is to delay the received signal $L$-1 times, represented in Figure 1.2 by $\tau_i$. The

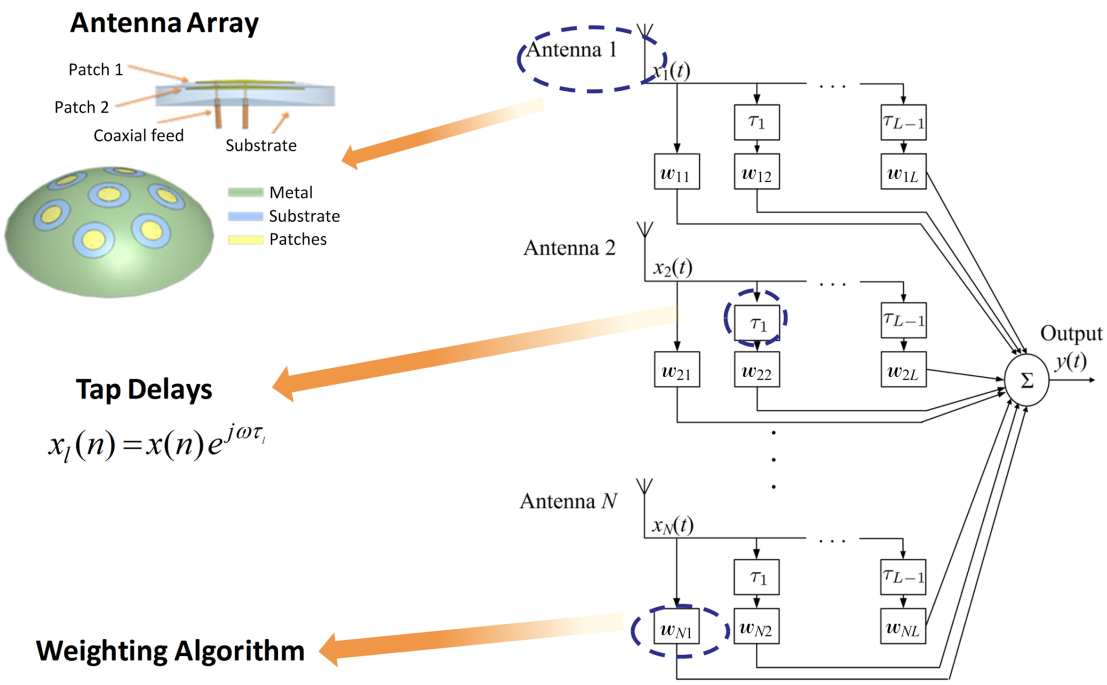


Figure 1.2: Block diagram for the space-time adaptive processing system. The antenna consists of a seven-element planar array; the time delays, $\tau_i$, are uniformly spaced; and the weights, $w_{nl}$, are calculated using the Applebaum algorithm.

output of the filter is a $(NL) \times 1$ vector that can be expressed as

$$\mathbf{x} = \begin{bmatrix} \mathbf{x}_1 \\ \mathbf{x}_2 \\ \vdots \\ \mathbf{x}_N \end{bmatrix} \tag{1.1}$$

where $\mathbf{x}_i = [x_i(\tau_0), x_i(\tau_1), x_i(\tau_2), ..., x_i(\tau_{L-1})]^T$ is a vector containing the received signal at antenna element $i$ and its delayed replicas, and the superscript $T$ indicates the transpose. Note that the signal of the first element of $\mathbf{x}_i$ is not delayed, since this signal is used as reference (i.e., there is a sample of the received signal used as reference at each antenna element). In other words, $\tau_0 = 0$ indicates that no time delay is applied to the first sample. The time filtering is implemented to mitigate the multipath propagation.

The outputs of the time filters are usually weighted to null the interferences. Several methods accomplish this based on the maximum signal-to-interference plus noise ratio (SINR) [27–29] or the least mean square error [30–33]. The Applebaum algorithm [27], also known as Minimum Variance Distortionless Response (MVDR) or Capon's Method, achieves the maximum SINR. Its basic principle is to reduce the susceptibility to jammers and interference by placing nulls in the direction of the jammers and therefore minimize the antenna array input power.

The MVDR establishes that the weights of the antenna elements, which maximize the SINR, are given by

$$\mathbf{w} = \frac{\mathbf{R}_{\mathbf{xx}}^{-1}\mathbf{s}}{\mathbf{s}^{\mathrm{H}}\mathbf{R}_{\mathbf{xx}}^{-1}\mathbf{s}} \tag{1.2}$$

where $\mathbf{R}_{\mathbf{xx}} = E[\mathbf{x}\mathbf{x}^{\mathrm{H}}]$ is the $(NL) \times (NL)$ covariance matrix of the signal at the output of the time filter modeled by (1.1), and H indicates the conjugate transpose. The $(NL) \times 1$ $\mathbf{s}$ vector represents the signal steering vector (for a *non-blind* algorithm) or a "generalized signal vector" (for a *blind* algorithm). If it is assumed that the desired signal is received by the center element (element one) and its exact angle of arrival is not known *a priori*, the "generalized signal vector" recommended by Applebaum [27],

$$\mathbf{s} = \begin{bmatrix} 1 & 0 & 0 & \cdots & 0 \end{bmatrix}^{T} \tag{1.3}$$

is used. Here, $T$ denotes transpose, and the 1 is placed in the position that represents the first received signal replica at element one (center element for the spherical array); i.e., it is assumed the SOI appears only in the top element to avoid the requirement of known information *a priori*.

The final step in STAP is to linearly combine these weighted replicas to obtain the output. Therefore, the output of the system can be written as

$$y(n) = \sum_{l=1}^{L} w_l^* x(n) e^{j\omega\tau_{l-1}} \tag{1.4}$$

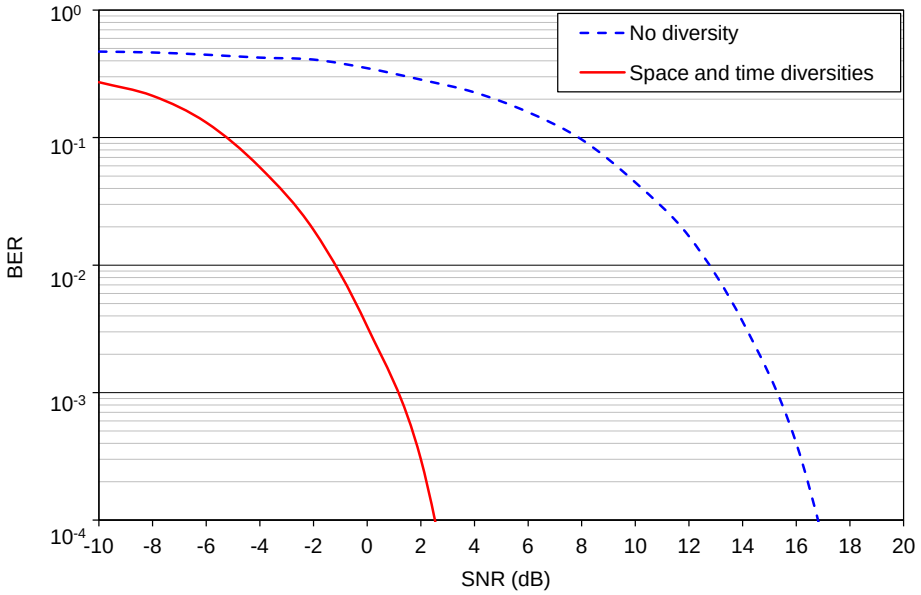


Figure 1.3: BER curves illustrating the improvement in system performance with the use of time and space diversities.

In short, the STAP procedure can be summarized as follows:

1. Receive the signal by $N$ antenna elements.
2. Delay the signal at each antenna element $L$-1 times.
3. Weight the delayed replicas.
4. Combine the weighted replicas.

One example of the enhanced performance of STAP, compared to the no-diversity case, is shown in Figure 1.3. The two diversities (space and time) were integrated by using a seven-element spherical array and two taps (two time delays). The results illustrate a significant improvement by using STAP compared to the no-diversity case. This leads to a better estimation of the SOI, and consequently, more accurate position data in the GPS.

An additional item is how this system compares to others; for instance, Space-Frequency Adaptive Processing (SFAP), another system used to mitigate multipath propagation and high-power interferences. In SFAP, the received signal is transformed into the

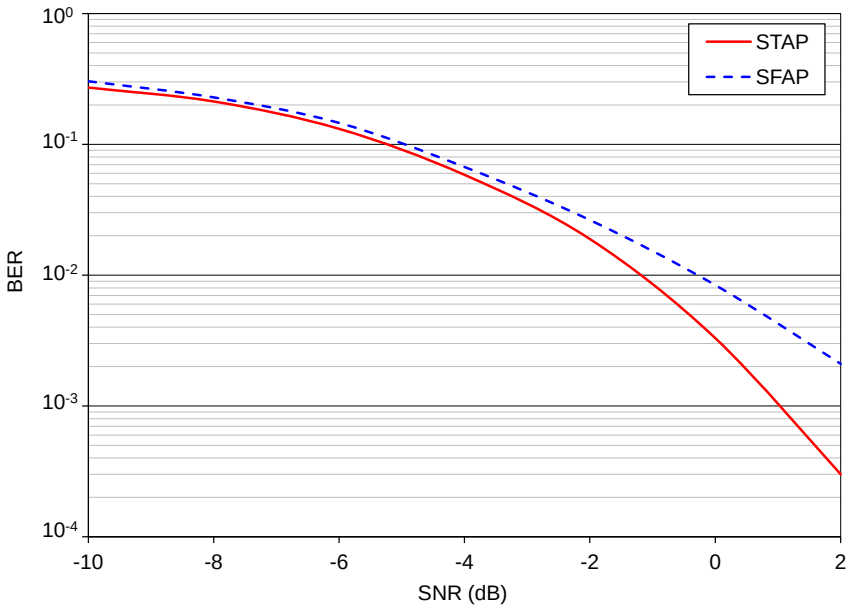


Figure 1.4: BER comparison between STAP and SFAP. The performance of STAP is much better, but SFAP is less computationally complex.

frequency domain, and the frequency range is divided into $k$ bins [15, 34]. Each one of these bins is processed separately (i.e., calculation of the weights and estimation of the signal). At the end, the signal is again transformed into the time domain. The advantage of SFAP is that the covariance matrices are smaller than that of STAP, since the bandwidth range is divided into bins. As a result, its inverse (needed in the Applebaum algorithm) is easier to calculate, making this processing alternative more computationally efficient. These two methods (STAP and SFAP) were compared, and the results are displayed in Figure 1.4. It can be seen that the use of SFAP results in slightly larger bit-error rate (BER) (i.e., worse reception performance than STAP); however, its computation efficiency is greater.

## 1.2 OBJECTIVES

The previous section demonstrates the advantages and improved system performance by integrating STAP. Based on these, this dissertation proposes several system alternatives to improve the GPS signal reception using STAP:

- *Examine and improve the adaptive algorithm*

  The adaptive algorithm has a critical impact on STAP performance because of its ability to suppress high-power interferences. Two metrics are significant for adaptive algorithms: stability and convergence time. The former outlines the ability of the algorithm to converge to some value without varying too much from that value in steady-state environments. The latter measures the time or number of iterations that the algorithm needs to converge. This is very important in real-time applications where the environment is changing. Therefore, the first objective of this research is to analyze and to decrease the convergence time of the adaptive algorithm without degrading its stability.

  To achieve this objective, several modifications will be incorporated into one of the current adaptive algorithms. These modifications should decrease the computational time and maintain and/or improve the stability but not increase the computational complexity of the algorithm. By implementing these changes, the algorithm will improve the overall performance of the STAP system by providing a better alternative to null high-power interferences.

- *Decrease the BER of the system*

  As will be explained later, the time processing can extract important information from each one of the replicas generated by a communication channel when a signal is transmitted. As more information is extracted from the received signal, the better the estimation of the desired signal will be, and the better the communication between the transmitter and the receiver will be. One metric to measure the accuracy of the estimation of the signal is the bit-error rate, a common measurement in wireless communications that provides the ratio of the number of bits that are incorrectly estimated over the number of total transmitted bits. The value of this ratio ranges, in theory, from 0 to 1, where 0 means that the signal is perfectly received and 1 indicates

that none of the received bits is correct. The lower the value of this ratio is, the better the system's performance will be. Therefore, the second objective of this research is to decrease the value of this metric to improve the performance of STAP.

To accomplish this goal without increasing the computational complexity of current algorithms, this research proposes the use of *fixed non-uniformly* spaced taps in the time processing. The use of the proposed distribution should focus the processing on the extraction of more information about the desired signal and thus decrease the BER compared with common distributions. However, one important fact is that the new distribution should not decrease the computational efficiency of the system.

- *Improve the antenna performance*

  The antenna is another component of STAP that impact the reception of the signal. Several modifications can be implemented to enhance its performance, including the number of elements, the geometry, and the characteristics of the substrate. By changing any of these parameters, the gain and bandwidth performances can be improved, so the reception of the signal can be impacted. Therefore, this research proposes the use of an alternate substrate that forces each antenna element to be more directional. If the antenna is more directional, the signal can be received with higher gain, and it will be easier to be estimated correctly.

  In addition, when microstrip elements are used in an array configuration, surface waves can increase the reflection coefficient as the main beam is scanned. As part of this objective, the alternate substrate must reduce the propagation of the surface waves to reduce the reflection coefficient for any scan angle.

  To achieve this objective, a ferrite material will be incorporated in the substrate to modify its impedances and reflection characteristics. This new substrate configuration will be called *hybrid*. By modifying these characteristics, constructive interfer-

ence can be generated to enhance the gain of the antenna and reduce the surface wave propagation.

## 1.3 SUMMARY OF THE CHAPTERS THAT FOLLOW

The remaining of this document is organized as follows:

- *Chapter 2: Adaptive Algorithm*. The first part of this chapter is devoted to a literature review of common algorithms used to null high-power interferences, such as the Applebaum, least mean squares (LMS), and recursive least squares (RLS). Then, the LMS is examined more in detail, and some modifications are proposed to improve its performance. The results of the performance of the modified system are compared with other algorithms, in terms of the time of convergence and the stability of the system. Finally, a brief summary is stated.

- *Chapter 3: Time Processing*. This chapter is devoted to the time processing. It begins with a literature review of taps and a discussion of the common distributions for time spacing. The proposed distributions are presented, and their results are compared with common cases in statistical and measured channels. Finally, a brief summary is provided.

- *Chapter 4: Antenna Array*. This chapter begins with the introduction of the GPS arrays: planar and spherical. The remaining part of the chapter is divided into two parts: *single microstrip elements* and *microstrip element arrays*. In the single element array section, the impact of the hybrid substrate in the bandwidth and gain of a single element will be investigated. The second part presents the performance of the hybrid configuration in arrays. The reflection coefficient and the absolute gain of the array will be used as the metrics to examine the performance. Finally, a summary is presented.

- *Chapter 5: Conclusions and Recommendations*. This chapter provides the conclusions and recommendations for future work.

# Chapter 2

# ADAPTIVE ALGORITHMS

Several algorithms have been developed to adapt the weights in antenna arrays to combat interference and multipath propagation [35–41]. Among them, some of the most popular are the Least Mean Squares (LMS) [40, 42, 43], Recursive Least Squares (RLS), and the Applebaum [27]. The differences between them are based on simplicity, computational efficiency, and convergence rate. The LMS is often preferred for its low computational complexity, although its convergence is not as fast as that of the RLS. Therefore, many adaptations have been implemented in the LMS to achieve faster convergence or to reduce the computational cost. In this chapter, a modified LMS that achieves simultaneously fast convergence and a reduction in the computational cost is presented. This proposed algorithm is optimized for a GPS spherical array used in STAP.

The remainder of this chapter is organized as follows. First, the background of the adaptive algorithm is reviewed. Then, the new modifications to the LMS are explained, followed by the results and a complete comparison between the classic LMS and the proposed adaptation. Finally, a summary of the chapter is presented.

## 2.1 BACKGROUND

The performance of the available algorithms for adaptive arrays can be divided into two categories: optimal weights or computational efficiency. A tradeoff has to be made at the time when the algorithm is selected. Below are the differences between them.

### *Optimal Weights*

The optimal weights for an adaptive algorithm are given by the Applebaum algorithm, also known as Minimum Variance Distortionless Response (MVDR). The development of this

algorithm begins by assuming that the desired received signal, $\mathbf{v}_s$, can be expressed as

$$\begin{aligned}
\mathbf{v}_s &= \alpha s_1 w_1 + \alpha s_2 w_2 + \alpha s_3 w_3 + \ldots + \alpha s_K w_K \\
&= \alpha \sum_{k=1}^{K} s_k w_k \\
&= \alpha \mathbf{S}^T \mathbf{W} \\
\mathbf{v}_s &= \alpha \mathbf{W}^T \mathbf{S} \qquad (2.1)
\end{aligned}$$

where $\mathbf{S}$ is the SOI steering vector with elements $s_k$, $\mathbf{W}$ is the weight vector with elements $w_k$, $\alpha$ is the transmitted signal, T denotes transpose operator, and $K$ is the number of elements. In the same way, the noise vector, $\mathbf{v}_n$, can be written as

$$\begin{aligned}
\mathbf{v}_n &= w_1 n_1 + w_2 n_2 + w_3 n_3 + \ldots + w_K n_K \\
&= \sum_{k=1}^{K} w_k n_k \\
\mathbf{v}_n &= \mathbf{W}^T \mathbf{N} \qquad (2.2)
\end{aligned}$$

where $\mathbf{N}$ is a vector containing the noise received at each element $n_k$. Then, the noise power, $P_n$, can be obtained by

$$\begin{aligned}
P_n &= E\left[|\mathbf{v}_n|^2\right] \\
&= E\left[\left|\mathbf{W}^T \mathbf{N}\right|^2\right] \\
&= E\left[\left(\mathbf{W}^T \mathbf{N}\right)^* \left(\mathbf{W}^T \mathbf{N}\right)\right] \\
&= E\left[\left(\mathbf{W}^T\right)^* \mathbf{N}^* \mathbf{W} \mathbf{N}^T\right] \\
P_n &= \left(\mathbf{W}^T\right)^* \mathbf{M} \mathbf{W} \qquad (2.3)
\end{aligned}$$

where $\mathbf{M} = E[\mathbf{N}^* \mathbf{N}^T]$ is the noise covariance matrix, and $*$ means complex conjugate. This matrix is a positive definite Hermitian (i.e., $\mathbf{M}^T = \mathbf{M}^*$), so whitening (transformation to an equivalent system where the covariance matrix is a scaled identity matrix [44]) can be used to simplify the solution.

Applying the whitening transformation, it can be shown that

$$\widehat{\mathbf{S}} = \mathbf{AS}, \tag{2.4}$$

$$\widehat{\mathbf{N}} = \mathbf{AN} \tag{2.5}$$

and

$$\mathbf{W} = \mathbf{A}\widehat{\mathbf{W}}^T. \tag{2.6}$$

where $\mathbf{A}$ is the transformation matrix. Therefore, the signal and noise vectors can be rewritten as

$$\mathbf{v}_s = \alpha\widehat{\mathbf{W}}^T\widehat{\mathbf{S}} \tag{2.7}$$

and

$$\mathbf{v}_n = \widehat{\mathbf{W}}^T\widehat{\mathbf{N}}, \tag{2.8}$$

respectively. Now, the noise power can be written as

$$\begin{aligned} P_n &= E\left[\left(\widehat{\mathbf{W}}^{\mathbf{T}}\right)^* \widehat{\mathbf{N}}^*\widehat{\mathbf{N}}^T\widehat{\mathbf{W}}\right] \\ &= \left(\widehat{\mathbf{W}}^T\right)^* E\left[\widehat{\mathbf{N}}^*\widehat{\mathbf{N}}^T\right]\widehat{\mathbf{W}} \\ &= \left(\widehat{\mathbf{W}}^T\right)^*\widehat{\mathbf{W}} \\ P_n &= \left\|\widehat{\mathbf{W}}\right\|^2 \end{aligned} \tag{2.9}$$

since the transformation decorrelates the noise, making $E\left[\widehat{\mathbf{N}}^*\widehat{\mathbf{N}}^T\right] = 1_K$, where $1_K$ is an identity matrix of order $K$.

Using (2.7) and (2.9) in the Cauchy-Schwartz inequality, an upper bound of the signal-to-noise ratio (SNR) can be found by

$$\begin{aligned} \text{SNR} &\leq \frac{|\mathbf{v}_s|^2}{P_n} \\ &\leq \frac{|\alpha|^2\left\|\widehat{\mathbf{W}}\right\|^2\left\|\widehat{\mathbf{S}}\right\|^2}{\left\|\widehat{\mathbf{W}}\right\|^2} \\ \text{SNR} &\leq |\alpha|^2\left\|\widehat{\mathbf{S}}\right\|^2. \end{aligned} \tag{2.10}$$

Finally, the optimum weights are given by

$$\begin{aligned} \mathbf{W}_{opt} &= \mathbf{A}^T \widehat{\mathbf{W}}_{opt} \\ &= \mathbf{A}^T \mu \widehat{\mathbf{S}}^* \\ &= \mu \mathbf{A}^T \mathbf{A}^* \mathbf{S}^* \\ \mathbf{W}_{opt} &= \mu \mathbf{M}^{-1} \mathbf{S}^* \end{aligned} \tag{2.11}$$

where $\mu = \left(\mathbf{S}^T \mathbf{M}^{-1} \mathbf{S}^*\right)^{-1}$ to meet the requirement of $\mathbf{W}_{opt}\mathbf{S}^T = 1$. Substituting $\mu$ in (2.11) results in the well-known optimum Applebaum weights

$$\mathbf{W}_{opt} = \frac{\mathbf{M}^{-1}\mathbf{S}^*}{\mathbf{S}^T \mathbf{M}^{-1} \mathbf{S}^*}. \tag{2.12}$$

However, these weights can be generalized to include the desired shape of the pattern. In that case, the weights can be defined as

$$\mathbf{W} = \frac{{\mathbf{R}_{\mathbf{xx}}}^{-1}\mathbf{s}}{\mathbf{s}^{\mathrm{H}} {\mathbf{R}_{\mathbf{xx}}}^{-1} \mathbf{s}} \tag{2.13}$$

where $\mathbf{R}_{\mathbf{xx}} = E[\mathbf{x}\mathbf{x}^{\mathrm{H}}]$ is the covariance matrix of the received signal and $\mathbf{s}$ can be the signal steering vector (for a *non-blind* algorithm) or a generalized signal vector (for a *blind* algorithm). If it is assumed that the direction of arrival of the SOI is not known a priori, the generalized signal vector recommended by Applebaum [27] can be used

$$\mathbf{s} = [1\ 0\ 0\ \cdots\ 0]^T. \tag{2.14}$$

After these weights are applied to the adaptive array, a null is formed in the direction of arrival of the jammer as shown in Figure 2.1. The reduction of gain in the direction of arrival of the jammer due to the adapted weights simplifies the extraction of the desired information.

*Least Mean Squares*

The algorithm described in the previous section requires a high computational capacity due to the calculation of the covariance matrix and its inverse. To reduce the computational

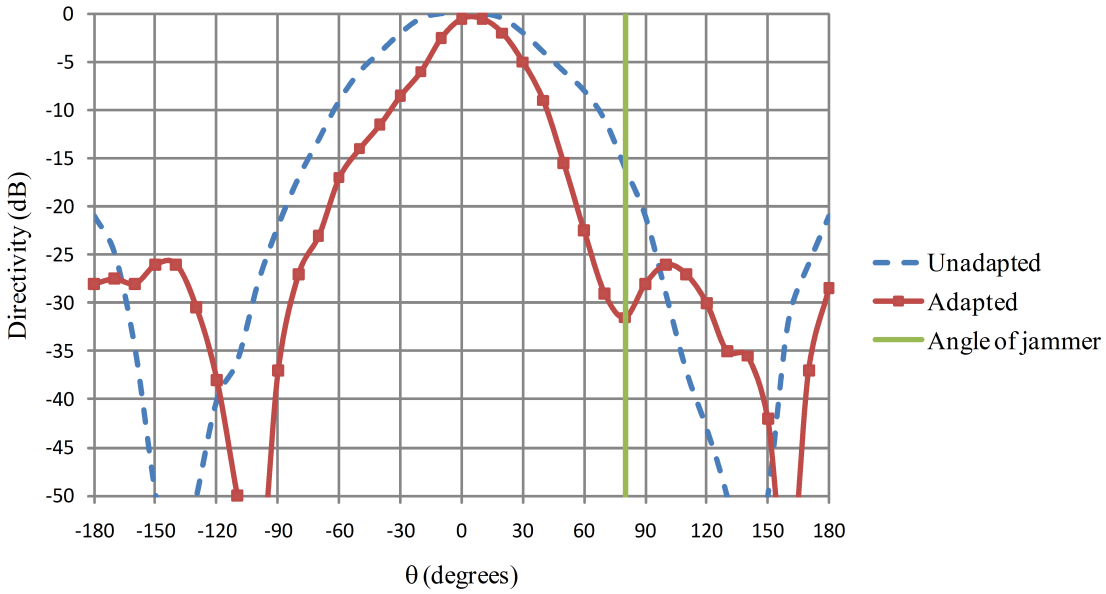


Figure 2.1: Antenna array directivity, based on the Applebaum algorithm, for an spherical array with an incident jammer at $\theta = 80^\circ$ and the SOI incident at $\theta = 0^\circ$.

burden, several adaptive algorithms have been developed to calculate the weights of the adaptive arrays. Between them, one of the most popular is the LMS due to its simplicity. The procedure of this algorithm follows.

Let the elements' input signal be denoted by $x_i$, and the weights by $w_i$, or

$$\mathbf{x} = [x_1, x_2, x_3, ..., x_N]^T \tag{2.15}$$

and

$$\mathbf{w} = [w_1, w_2, w_3, ..., w_N]^T \tag{2.16}$$

where $N$ is the number of elements and $T$ denotes the transpose operator. In addition, the desired response $d(j)$ is a known training signal transmitted over a noisy channel. Therefore, the error $e(j)$ between the desired response and the received signal $y(j)$, for a given instant of time $j$, can be expressed by

$$e(j) = d(j) - y(j). \tag{2.17}$$

The LMS uses a gradient-based method of steepest descent and incorporates an iterative procedure to calculate the weight vector given by

$$\mathbf{w}(j+1) = \mathbf{w}(j) + \mu \mathbf{x}(j+1)e(j). \tag{2.18}$$

The $\mu$ factor, or step size, is a value between 0 and $2/tr(\mathbf{R})$ where $\mathbf{R}$ is the input signal correlation matrix and $tr$ is the trace function (sum of the elements of the main diagonal of a matrix). Successive corrections, in the direction of the negative of the gradient vector, make the weight vector converge to the minimum mean square error.

As an example of the performance of the LMS in multipath environment a channel that includes a direct path, an indirect path and two interferences was analyzed. Figure 2.2 shows the mean square error (MSE) of the channel with different attenuation for the indirect path. At least 100 iterations are required to obtain an MSE less than unity, which sometimes is not adequate for real-time applications.

Other algorithms, such as the RLS, converge with fewer iterations by increasing the computational burden per iteration. For example, Figure 2.3 shows the computational time per iteration of the LMS, RLS, and Applebaum for a weight vector of seven elements. The computational time of the LMS is less than that of the Applebaum and the RLS. The difference in time is not as large as can be expected due to the small size of the weight vector (seven elements). As the number of elements increases the computational complexity of the Applebaum algorithm increases making this alternative non appropriate for real-time processing.

Due to the low number of operations required per iteration, the LMS can perform several iterations before the inverse of the correlation matrix (required by the Applebaum) can be calculated. Figure 2.4 shows the number of iterations in the LMS and the RLS, which required the same number of operations of one matrix inverse, as function of the number of elements, $N$. Here is its evident that when $N$ increases the LMS become more

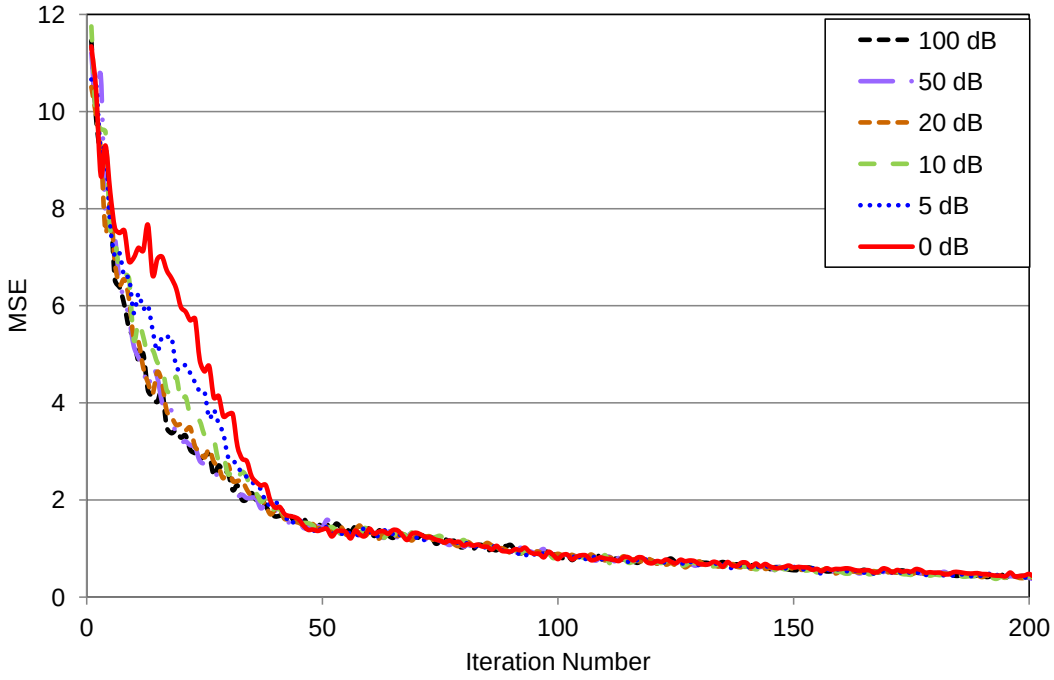


Figure 2.2: MSE for a channel with different attenuations for an indirect path.

viable, since it performs a large number of iterations before a single inverse of the covariance matrix for the Applebaum.

Table 2.1 presents a summary of the advantages and disadvantages of the Applebaum, LMS, and RLS.

## 2.2 MODIFIED LMS ALGORITHM

As indicated previously, the LMS has many advantages that make it very attractive for applications in communications. Therefore, many adaptations have been formulated to improve its performance. One of those modifications, Partial Update LMS (PU-LMS) [45–47], updates a reduced number of weights per iteration. However, as can be expected, this alternative increases the number of iterations to converge. This drawback can be seen in Figure 2.5, where it is shown that the PU-LMS requires more iterations than the LMS and the RLS. Thus, a new modified LMS that involves a partial update but with some

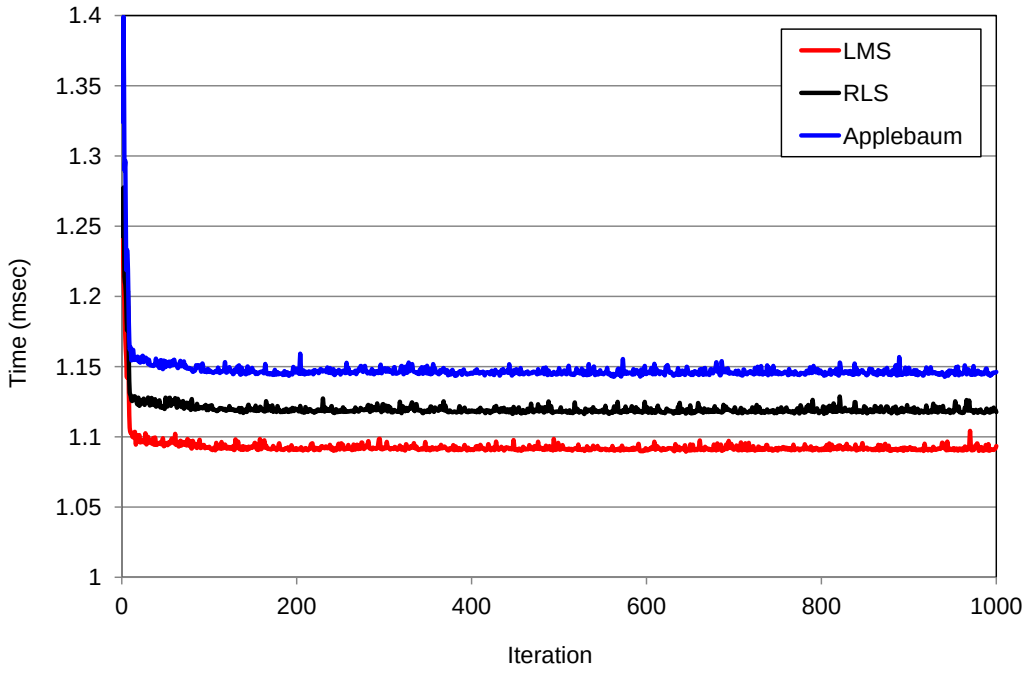


Figure 2.3: Computational time per iteration of several adaptive algorithms for a weight vector of seven elements

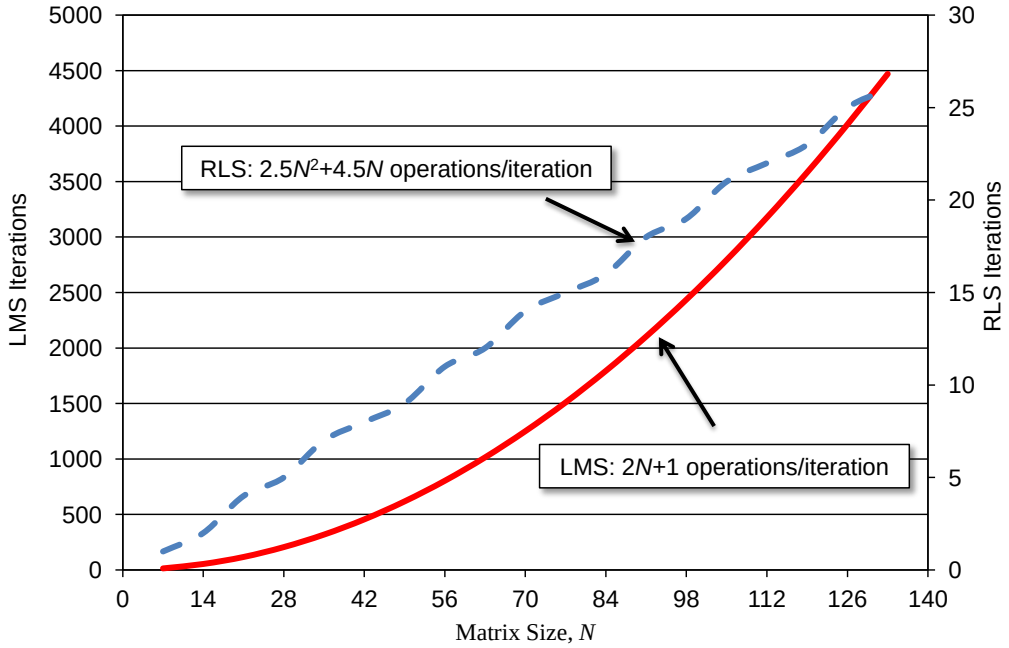


Figure 2.4: Number of iterations in the LMS and the RLS, which require the same number of operations as the inverse for the Applebaum.

Table 2.1: Summary of the adaptive algorithms.

| Algorithm | Formula | Comments |
|---|---|---|
| Applebaum | $\mathbf{w} = \frac{\mathbf{R}_{\mathbf{xx}}^{-1}\mathbf{s}}{\mathbf{s}^{\mathrm{H}}\mathbf{R}_{\mathbf{xx}}^{-1}\mathbf{s}}$ | **Advantage**: Optimum weights. **Disadvantage**: Needs the input signal covariance matrix and its inverse. |
| LMS | $\mathbf{w}(j+1) = \mathbf{w}(j) + \mu\mathbf{x}(j+1)e(j)$ | **Advantage**: Low computational cost, no covariance matrix. **Disadvantage**: Slow convergence. |
| RLS | $\mathbf{w}(j+1) = \mathbf{w}(j) + P(j+1)\mathbf{x}(j+1)e(j)$ | **Advantage**: No covariance matrix, fast convergence. **Disadvantage**: High computational cost. |

specific characteristics that make the algorithm converge faster than the classic LMS with less computational cost is proposed here.

Let us start by denoting the top (center) element in the spherical array as element 1 and the other elements 2, 3, 4, 5, 6, and 7, respectively. Then, it should be noted that, in the spherical array, the top element (element 1) is the main element, or the element that has a greater LOS view toward zenith; thus, it is crucial to update the weight of that element at each iteration. Therefore, the other elements work as auxiliary elements by updating a different element at each iteration. This means that, in the first iteration, $w_1$ and $w_2$ are updated; in the second iteration $w_1$ and $w_3$ are updated; in the third, $w_1$ and $w_4$ are updated, and so on until $w_7$ has been updated. Then the cycle is repeated.

In addition to update the weight of the first element at each iteration, it is necessary to introduce another condition to achieve faster convergence. In this case, the proposed modification is to use different $\mu$ (step size) factors between element 1 and the other elements. It is important to clarify here that the proposed change involves fixed values to

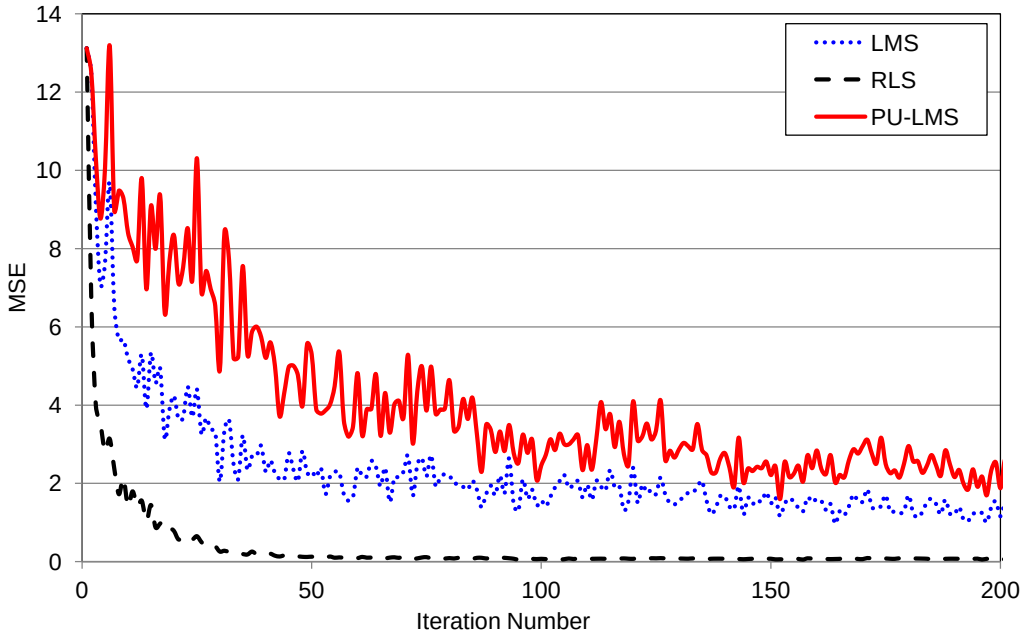


Figure 2.5: Mean square error for different adaptive algorithms.

maintain computational efficiency, but making $\mu_1$ different from the other six. Given that the first element is the main element, the value of $\mu_1$ should be larger than the others, to improve the convergence rate. However, it should not be too large since, in that case, the first element will control the system performance without obtaining good stability. Through parametric studies, it was determined that they should be of the same order of magnitude; for example, $\mu_1 = 10\mu_2 = 10\mu_3 = 10\mu_4 = 10\mu_5 = 10\mu_6 = 10\mu_7$. Larger values exhibits stability problems, and for smaller values, the convergence rate is not improved.

To find the values of $\mu$ that provide stability to this algorithm, let us start by defining a $\mu(k)$ matrix as

$$\mu(k) = \begin{bmatrix} \mu_1(k) & 0 & 0 \\ 0 & \ddots & 0 \\ 0 & 0 & \mu_N(k) \end{bmatrix}, \text{ for } k = 1,2,3,...K \tag{2.19}$$

where $K$ is the number of step size matrices (for the spherical array, $K = 6$). Then, taking the expected value of the weight vector at time instance $j+1$,

$$\begin{aligned} E[\mathbf{w}(j+1)] &= E[\mathbf{w}(j)] + E[e(j)\mu(k)\mathbf{x}(j)] \\ &= E[\mathbf{I} - \mu(k)\mathbf{x}(j)\mathbf{x}^T(j)\mathbf{w}(j)] + \mu(k)E[d(j)\mathbf{x}(j)] \\ &= [\mathbf{I} - \mu(k)\Phi_{\mathbf{xx}}]E[\mathbf{w}(j)] + \mu(k)\Phi_{\mathbf{dx}}. \end{aligned} \tag{2.20}$$

If the initial weight vector is $\mathbf{w}(0)$, $\Phi_{\mathbf{xx}} = \mathbf{Q}^{-1}\lambda\mathbf{Q}$ and $\alpha = (j+1)/k$, where $\lambda$ is a diagonal matrix with the eigenvectors of the input signal covariance matrix, it can be shown that (2.20) can be expressed, after some mathematical manipulations, as

$$\begin{aligned} E[\mathbf{w}(j+1)] = \mathbf{Q}^{-1}[\mathbf{I} - \mu(k)\lambda]^{\alpha-1}\mathbf{Q}\mathbf{w}(0) + \mu(k)\mathbf{Q}^{-1}\sum_{i=0}^{\alpha-2}[\mathbf{I} + \mu(k)\lambda]^i\mathbf{Q}\Phi_{\mathbf{dx}} \\ ... + \mathbf{Q}^{-1}\{\mathbf{I} - \mu(k)\lambda\}^{\alpha}\mathbf{Q}\mathbf{w}(0) + \mu(k)\mathbf{Q}^{-1}\sum_{i=0}^{\alpha-1}[\mathbf{I} + \mu(k)\lambda]^i\mathbf{Q}\Phi_{\mathbf{dx}} \\ + \mathbf{Q}^{-1}\{\mathbf{I} - \mu(k-1)\lambda\}^{\alpha}\mathbf{Q}\mathbf{w}(0) + \mu(k-1)\mathbf{Q}^{-1}\sum_{i=0}^{\alpha-1}[\mathbf{I} + \mu(k-1)\lambda]^i\mathbf{Q}\Phi_{\mathbf{dx}} \\ ... + \mathbf{Q}^{-1}\{\mathbf{I} - \mu(1)\lambda\}^{\alpha}\mathbf{Q}\mathbf{w}(0) + \mu(1)\mathbf{Q}^{-1}\sum_{i=0}^{\alpha-1}[\mathbf{I} + \mu(1)\lambda]^i\mathbf{Q}\Phi_{\mathbf{dx}}. \end{aligned} \tag{2.21}$$

The summation terms in (2.21), when $\alpha \to \infty$ (i.e., after a large number of iterations), tend to $\{\mu(k)\lambda\}^{-1}$. Then,

$$\mu(k)\mathbf{Q}^{-1}\sum_{i=0}^{\alpha-1}[\mathbf{I} + \mu(k)\lambda]^i\mathbf{Q}\Phi_{\mathbf{dx}} = \Phi_{\mathbf{xx}}^{-1}\Phi_{\mathbf{dx}}. \tag{2.22}$$

Equation 2.22 gives the Weiner or optimum weights; thus, the other terms of (2.21) should converge to zero, or

$$\lim_{\alpha\to\infty}[\mathbf{I} - \mu(k)\lambda]^{\alpha} = 0 \tag{2.23}$$

if all the diagonal terms are less than 1. Therefore, the step sizes for the new algorithm to converge are given by

$$\begin{aligned} |1-\mu_1\lambda_1| &< 1 \\ |1-\mu_2\lambda_2| &< 1 \\ &\vdots \\ |1-\mu_N\lambda_N| &< 1 \end{aligned}$$

or

$$\boxed{0 \leq \mu_i(k) < \frac{2}{\lambda_i} \text{ for } i = 1,2,3,...N,\ k = 0,1,...,K} \tag{2.24}$$

The step value of element one is equal to $\mu_1$ at each iteration, but every one of the step values 2 through $N$ is equal to $\mu_0$ ($\mu_0 = min\{\mu_2, \mu_3, ...\mu_N\}$) at every $N-1$ iteration, and at that iteration, all the other step sizes are equal to zero. That means that the algorithm performs only five operations per iteration (LMS operational cost = $2N+1$, and since it calculates just two weights per iteration, the computational cost is $2N+1 = 5$ arithmetic operations).

## 2.3 RESULTS

The proposed algorithm was implemented in MATLAB and analyzed in scenarios with one desired signal, two random interferences, and Gaussian noise. The first simulation consisted of comparing the performance of the modified PU-LMS with the classic LMS using a low step size (more stability) and a high step size (faster convergence). The results of this comparison are illustrated in Figure 2.6, where the proposed algorithm (Modified PU-LMS) clearly performs faster than the classic LMS and achieves the same stability as using a low value for the step size.

The second simulation consisted of the comparison of the proposed algorithm with the Partial-Update LMS, with the results displayed in Figure 2.7. It is evident that the

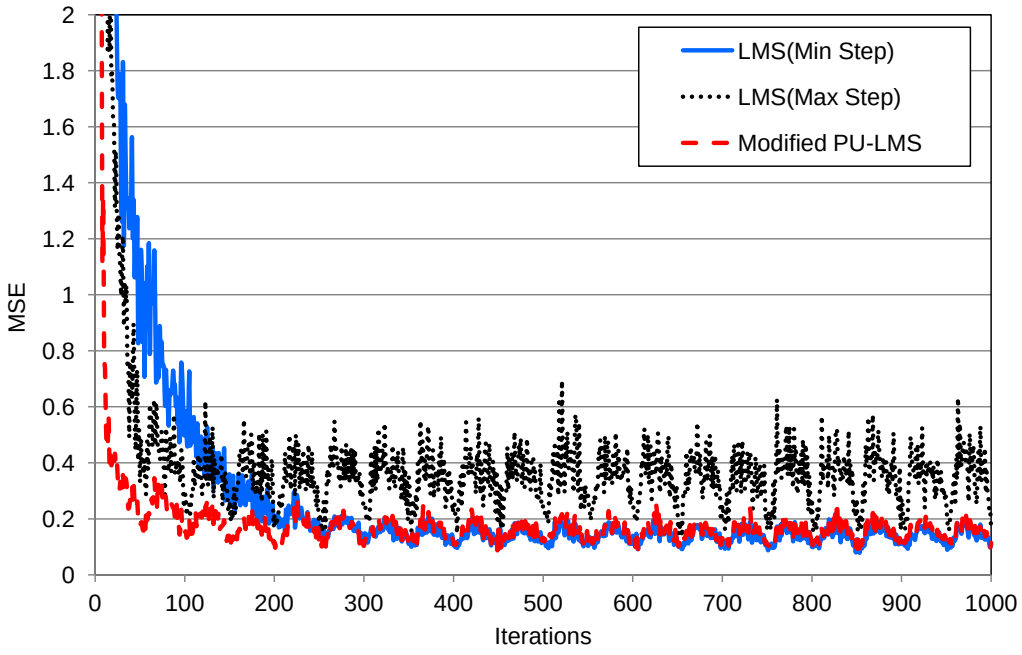


Figure 2.6: Comparison between the proposed algorithm and the LMS using a small step size (good stability) and using a larger step size (fast convergence).

proposed algorithm performs with low computational cost, since it calculates only two weights per iteration, but it also attains faster convergence. This means that two important advantages are achieved: fast convergence and low computational cost.

Another simulation illustrated here is the performance of the proposed algorithm in a non-stationary environment. For this, the angle of arrival of the interferences was randomly changed after a random number of iterations. Figure 2.8 displays the results when the channel had a disturbance after 450 and 600 iterations. It can be appreciated that the algorithm can return easily to the mean squared error that it had achieved before the disturbances. The last example analyzes an environment with more disturbances, and its results are shown in Figure 2.9. As illustrated, the proposed modifications still performed significantly better than the classic LMS algorithm.

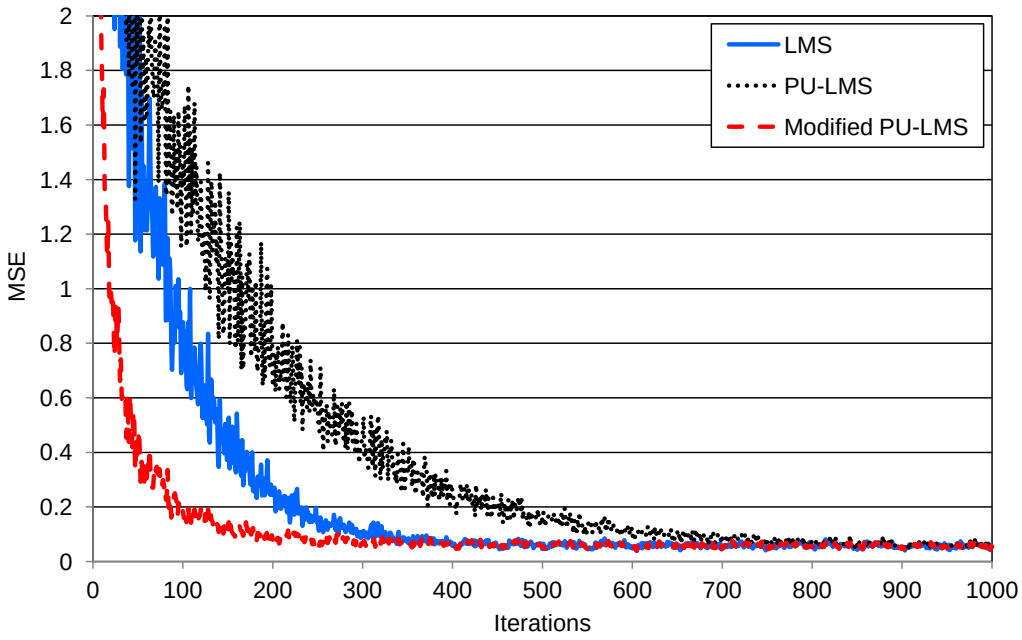


Figure 2.7: Mean square error for the classic LMS, the PU-LMS, and the proposed Modified PU-LMS.

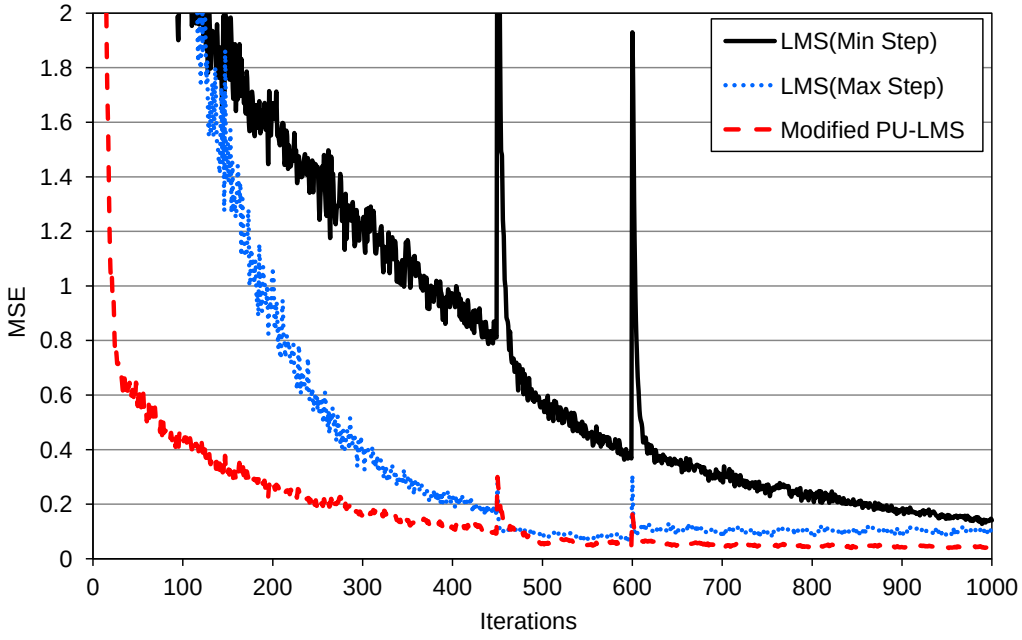


Figure 2.8: Modified PU-LMS in a non-stationary environment.

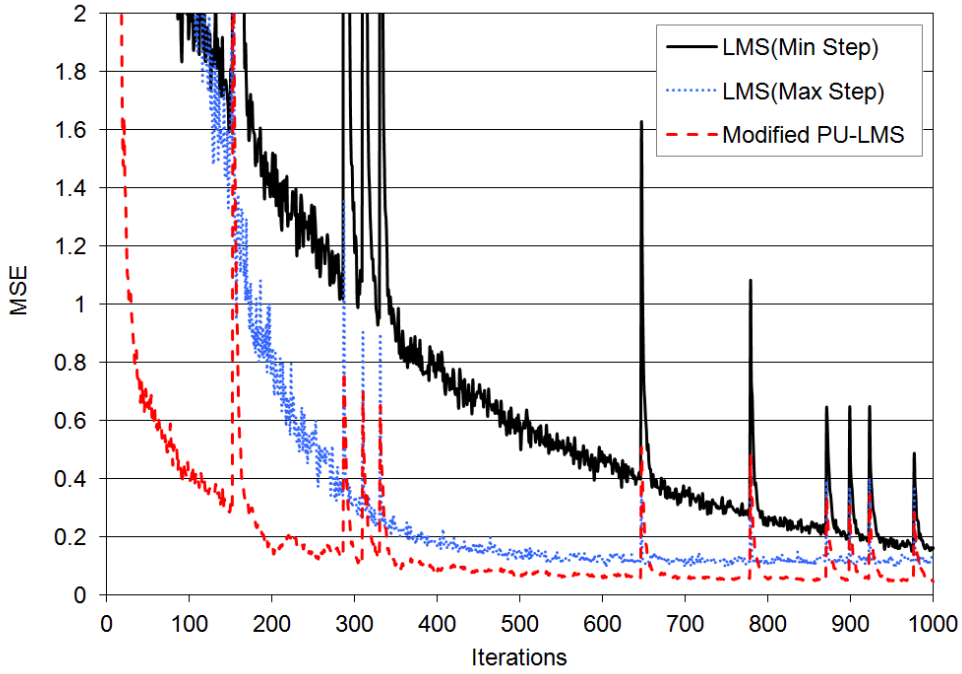


Figure 2.9: Modified PU-LMS in a non-stationary environment.

## 2.4 SUMMARY

A modified partial-updated LMS algorithm optimized for a spherical array intended to be used in a GPS application is proposed. This new algorithm updates the weight of the top element at each iteration and interchanges the update time of the remaining elements in such a way that only two elements' weights are updated at each iteration. Furthermore, it is important that the step size for the top element be larger than the step size for the other elements (but no more than 10 times because then a good stability cannot be achieved).

Several scenarios and comparisons with classic algorithms showed that the proposed algorithm can achieve the same stability as the LMS with a small step size, and its convergence rate is better than the classic LMS using a large step size. In addition, the new algorithm provides the advantage of the PU-LMS since it updates only two coefficients per iteration, thus increasing the computational efficiency.

Chapter 3

# TIME PROCESSING

In a wireless communication system, the desired signal arrives at the receiver through various paths, as explained in Chapter 1. These multiple replicas are usually referred to as *multipath*, and they allow to model the channel as a linear filter with a channel impulse $h_c$ response that can be modeled as [39]

$$h_c = \sum_{k=1}^{K} a_k(t) e^{j\psi_k(t)} \delta(\tau - \tau_k(t)) \tag{3.1}$$

where:

$a_k(t)$: amplitude of path $k$ at time $t$

$\psi_k(t)$: phase of path $k$ at time $t$

$\tau_k(t)$: delay of path $k$ at time $t$

$K$: total number of paths in the channel

Figure 3.1 shows an example of a channel impulse response with six paths. As observed in the figure, at each instant of time (for example $t = t_1$), the channel has six impulses $(\tau_1, ..., \tau_6)$ representing each trajectory of the signal. The impulses do not have the same time delay due to the difference in distance between the paths. In a real system, this difference causes distortion in the received signal. Thus, in a similar way that the coupling is usually not desired in antenna arrays, multipath propagation is not desired in wireless systems. However, in practice, both coupling and multipath, if used properly, can improve the performance of the system.

It is also important to observe that the signals that travel the longer paths usually have the largest attenuations (i.e., lower amplitudes). When the desired signal passes through this channel, the received signal consists of the superposition of these replicas,

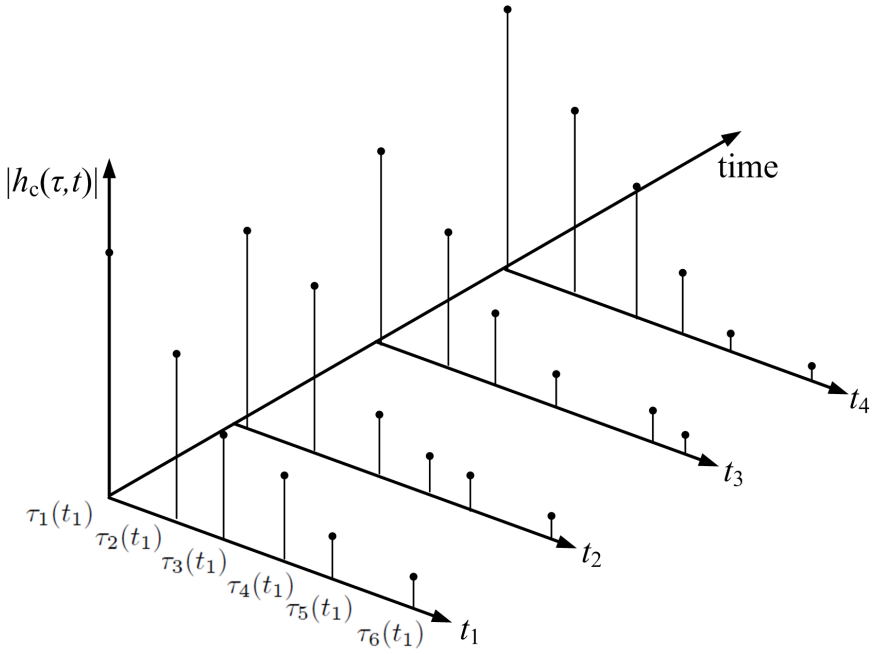


Figure 3.1: Channel impulse response. This impulse response illustrates the performance of a channel with six paths at different time instants.

plus interferences and noise. If the received signal is not processed correctly, the desired information can be lost.

This chapter is devoted to the implementation of the time processing with the purpose of using the information about the replicas in the channel to improve the system performance. The next section presents the background of the time processing with a detailed explanation of the optimal distribution. Then, the proposed distributions are explained. After that, the results assuming a Rician channel are presented. To validate the assumption of the Rician channel, additional results based on models developed by a high-resolution campaign conducted by the German Aerospace Center (DLR) [48] are also available. These results were published in [49, 50]. Finally, a summary of the chapter is included.

## 3.1 BACKGROUND

An important step to mitigate multipath propagation is the time processing of the received signal [51–56]. The process consists of delaying the received signal a predetermined num-

ber of times (also known as taps or time delays), $L-1$, plus a sample of the signal without delay (i.e., $L$ replicas in total). In this way, different echoes from the same source signal can be efficiently simulated. The first tap output corresponds to the received signal without delay, while the $l$ tap output corresponds to the signal delayed $l$-1 times. This means that, if the received signal is *x(n)*, the $l$ tap output is given by

$$x_l(n) = x(n)e^{j\omega\tau_{l-1}} \tag{3.2}$$

where $\omega = 2\pi f$, $f$ is the frequency of operation, and $\tau$ is the time delay. In that stage, the value of the time delay, applied to the replicas, can have a significant impact on the performance of the system. Commonly, the tap delay values are implemented as a uniform distribution because of their simplicity. This means that

$$\tau_i = iT_0, \text{for } i = 1,2,3,...,L-1 \tag{3.3}$$

or

$$\begin{aligned} \tau_1 &= T_0 \\ \tau_2 &= 2T_0 \\ &\vdots \\ \tau_{L-1} &= (L-1)T_0 \end{aligned}$$

where $L-1$ is the number of taps, and $T_0$ is a constant that depends on the application. As can be observed, the delay between two consecutive replicas is constant. However, work based on tap delay tracking algorithms has demonstrated that the optimal delays are not necessarily uniform [57–61]. Even so, these results are based on optimization algorithms that significantly increase the processing time, making the system inappropriate for real-time applications.

Ideally, with an infinite number of time delays or taps, the system achieves its optimal performance. However, in practical applications, a finite number of taps must be

used, and a tradeoff between simplicity (uniform taps) and optimality (tap delay tracking) is required.

For instance, one method to find the optimal spacing is the *Branch and Bound Method*, which is an optimization algorithm that splits all possible solutions into branches to detect those that do not have optimal solutions (based on some cost function) and remove them. Therefore, the algorithm can efficiently use the available resources (i.e., the algorithm uses the information of previous branches to avoid the calculation of non-optimal solutions and focus the computational resources on the combinations that could be optimal). The algorithm converges when it finds the optimal solution or when a predetermined bound has been achieved.

To determine non-equally spaced taps using this method, the procedure can be summarized as follows:

1. Select the final number of taps, $q$, to be used.
2. Select a larger number of taps, $p$ (i.e., $p > q$).
3. Define a uniform distribution $d(l)$ of $p$ taps in the interval $q/p$ to $q$ (i.e., $d(l) = q/p, 2q/p, 3q/p, ..., q$).
4. At each level, delete one tap of the $d(l)$ distribution (using all possible combinations) and calculate the cost function (BER is used in this research).
5. Delete those branches that do not present an optimal combination and extend those branches that could be optimal one more level (delete another tap).
6. The process terminates when one branch (the optimal) remains at the level $p - q$.

The entire flow chart of this method is displayed in Figure 3.2.

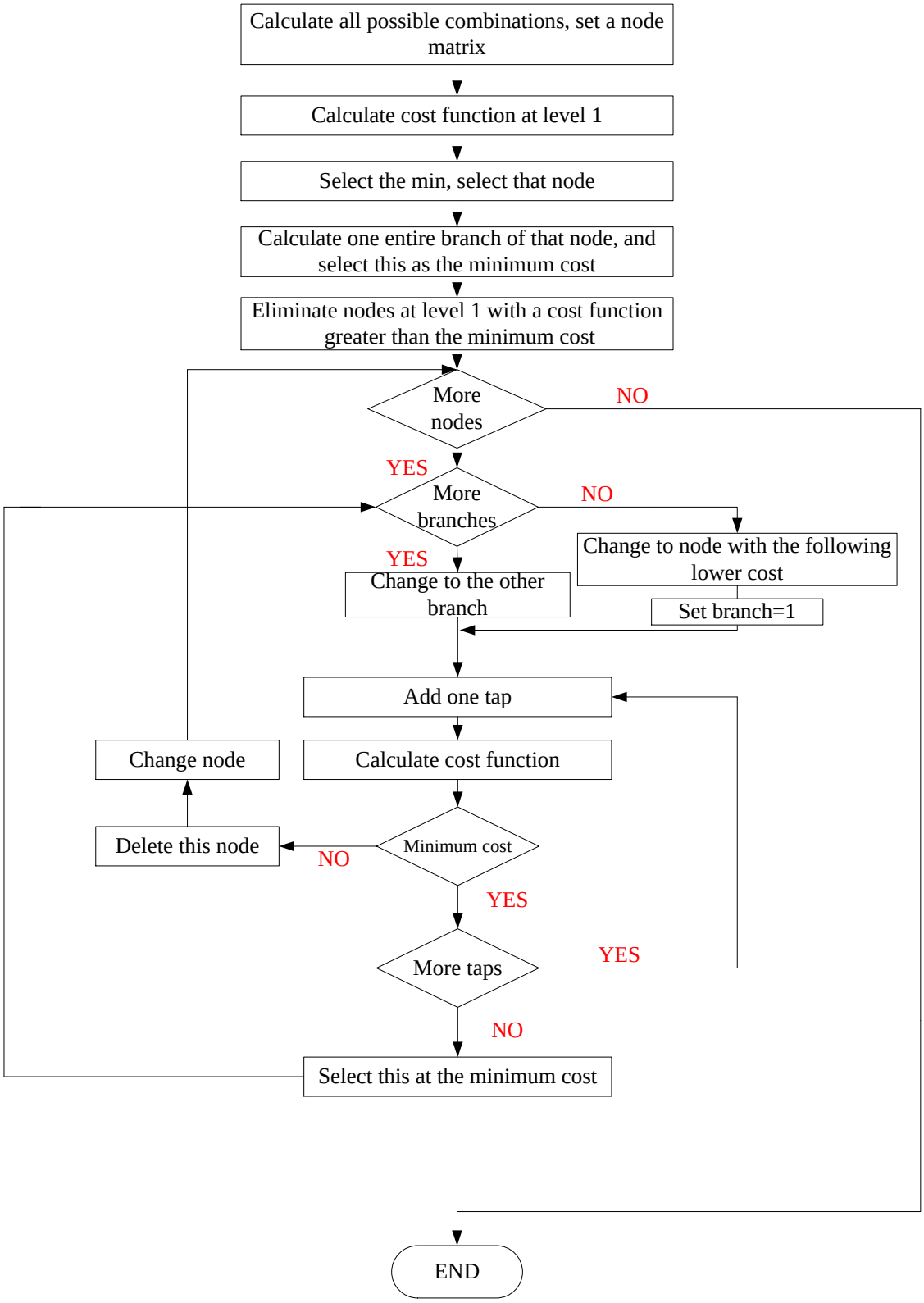


Figure 3.2: Flow chart to calculate non-uniformly spaced taps.

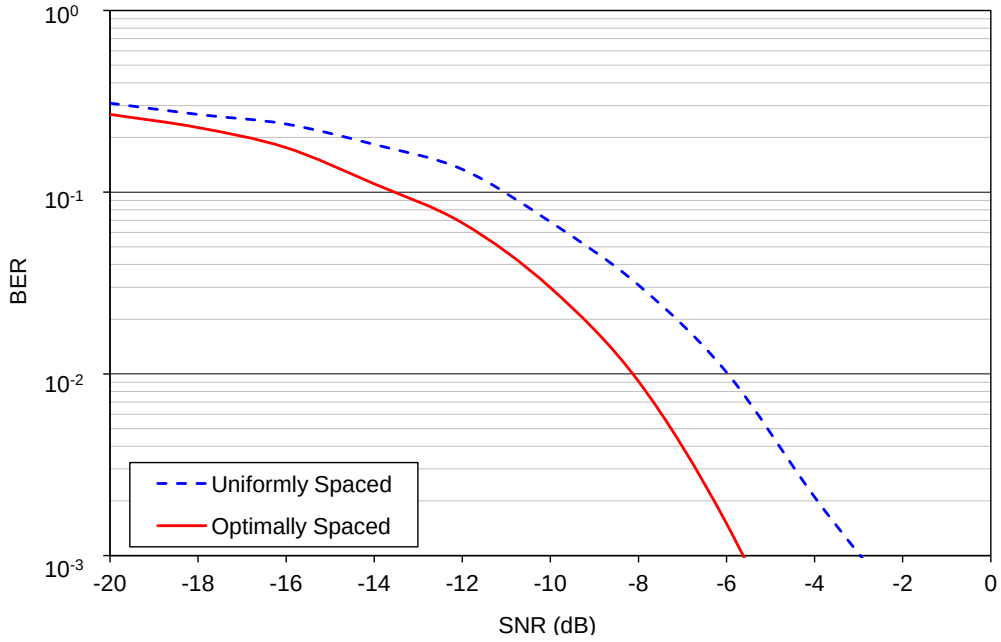


Figure 3.3: BER for uniformly and non-uniformly spaced taps. Figure shows a significant decrease in the BER when non-uniformly spaced taps are used.

Compared to the uniform distribution, this optimization algorithm introduces significant complexity. In a stationary channel, this complexity is compensated by a significant improvement in system performance as shown in Figure 3.3. However, in a non-stationary channel, the entire process has to be continually repeated to obtain optimum spacings, which results in a slower receiver and may not be adequate for real-time processing.

In addition, the optimality of this method depends on the initial number of taps. In theory, an infinite number of taps is required to obtain the optimal combination. Since this is not possible in practical systems, the best combination found by this method is given by the $p$ and $q$ values using the selection criteria stated previously.

Therefore, in searching for a new solution, it is proposed that the use of a fixed non-uniform distribution for the time delays will yield better system performance than the uniform distribution, but without significant compromise in the computational efficiency.

This goal can be attained with a distribution that can be calculated as a pre-process and that can extract important information about the desired signal in any channel.

## 3.2 FIXED NON-UNIFORM DISTRIBUTIONS

Fixed non-uniform distributions that focus the time processing on different time arrivals were used to perform this analysis. These proposed new time delays were modeled as follows:

- Exponential

$$\tau_1 = iT_0 e^{-(L-1-i)}, \text{for } i = 1,2,3,...,L-1 \tag{3.4}$$

or

$$\begin{aligned} \tau_1 &= T_0 e^{-(L-2)} \\ \tau_2 &= 2T_0 e^{-(L-3)} \\ &\vdots \\ \tau_{L-1} &= (L-1)T_0 \end{aligned}$$

The principle behind this distribution is based on the impulse response of a channel. In a practical system, a large number of replicas arrive at the receiver, and the time processing in STAP tries to correlate these replicas to estimate the desired signal. Therefore, a large number of taps would be required to correlate each one of the replicas. However, in a multipath channel, the late arrivals usually have lower amplitude (more attenuation) and therefore less information about the desired signal. With the exponential distribution, the time processing focuses on the early arrivals to obtain more information without using too many taps.

- Rician

$$\tau_i = T_0(L-1)\frac{(L-i)}{\sigma^2} e^{-[(L-i)^2+v^2]/2\sigma^2} I_0\left[0, \frac{(L-i)v}{\sigma^2}\right] \text{ for } i = 1,2,3,...,L-1 \tag{3.5}$$

or

$$\begin{aligned}
\tau_1 &= T_0(L-1)\frac{L-1}{\sigma^2}e^{-[(L-1)^2+v^2]/2\sigma^2}I_0\left[0,\frac{(L-1)v}{\sigma^2}\right] \\
\tau_2 &= T_0(L-1)\frac{L-2}{\sigma^2}e^{-[(L-2)^2+v^2]/2\sigma^2}I_0\left[0,\frac{(L-2)v}{\sigma^2}\right] \\
&\vdots \\
\tau_{L-1} &= T_0(L-1)\frac{1}{\sigma^2}e^{-[1+v^2/2]\sigma^2}I_0\left[0,\frac{v}{\sigma^2}\right]
\end{aligned}$$

where $\sigma^2 = 1$, $v = 1$, and $I_0$ is the modified Bessel function of the first kind of order zero.

- Rayleigh

$$\tau_1 = T_0\frac{i}{\alpha^2}e^{\frac{(L-1-i)^2}{2\alpha^2}}, \text{for } i = 1,2,3,...,L-1 \tag{3.6}$$

or

$$\begin{aligned}
\tau_1 &= T_0\frac{1}{\alpha^2}e^{-(L-2)^2/2\alpha^2} \\
\tau_2 &= T_0\frac{2}{\alpha^2}e^{-(L-3)^2/2\alpha^2} \\
&\vdots \\
\tau_{L-1} &= T_0\frac{L-1}{\alpha^2}
\end{aligned}$$

where $\alpha^2 = 1$.

- Gaussian

$$\tau_1 = T_0\frac{L-1}{\sqrt{2\pi}\sigma}e^{\frac{-(L-1-i)^2}{2\sigma^2}}, \text{for } i = 1,2,3,...,L-1 \tag{3.7}$$

or

$$\begin{aligned}
\tau_1 &= T_0\frac{L-1}{\sqrt{2\pi}\sigma}e^{-(L-2)^2/2\sigma^2} \\
\tau_2 &= T_0\frac{L-1}{\sqrt{2\pi}\sigma}e^{-(L-3)^2/2\sigma^2} \\
&\vdots \\
\tau_{L-1} &= T_0\frac{L-1}{\sqrt{2\pi}\sigma}
\end{aligned}$$

where $\sigma^2 = 1$.

Each one of these distributions was normalized so that the maximum for each one is the same as the uniform.

## 3.3 RESULTS

To analyze the proposed distributions, two different channel types were implemented. The first one is based on stochastic processes, and it is modeled as a Rician distribution. The second channel type is more realistic, and it was developed based on a high-resolution campaign conducted by the German Aerospace Center (DLR) to improve the land and aeronautical channels for navigation communications [48]. These models include shadows and multipath propagation due to buildings, trees, mountains, the ground, etc. [62].

The results of these two types of channels are analyzed in the following subsections.

### *Stochastic Channel Model*

The first step was to develop a stochastic channel model to analyze the performance of the uniform, optimal, and proposed non-uniform spacings. All of them included a LOS path, indirect paths, interferers, and Gaussian noise. Three of these scenarios were chosen and are described in Table 3.1. These scenarios were analyzed in terms of BER, calculated as the ratio of the number of bits errors divided by the total number of transmitted bits, after performing a Monte Carlo simulation. To obtain the optimal combination, eight uniformly spaced taps were selected as the starting point (i.e., $p = 8$ in step 2 of the *Branch and Bound Method*).

In the first scenario, it is assumed that the signal of interest is traveling and received directly above the receiver ($\theta = 0^\circ$). In this case, two indirect paths and two interferers were also arriving at the receiver; this means that the system received a total of five signals (jammers, multipath replicas, and LOS signal). The BER was calculated with a Monte Carlo simulation, and the results are indicated in Figure 3.4. It can be seen that uniform distribution is not a good alternative in this scenario, having a BER as high as $2 \times 10^{-2}$ at

Table 3.1: Implemented scenarios for comparison of the uniform, exponential, and optimal time delay spacings.

| | Scenario 1 | Scenario 2 | Scenario 3 |
|---|---|---|---|
| Desired signal angles | $\theta = 0^\circ, \phi = 0^\circ$ | $\theta = 20^\circ, \phi = 240^\circ$ | $\theta = 5^\circ, \phi = 120^\circ$ |
| Number of interferers | 2 | 4 | 1 |
| Angle of incidence of the interferers | $(\theta_1 = 78^\circ, \phi_1 = 35^\circ)$<br>$(\theta_2 = 89^\circ, \phi_2 = 247^\circ)$ | $(\theta_1 = 83^\circ, \phi_1 = 40^\circ)$<br>$(\theta_2 = 75^\circ, \phi_2 = 230^\circ)$<br>$(\theta_3 = 59^\circ, \phi_3 = 120^\circ)$<br>$(\theta_4 = 69^\circ, \phi_4 = 300^\circ)$ | $(\theta_1 = 65^\circ, \phi_1 = 95^\circ)$ |
| Signal-to-interference ratio, SIR (dB) | -20 | | |
| Number of indirect paths | 2 | 2 | 6 |
| Attenuation of indirect paths (dB) | 10.80, 15.00 | 4.00, 10.00 | 10.00, 12.00, 15.00, 15.50, 16.00, 17.00 |
| Delay of indirect paths (ns) | 0.70, 0.90 | 0.60, 0.90 | 0.70, 0.89, 0.91, 1.20, 2.10, 2.32 |
| Taps | 3 | | |
| Time constant, $T_0$ (s) | $T_{90}/6B = 1.73 \times 10^{-9}$ | | |
| Uniform time delays (s) | $\tau_1 = 1.0000T_0$<br>$\tau_2 = 2.0000T_0$<br>$\tau_3 = 3.0000T_0$ | $\tau_1 = 1.0000T_0$<br>$\tau_2 = 2.0000T_0$<br>$\tau_3 = 3.0000T_0$ | $\tau_1 = 1.0000T_0$<br>$\tau_2 = 2.0000T_0$<br>$\tau_3 = 3.0000T_0$ |
| Optimal time delays (s) | $\tau_1 = 0.3750T_0$<br>$\tau_2 = 0.7500T_0$<br>$\tau_3 = 1.1250T_0$ | $\tau_1 = 0.3750T_0$<br>$\tau_2 = 0.7500T_0$<br>$\tau_3 = 1.1250T_0$ | $\tau_1 = 0.3750T_0$<br>$\tau_2 = 0.7500T_0$<br>$\tau_3 = 1.1250T_0$ |
| Exponential time delays (s) | $\tau_1 = 0.1353T_0$<br>$\tau_2 = 0.7358T_0$<br>$\tau_3 = 3.0000T_0$ | $\tau_1 = 0.1353T_0$<br>$\tau_2 = 0.7358T_0$<br>$\tau_3 = 3.0000T_0$ | $\tau_1 = 0.1353T_0$<br>$\tau_2 = 0.7358T_0$<br>$\tau_3 = 3.0000T_0$ |
| Rician time delays (s) | $\tau_1 = 0.6355T_0$<br>$\tau_2 = 2.4105T_0$<br>$\tau_3 = 3.0000T_0$ | $\tau_1 = 0.6355T_0$<br>$\tau_2 = 2.4105T_0$<br>$\tau_3 = 3.0000T_0$ | $\tau_1 = 0.6355T_0$<br>$\tau_2 = 2.4105T_0$<br>$\tau_3 = 3.0000T_0$ |
| Rayleigh time delays (s) | $\tau_1 = 0.1353T_0$<br>$\tau_2 = 1.2131T_0$<br>$\tau_3 = 3.0000T_0$ | $\tau_1 = 0.1353T_0$<br>$\tau_2 = 1.2131T_0$<br>$\tau_3 = 3.0000T_0$ | $\tau_1 = 0.1353T_0$<br>$\tau_2 = 1.2131T_0$<br>$\tau_3 = 3.0000T_0$ |
| Gaussian time delays (s) | $\tau_1 = 0.4060T_0$<br>$\tau_2 = 1.8196T_0$<br>$\tau_3 = 3.0000T_0$ | $\tau_1 = 0.4060T_0$<br>$\tau_2 = 1.8196T_0$<br>$\tau_3 = 3.0000T_0$ | $\tau_1 = 0.4060T_0$<br>$\tau_2 = 1.8196T_0$<br>$\tau_3 = 3.0000T_0$ |

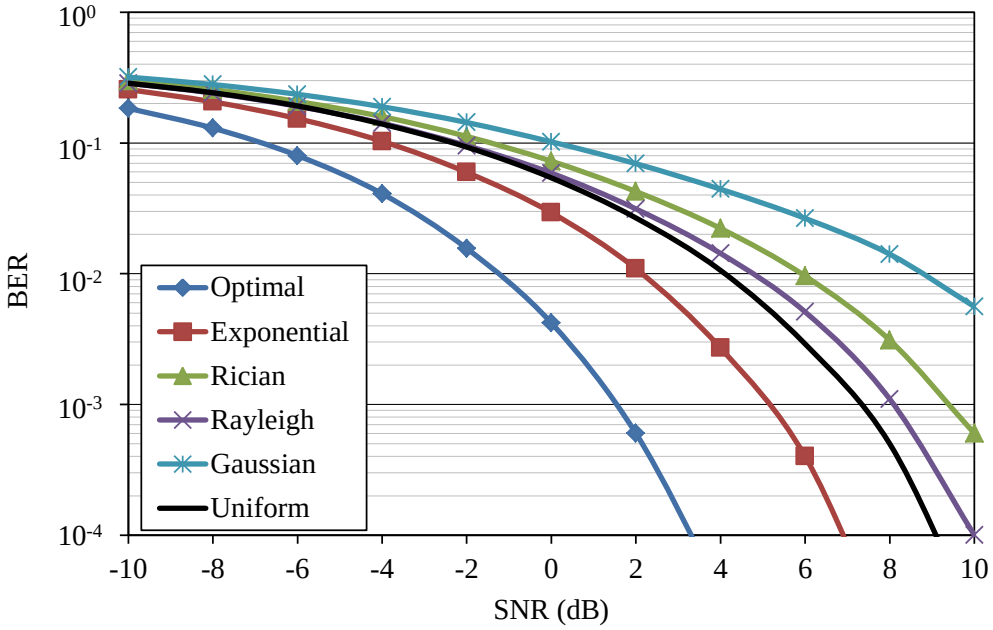


Figure 3.4: BER for uniform, non-uniform, and optimal tap spacing distributions for scenario 1. Figure shows an improvement in the BER by using exponential spacing in a channel with two interferers and two indirect paths.

an SNR of 2 dB. On the other hand, the optimal distribution, obtained with the *Branch and Bound Method* ($p = 8, q = 3$), achieved a BER of almost $6 \times 10^{-4}$ at the same SNR (2 dB), but at the expense of high computational complexity and inefficiency. At the same SNR, the exponential distribution achieved a BER=$1 \times 10^{-2}$, showing a significant improvement compared to the uniform distribution without degrading the system's simplicity, as in the case of the more complex *Branch and Bound Method*. The Gaussian distribution exhibits the worst performance in this scenario.

For the second scenario, the angle of incidence of the signal of interest is $\theta = 20^{\circ}, \phi = 240^{\circ}$, and four interferers are included. The results are displayed in Figure 3.5. It can be observed that the system performance, based on the optimal distribution, was degraded (i.e., high BER for the SNR range). The reason for the degradation is that the Applebaum steering vector given by (1.3) is used, which assumes that the desired signal

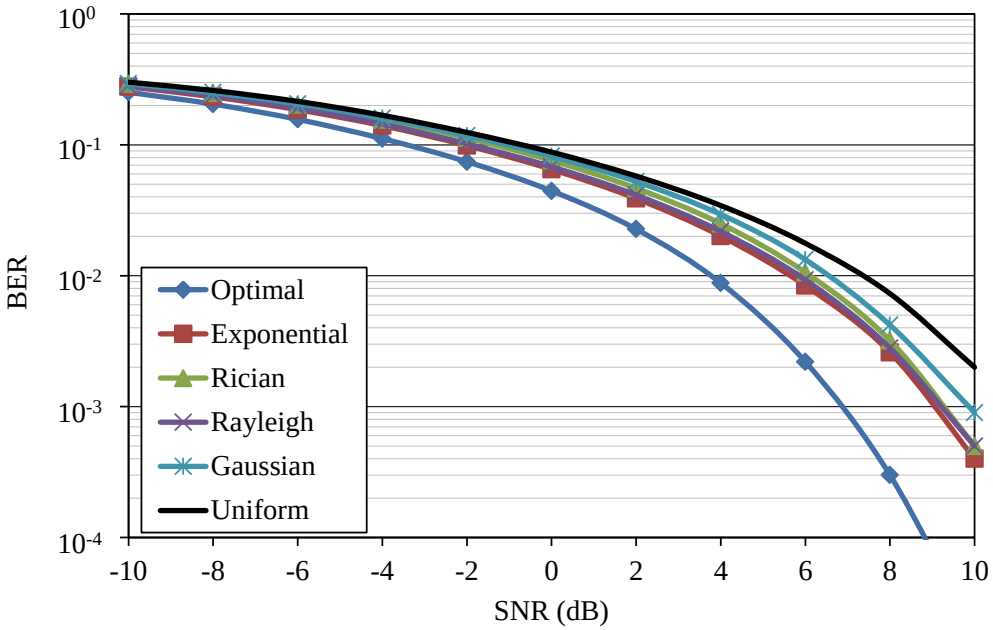


Figure 3.5: BER for uniform, non-uniform, and optimal tap spacing distributions for scenario 2. Figure shows an improvement in the BER by using exponential spacing in a channel with four interferers and three indirect paths.

arrives at the top element, but in the simulated scenario, the angle of arrival was not directly above the receiver. In addition, the SINR was increased by including two more interferers. However, in this simulation, it is also observed that the exponential spacing distribution again outperforms the uniform.

The last simulated scenario includes six indirect paths, but only one interferer. The results are exhibited in Figure 3.6. The system can easily null the interferers because this scenario assumes only one interferer. In this simulation, the improvement of the exponential distribution against the uniform and other non-uniform distributions (i.e., Rician and Rayleigh) is also notable.

It can be seen that, in all the scenarios, the Rician, Rayleigh, and Gaussian distributions are not as good candidates, as the exponential for the time spacing since their

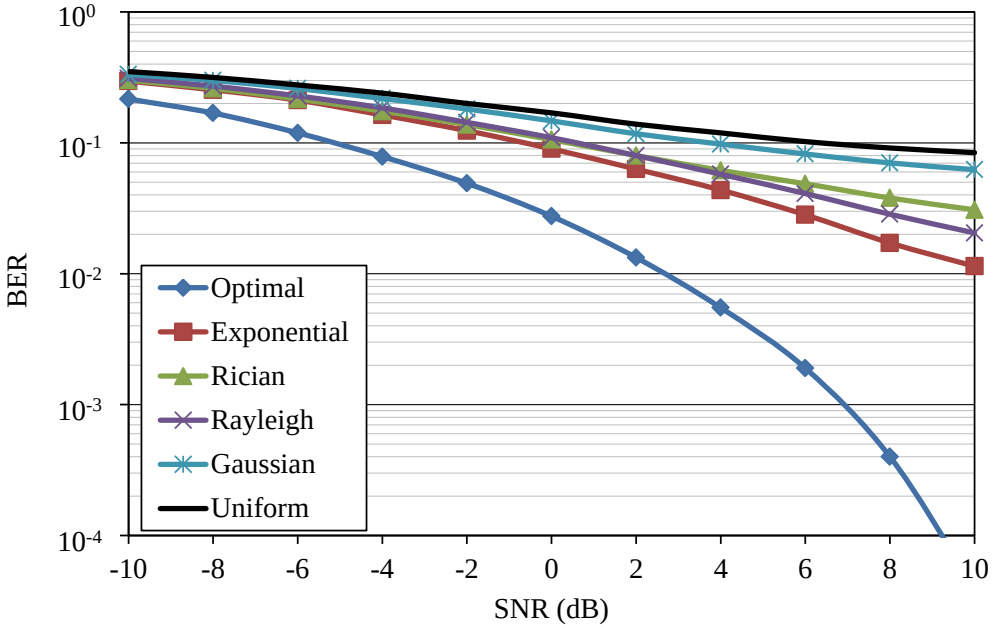


Figure 3.6: BER for uniform, non-uniform, and optimal tap spacing distributions for scenario 3. Figure shows an improvement in the BER by using exponential spacing in a channel with one interferer and seven indirect paths.

performances are very similar to or worse than the uniform performance in all the modeled scenarios.

### Deterministic Channel

In the previous analysis, a Rician model was used to simulate the multipath channel. This statistical representation assumes that the channel has a strong dominant component that can be the LOS; the other replicas will be of a much lower strength. To compare the performance of this model with an alternate environment, a deterministic channel was simulated.

The implemented channel consists of the LOS path and a replica, as shown in Figure 3.7. To simplify the analysis, several assumptions were made: the transmitting antenna is isotropic, the signal is reflected by a flat perfect electric conductor (PEC) rectangular plate, and $TE^x$ polarization is assumed. For the analysis, Physical Optics (PO) theory [63] was

used. Therefore, the scattered electric field is represented by

$$E_r = 0 \tag{3.8}$$

$$E_\theta = c\left\{\cos\theta_s \sin\phi_s \left[\frac{\sin(X)}{X}\right]\left[\frac{\sin(Y)}{Y}\right]\right\} \tag{3.9}$$

$$E_\phi = c\left\{\cos\phi_s \left[\frac{\sin(X)}{X}\right]\left[\frac{\sin(Y)}{Y}\right]\right\} \tag{3.10}$$

where

$$c = \frac{-j\eta ab\beta H_0 e^{-j\beta r}}{2\pi r} \tag{3.11}$$

$$X = \frac{\beta\alpha}{2}\sin\theta_s\cos\phi_s \tag{3.12}$$

$$Y = \frac{\beta b}{2}(\sin\theta_s\sin\phi_s - \sin\theta_i) \tag{3.13}$$

$\eta$ is the intrinsic impedance, $a$ and $b$ are the dimensions of the rectangular plate, $\beta$ is the phase constant, $H_0$ is the magnitude of the incident H-field, $r$ is the distance between the flat plate and the receiver, and $(\theta_s, \phi_s)$ are the observation angles. It was assumed that $a$ and $b$ are 5 wavelengths.

The performance of the STAP in this type of channel was analyzed in terms of BER by varying $\theta_i$ and fixing $\theta_s = 30^\circ$ for different SNRs. The results of this analysis are displayed in Figure 3.8. $|E|$ and $|E_s|$ represent the magnitude of the receiver antenna radiation pattern towards the incident angle of the indirect and LOS signals, respectively. Clearly, the performance of the system is highly dependent on the observation angle of the indirect replica since, when $\theta_m = \theta_s = 30^\circ$ (i.e., the receiver is in the specular direction or maximum of the scattered field), the performance of the system is highly degraded. Therefore, if the Rician model is used, the model may not be very accurate depending on the incident angles of the replicas and the system input power. However, its advantage is that no *a priori* information is required about the incoming signals. This is an excellent advantage in wireless communications where the channel is continually changing.

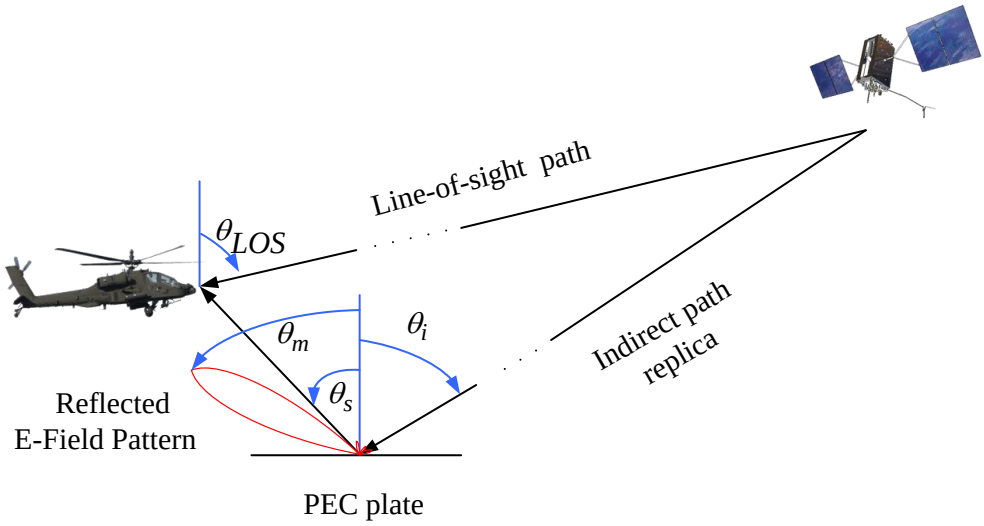


Figure 3.7: Model for the deterministic channel. The channel consists of the LOS path and one replica from a PEC plate.

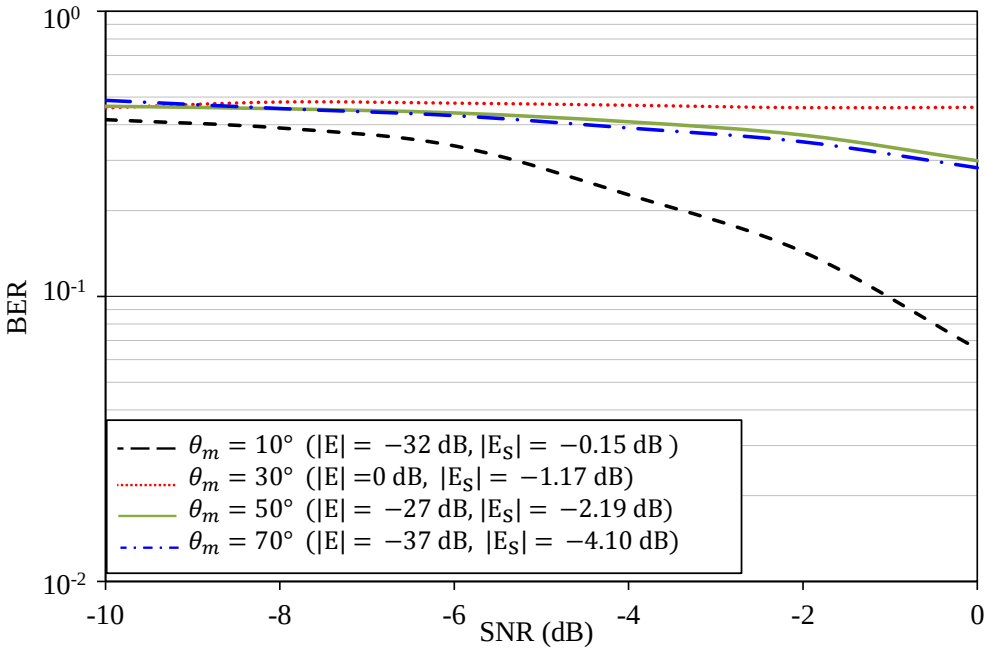


Figure 3.8: BER for a deterministic channel with the LOS path signal and one replica. The results show the performance of the system as the angle of incidence of the replica is varied.

### Time Constant

It can be noted that, in addition to the spacing distribution, the constant $T_0$ can impact the STAP performance. Concerning this topic, different suggestions can be found in literature [55]; thus, the next step was to analyze the proposed system with different time constants, $T_0$ . For this, the possible values were divided into ranges:

Small values:

$$0 \leq T_0 \leq T_{90} \tag{3.14}$$

Intermediate values:

$$T_{90} < T_0 < T_{90}/B \tag{3.15}$$

Large values:

$$T_0 \geq T_{90}/B \tag{3.16}$$

where $T_{90} = \pi/(2\omega_0)$ is the quarter wavelength delay and $B$ is the fractional signal bandwidth. Different scenarios were analyzed for values within these ranges, and one of the results is shown in Figure 3.9. It can be observed that values below $T_{90}/B$ produce good performance and that large values degrade the system response. However, after the analysis of the antenna weights, it was also noted that small values produce coefficients with large relative magnitudes, which are not adequate for practical systems. That means that the optimal value for the time constant is in the range of intermediate values. In particular, a value of $T_{90}/2B$ produced the best results in all the analyzed cases.

### Reference Tap

The tap selected as the reference can also have a considerable impact on the system performance. In the literature, most of the suggestions have focused on using the center tap as a reference. However, there is not a consensus on this topic [24, 61]. Consequently, this section attempts to give a better insight on this issue.

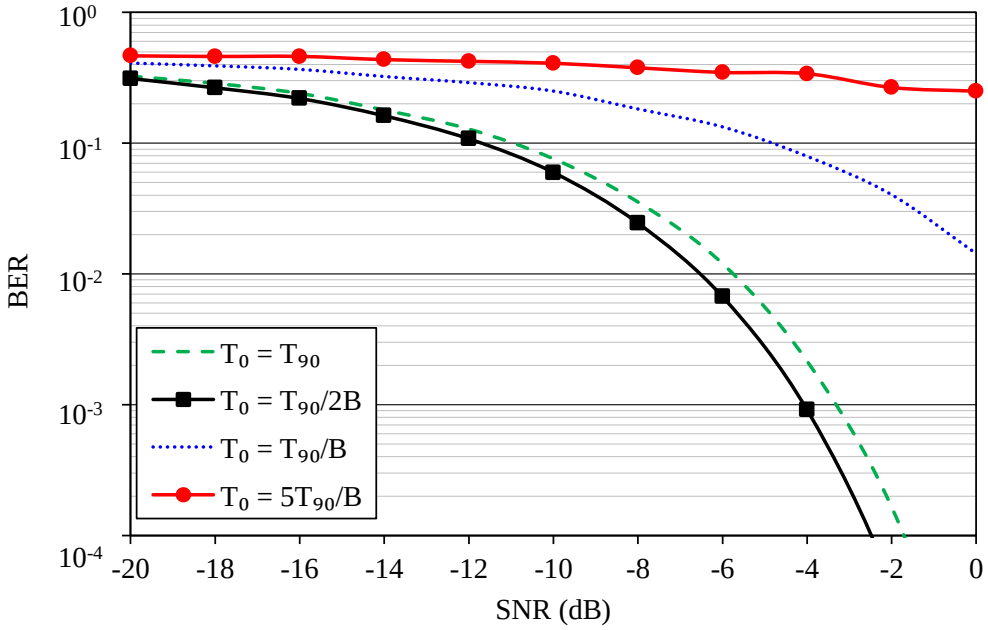


Figure 3.9: BER for different tap spacings.

To start the discussion, some results found in [24] are used here. In [24], the authors used an isotropic five-element planar array (designed to work at a center frequency of 2.004 GHz) and seven taps per antenna element. This array was exposed to several combinations of wideband and continuous wave (CW) interferences, and their results showed that the center tap for each antenna element should be used as a reference to obtain the best performance.

During this project, this experiment was reproduced to obtain the BER as the reference tap was varied. In agreement with [24], the results showed that, indeed, with the array and the scenarios reported in [24], the center tap position presents the best performance. This can be observed in Figure 3.10, where the system was exposed to an interference at 65 degrees from zenith. The figure shows that, when the fourth tap is used as the reference, the BER is lower than for the other positions, meaning better system performance.

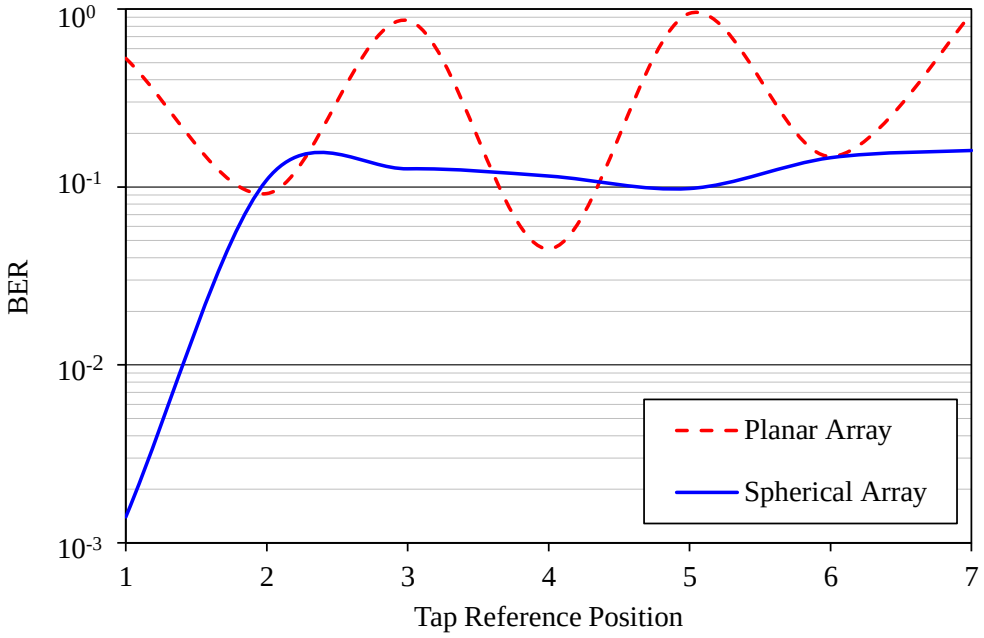


Figure 3.10: BER for a system with a five-element planar array and with a seven-element spherical array. The system is exposed to an interference at 65 degrees from zenith.

Thus, the next step was to use the seven-element spherical array with the same scenario as in [24] to assess whether the performance was similar with a different array geometry. The results for this new simulation exhibited a different behavior. In this case, the best performance was obtained with the first tap as the reference for each antenna element. This result is also plotted in Figure 3.10 for a comparison with the results of [24].

Surprisingly, however, different results were obtained for a scenario with the interference incident at 45 degrees, instead of 65 degrees. In this case, the center tap no longer displays the lowest BER; rather, the second and the first positions were the optimal for the planar and the spherical array, respectively. The results for this new scenario are illustrated in Figure 3.11.

Considering these results, two important issues can be concluded in terms of the reference tap. First, the reference is a function of the antenna array geometry configuration;

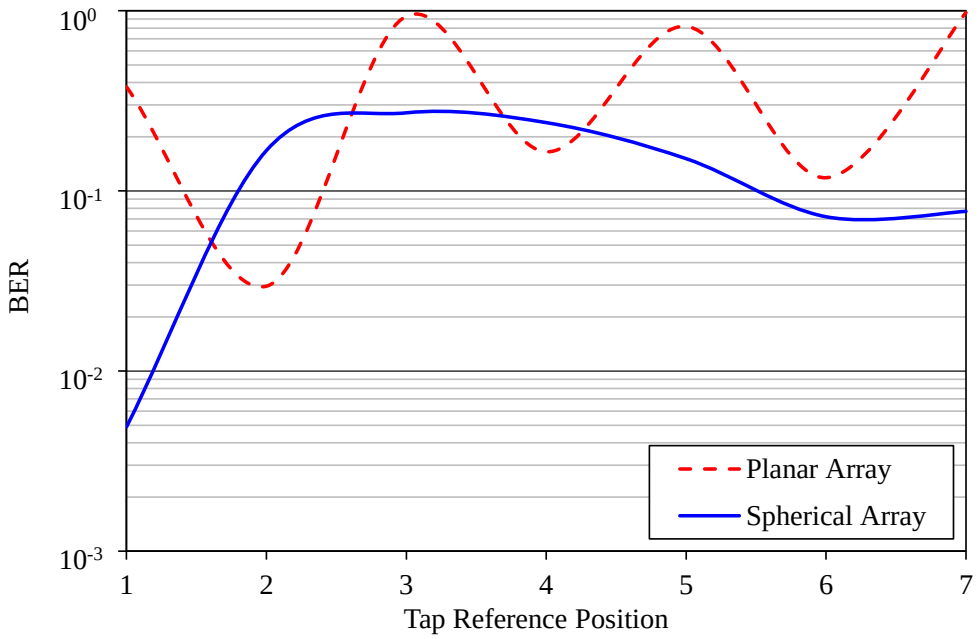


Figure 3.11: BER for a system with a five-element planar array and with a seven-element spherical array. The system is exposed to an interference at 45 degrees from zenith.

the same performance is not obtained for different array geometries. Second, the channel influences the behavior of the reference tap. Therefore, before the reference tap is selected, it is recommended to examine the channel with the array to be used. However, depending on the number of taps, the process to set each tap as a reference and analyze the system can take a long time. One suggestion to decrease the time is to use a method like the steepest descent to find the minimum bit-error rate as a function of the reference tap [56].

This method was applied to the seven-element spherical array with seventeen taps, and it was observed that the algorithm does not always converge to the global minimum, but at least the local minima are comparable in magnitude with the global minimum. For instance, the BER for this system is shown in Figure 3.12, and it can be observed that there are three local minima (at the first, eighth, and fifteenth positions) with similar magnitudes. However, the starting position is crucial to determine to which of these reference positions the algorithm converges. For example, Figure 3.13 illustrates the minimum found for dif-

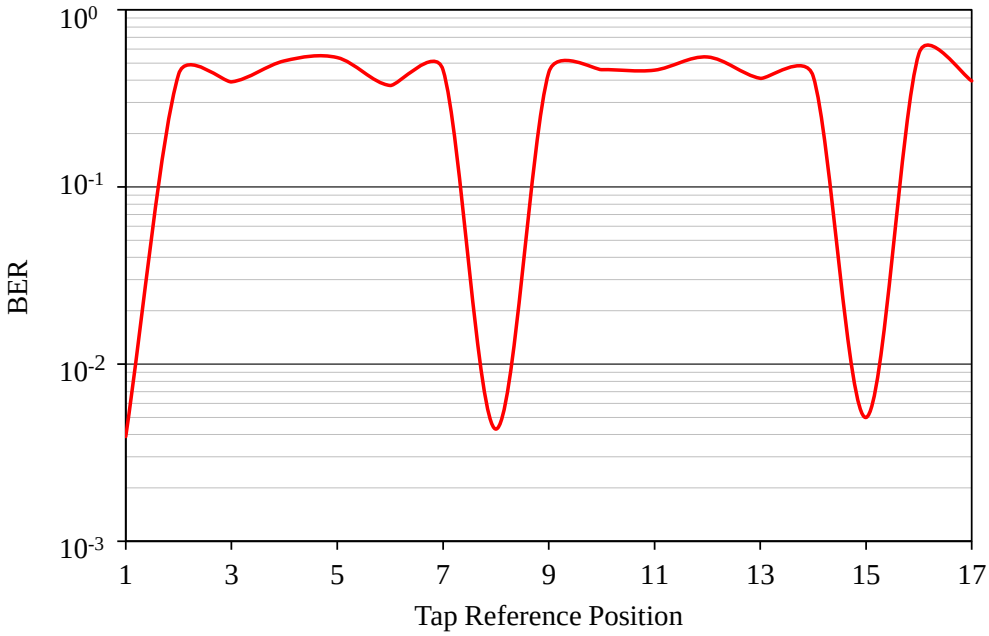


Figure 3.12: BER for a system with a seven-element spherical array and seventeen taps. Three positions present local minima.

ferent initial positions, and shows how many steps are needed to converge. It is important to note that, if this method is not used, 17 steps are needed to find the best position, but with this method, the worst case is 12 steps. Obviously, it reduces the computational time (compared with no algorithm), and improves the system performance (compared with fixing one position without examining the channel and antenna array).

### GPS Codes

The development of the previous results was based on the system performance without coding. However, GPS systems use two different codes to transmit data: the precision code and the coarse/acquisition code. The first one is a long sequence ($6.1871 \times 10^{12}$ bits) used with military signals, while the second is a 1,023-bit sequence used for civilian applications. The two codes are used to compensate for the low signal power in GPS systems.

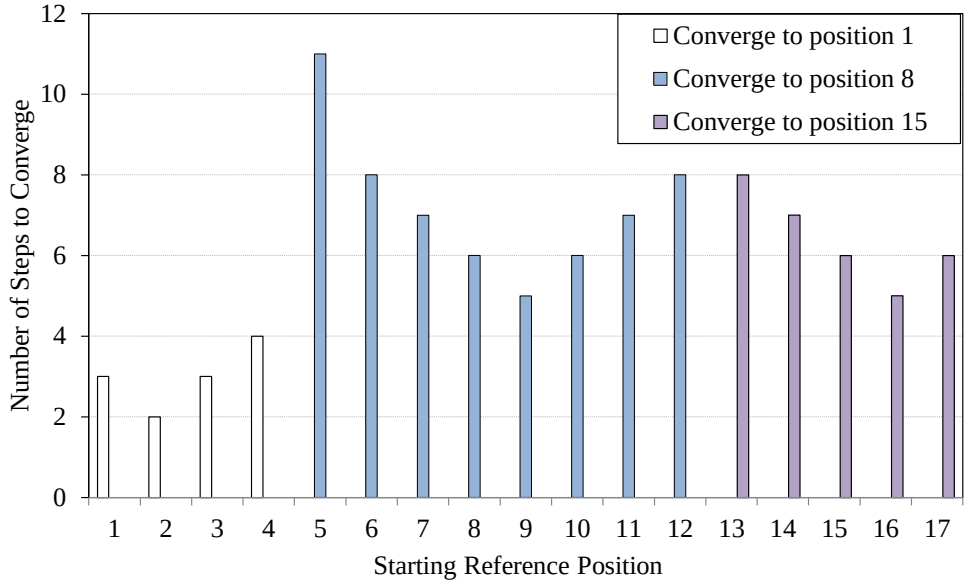


Figure 3.13: Number of steps to converge as a function of the initial position using the steepest descent method. The position of convergence is also shown.

Given that the precision code is an extremely large code, the results shown here are based only on the coarse/acquisition code. This code was included in the system, and the BER response was calculated for the uniform, the exponential, and the optimal tap distributions. The results are displayed in Figure 3.14, which when compared to previous results, it can be observed that the most significant impact in the system performance is a reduction in the SNR for a fixed BER. This means that the signal with coding can be estimated better than one without coding in high noise power environments or with low signal power, as in GPS cases.

*Validation of the channel model*

After the implementation and analysis of the stochastic channel type, a more realistic channel type was selected. For this, several channel models based on an intense campaign were used. These models were developed for aeronautical, urban car, urban pedestrian, suburban car, and suburban pedestrian environments.

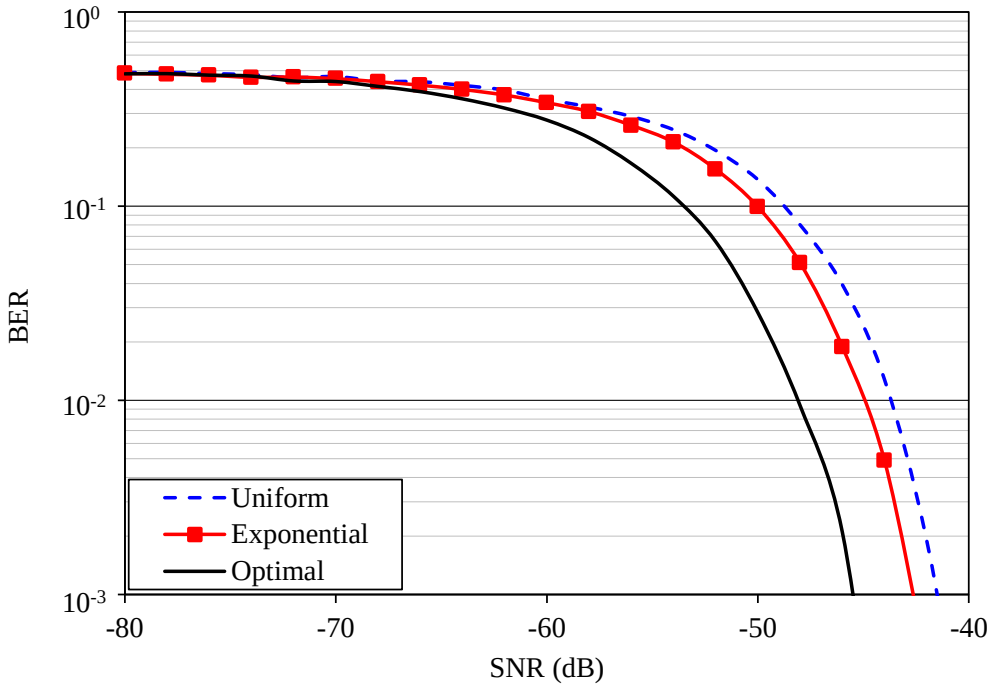


Figure 3.14: BER for a coded GPS signal for the uniform, exponential, and optimal distributions.

For every simulation, the multipath channel was generated with the available models, and then two jammers were included with random direction of arrivals in the elevation angular range of $25^\circ \leq \theta \leq 100^\circ$; $\theta = 0^\circ$ is zenith. A direct path at $\theta = 0^\circ$ for the desired signal was also included in the simulations. All the available multipath channels were analyzed (i.e., aeronautical, urban car, urban pedestrian, suburban car, and suburban pedestrian). Three taps ($L = 4$) were used for all the simulations.

The first step was to analyze the time constant $T_0$ for each one of the channels in terms of the BER as a function of the SNR. For this, $T_0$ values of $10^{-10}$, $10^{-9}$, $10^{-8}$ and $10^{-7}$ were used. For each value, the uniform, exponential, Rayleigh, Rician, and Gaussian tap distributions were analyzed. An example of one of these simulations is shown in Figure 3.15 for $T_0 = 10^{-8}$ in an urban pedestrian channel. In this scenario, it is evident that the

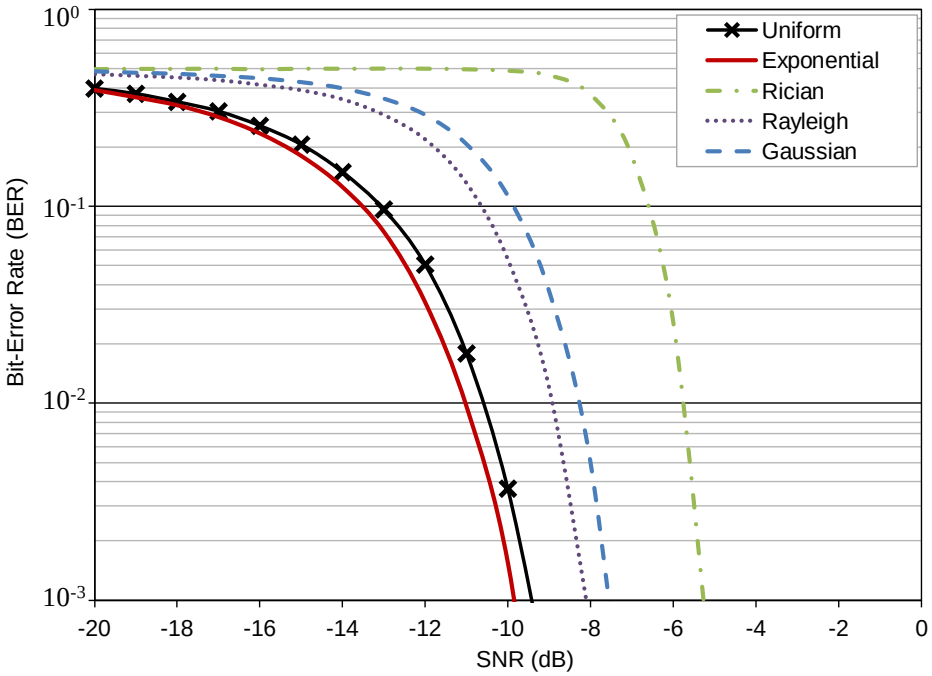


Figure 3.15: BER of a STAP system for different taps distributions for an *urban pedestrian* multipath channel using $T_0 = 10^{-8}$.

exponential distribution outperforms the uniform using the same time constant $T_0 = 10^{-8}$, which is commonly used in GPS scenarios.

The process was repeated for each value of $T_0$ (from $10^{-10}$ to $10^{-7}$) in all the channels. Each of the examined $T_0$'s leads to a best performance for the following distributions:

- $T_0 = 10^{-10}$: Gaussian
- $T_0 = 10^{-9}$: Exponential
- $T_0 = 10^{-8}$: Exponential
- $T_0 = 10^{-7}$: Uniform

Next, each channel was analyzed, using $T_0$ from above with their respective distribution, to compare the performance between the distributions. The results for the aeronautical channel are shown in Figure 3.16. Clearly, the exponential distribution, using

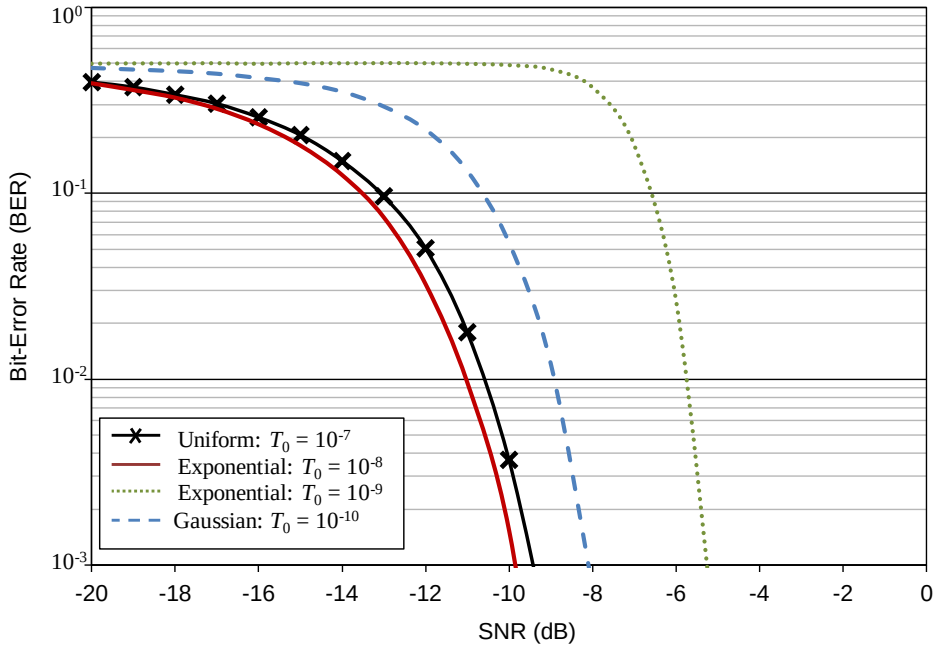


Figure 3.16: BER of a STAP system for different $T_0$, using their best tap distributions, for an *aeronautical* multipath channel.

$T_0 = 10^{-8}$, results in the lowest BER or the best system performance. For a BER = $10^{-3}$, the system can operate at an SNR of 1 dB less than the uniform using $T_0 = 10^{-7}$. In addition, it is evident that, although the Gaussian distribution performs the best using $T_0 = 10^{-10}$, compared with the other distributions, its performance is not as good as the others. Actually, for the aeronautical channel with an SNR = -9 dB, the BER for the Gaussian is $1.2 \times 10^{-2}$, whereas for the exponential, it is $0.5 \times 10^{-4}$ (240 times lower).

The same analysis was applied to the land mobile channel. Three examples are illustrated in Figure 3.17, 3.18, and 3.19 (similar results were obtained for the suburban car not shown here). Figure 3.17 shows the performance of the system in the suburban pedestrian multipath channel. It is also clear that the exponential using $T_0 = 10^{-8}$ outperforms the other distributions by decreasing the BER.

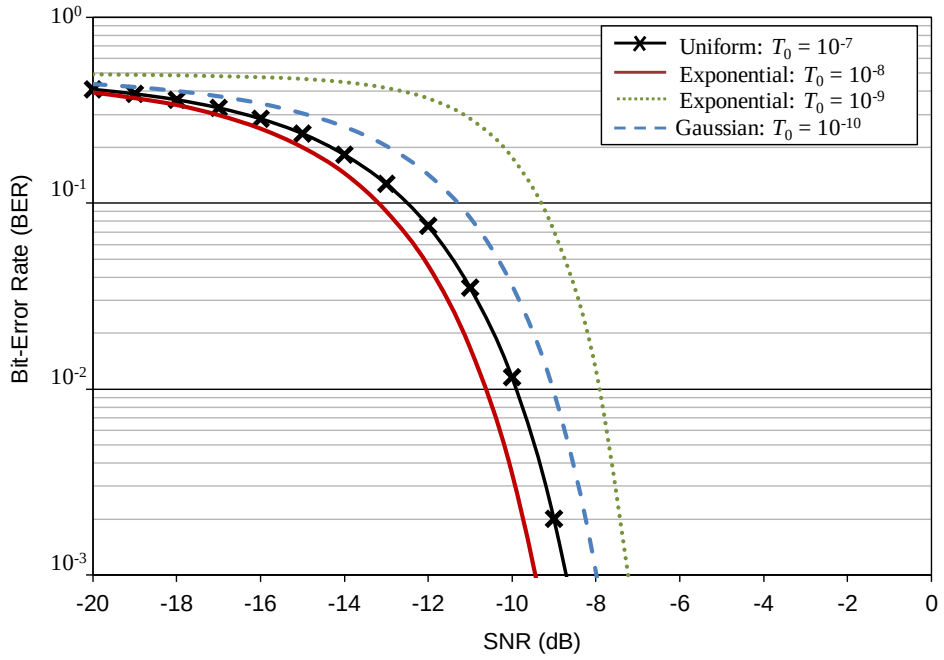


Figure 3.17: BER of the STAP system for different $T_0$, using their best tap distributions, for a *suburban pedestrian* multipath channel.

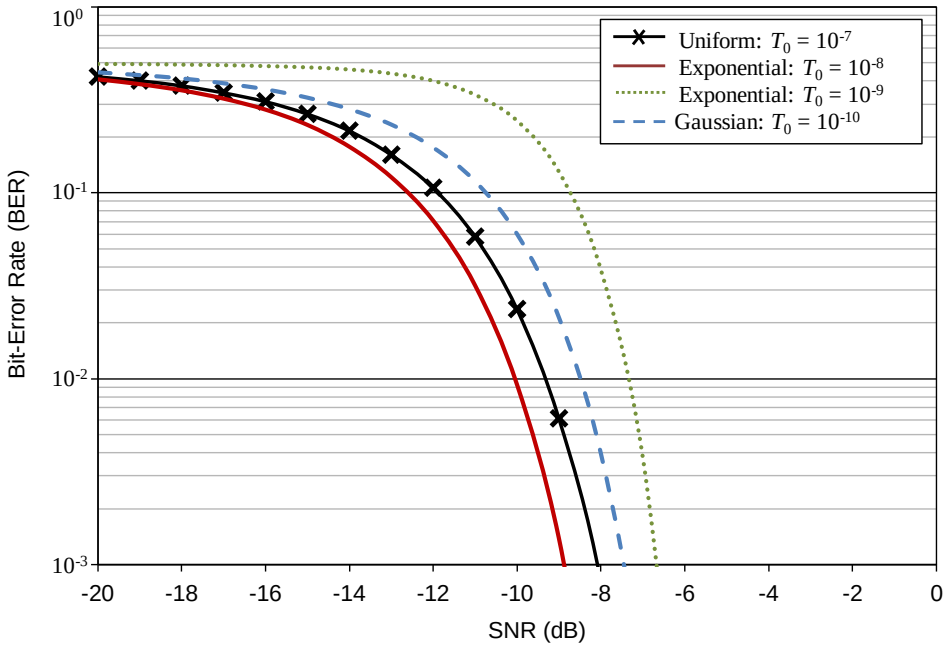


Figure 3.18: BER of the STAP system for different $T_0$, using their best tap distributions, for an *urban car* multipath channel.

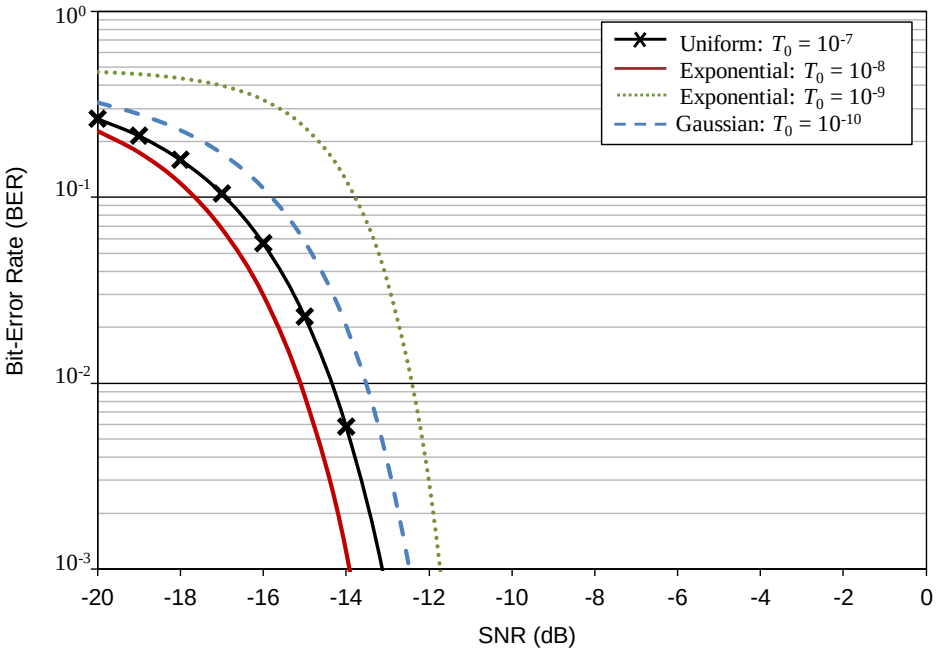


Figure 3.19: BER of the STAP system for different $T_0$, using their best tap distributions, for an *urban pedestrian* multipath channel.

Figures 3.18 and 3.19 display the results for the urban car and urban pedestrian, respectively. It is important to note that, in all the cases, the exponential distribution using $T_0 = 10^{-8}$ (typically used in practice) outperforms the other distributions, including the uniform, without increasing the complexity of the system.

## 3.4 SUMMARY

The focus of this chapter is on the use of *fixed non-uniformly* spaced time delays (i.e., exponential, Rician, Rayleigh, and Gaussian distributions) to improve the performance of STAP in a multipath environment. Multipath channels, developed by an intense campaign of the DLR, were used to simulate multipath propagation. Based on these results, it can be stated that the exponential distribution is an excellent tradeoff between the simplicity of the uniform and the good performance of the computationally intensive tap tracking algorithms.

Table 3.2: Summary of the characteristics for uniform, optimal, and exponential spacings.

| | Uniform | Optimal | Exponential |
|---|---|---|---|
| Simplicity | High | Low | High |
| Real time adaptation | Good | Poor | Good |
| BER performance | Poor | Good | Good |
| Computational efficiency | High | Low | High |

A comparison of the characteristics of the uniform, optimal, and exponential distributions is summarized in Table 3.2, where:

- *Simplicity* refers to the ease of implementation.
- *Real-time adaptation* represents the time necessary to compute the tap spacing.
- *BER* is a measure of the number of errors using the computed time spacings.
- *Computational efficiency* is the ability of the system to find a good solution in a short time.

# Chapter 4

# MICROSTRIP PATCH ANTENNAS

In a GPS, some satellite signals arrive from low elevation angles. However, current GPS antenna arrays are planar (see Figure 4.1), with the main beam pointed toward zenith and having a low directivity for angles near the horizon. Spherical arrays are good alternatives to direct the beam away from zenith because the main beam of each element is pointing toward different directions; thus, they increase the LOS for low elevation angles.

The array used in this research consists of seven cavities with a substrate permittivity of 6 recessed on the surface of a metallic sphere. One cavity is at $\theta = 0^\circ$, while the other six are uniformly placed along the rim of a cone defined by $\theta = 30^\circ$. Each one of these cavities has two circular stacked patches; the top patch is directly fed with a coaxial cable, and the bottom patch is parasitic. The reason for the stacked patches is to obtain two resonances, each one at a GPS band (L1 = 1.575 GHz and L2 = 1.227 GHz) instead of using only one element with a wide bandwidth. This geometry is shown in Figure 4.2, and its dimensions are summarized on Table 4.1.

Table 4.1: Parameters for the geometry of the spherical array

| **Parameters** | **Value** |
|---|---|
| Patch 1 radius | 2.650 cm |
| Patch 2 radius | 2.205 cm |
| Feed radius | 1.087 cm |
| Cavity radius | 3.973 cm |
| Sphere radius | 19.000 cm |
| Separation between the stacked patches | 0.254 cm |
| Separation between the bottom patch and cavity | 0.635 cm |

The number of antenna elements is an essential parameter in the performance of the array. As expected, the more antenna elements are used, the higher the gain is; therefore,

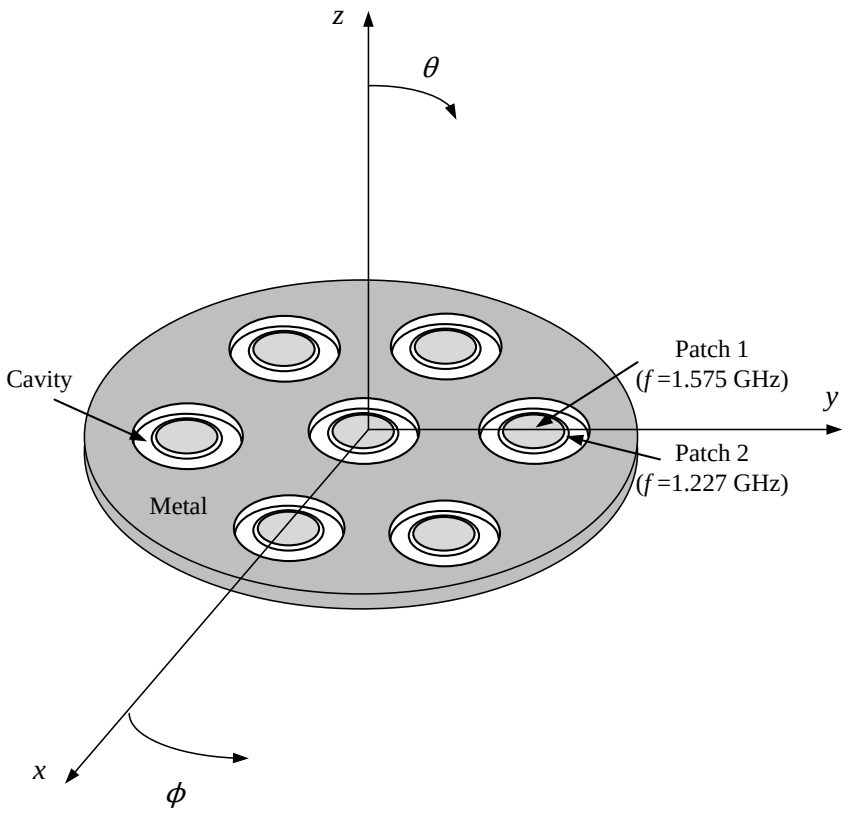


Figure 4.1: Planar array in some GPS receivers.

the BER is lower, as shown in Figure 4.3. In particular, there is a difference of more than 1 dB in the SNR, at a BER of $10^{-3}$, when the number of elements is increased from 7 to 9. Furthermore, it is well known that the number of interferences that can be suppressed by an array is equal to one less than the number of antenna elements; i.e., with more elements, the entire system is more robust to interference environments. From these results, it is ideally desirable to have an infinite number of elements. However, a tradeoff has to be made given that, practically, the array must be finite.

Another important characteristic to take into account about the antenna array is its geometry [64–66]. Although it was previously mentioned that the spherical array is an excellent alternative, because it increases the LOS coverage compared to the planar ground, there are many other non-planar geometries that could also increase the LOS coverage. As

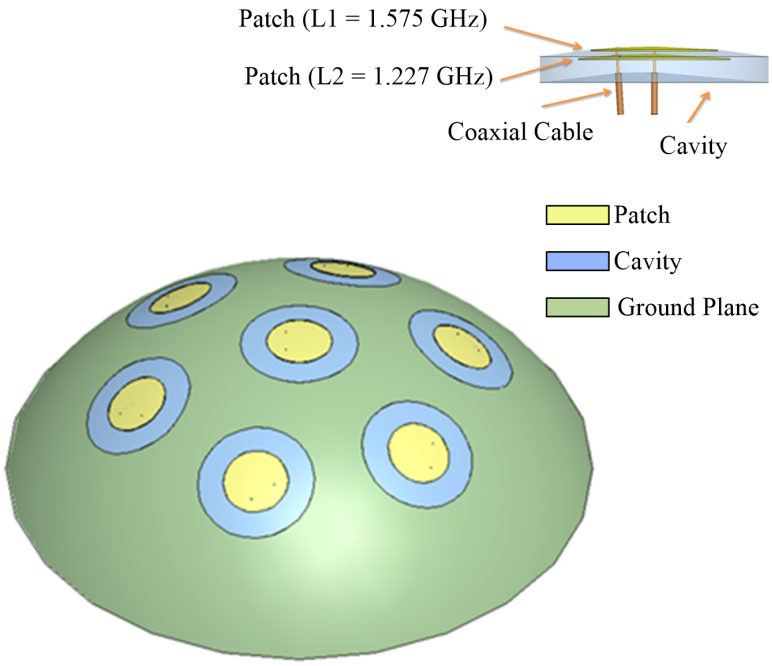


Figure 4.2: Geometry of the array showing the placement of the stacked patches on the sphere and a cross section of one element cavity.

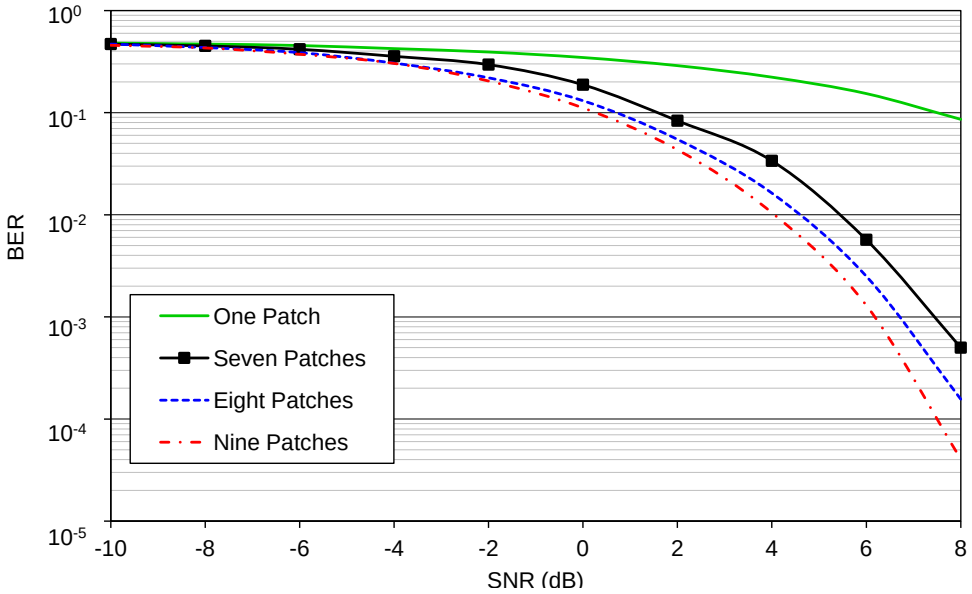


Figure 4.3: BER with different numbers of antenna elements. The results for one, six, eight, and nine patches demonstrate that the BER decreases as the number of patches increases.

an example, two new non-planar geometries, shown in Figure 4.4, were considered for comparison with the spherical ground. Both are based on hexagonal patterns and designed to be circumscribed in the spherical cap. In fact, the truncated hexagonal pyramid was considered as an alternative antenna configuration for wireless communications systems [67].

As part of these new designs, the dimensions of the patches were adjusted to operate at the two GPS bands, as seen in Figure 4.5. The new values are 2.196 cm and 2.550 cm for the radius of the top and bottom patches, respectively. All other dimensions remain the same as in the spherical array.

The BER of these new geometries was compared with that of the spherical cap, and the results are displayed in Figure 4.6. It is apparent that these geometries do not have a significant impact on the performance of the system for signals arriving from $\theta = 0^{\circ}$. In other words, the BER of the system remains basically the same with these new geometries as long as the number of elements is maintained constant. However, other factors are impacted; in particular, the LOS changes as the angle of the elements is changed.

After the impact of the number of elements and geometry in the performance of the system has been illustrated, the remainder of this chapter is devoted to improve the performance of the antenna. The chapter is divided into two parts: (1) single-element and (2) antenna array. In the first part, a new hybrid substrate is proposed, and its performance is compared with that of the conventional dielectric design. The optimal dimensions of the hybrid design are analyzed using the maximum gain as a criterion. The second part consists of the implementation of this new substrate to reduce the reflection coefficient in phased arrays, as the main beam is scanned from broadside to endfire. It is important to clarify that the frequencies of operation for simulations in this chapter are not necessarily those of the GPS bands to compare the performance of the proposed configuration with previous designs.

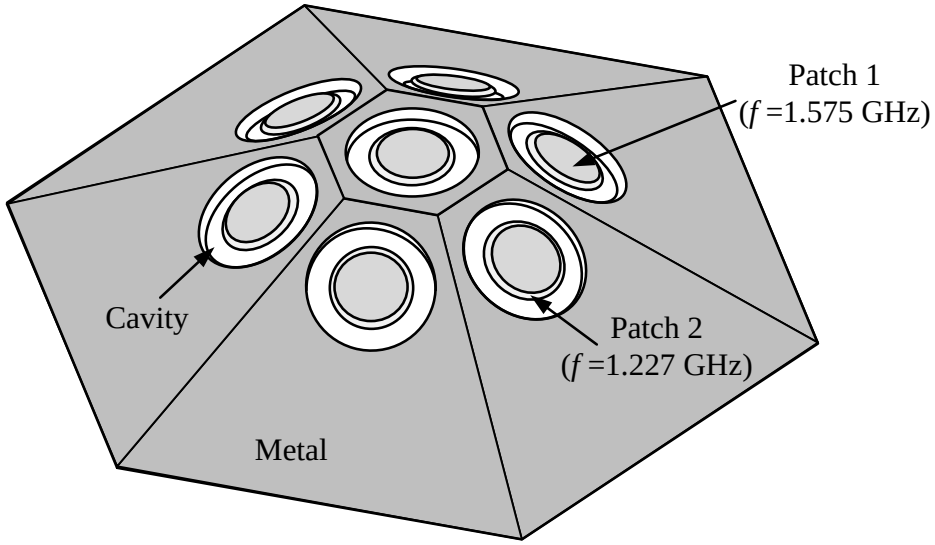


(a)

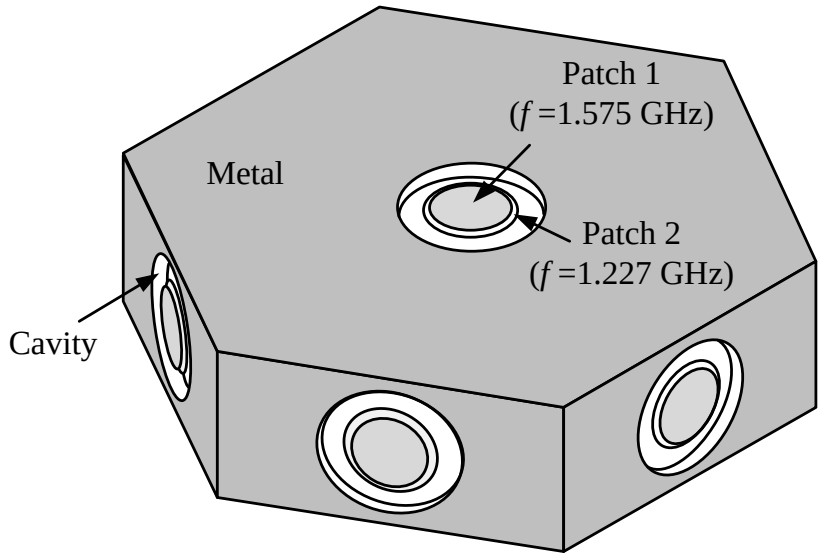


(b)

Figure 4.4: Hexagonal antenna arrays. (a) Truncated hexagonal pyramid. (b) Flat hexagon.

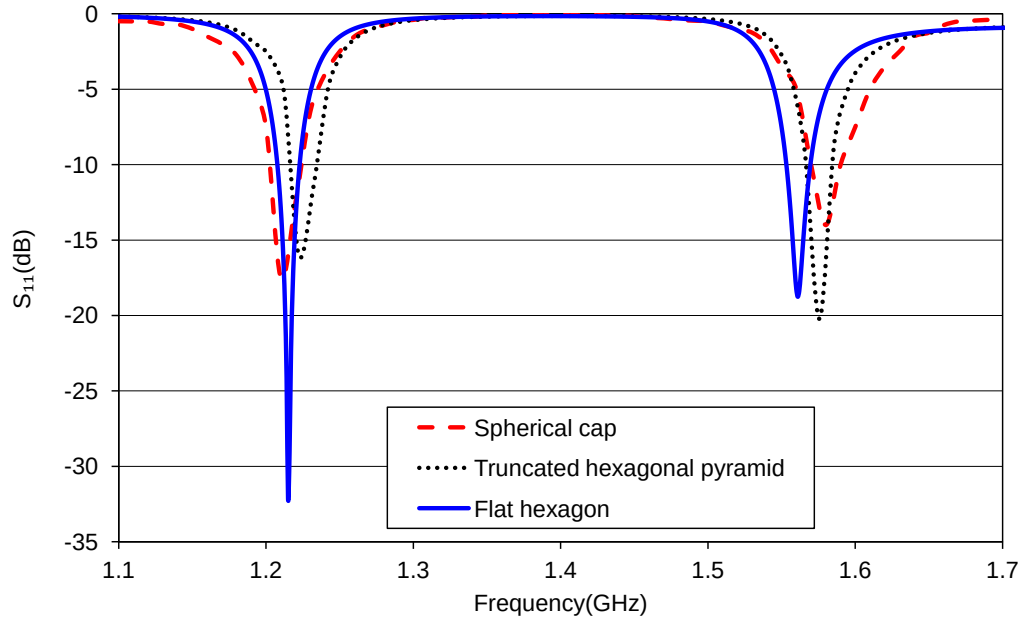


Figure 4.5: $S_{11}$ for different antenna geometries. As can be noted, the arrays were designed to operate at two GPS frequencies (L1 and L2).

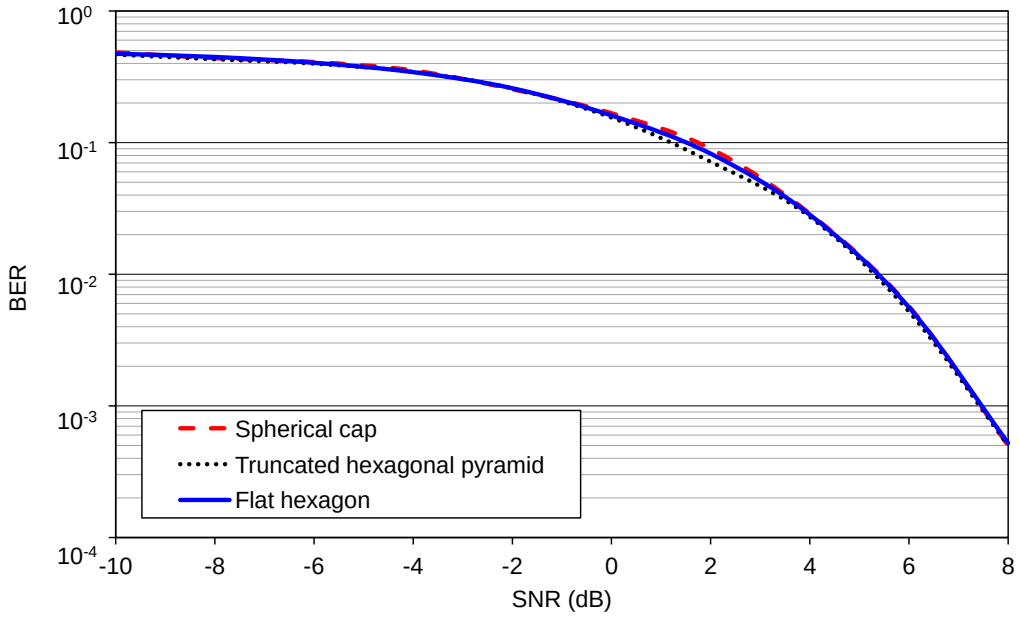


Figure 4.6: BER for different array geometries. Clearly, the geometry in these cases does not impact the BER.

## 4.1 SINGLE ELEMENT PATCH ANTENNA

The highly desirable features of microstrip antennas, such as performance, flexibility, simplicity, and low fabrication cost, make them very popular for many applications. Their conventional design consists of a metallic patch (usually square or circular) on top of a dielectric substrate. When the antenna is energized, waves can propagate in all directions. Some of these waves, referred to as *surface waves*, travel in the substrate and do not contribute to the main radiation. Therefore, some energy is lost in these directions, limiting the maximum achievable gain between 5 to 9 dB for these radiating elements [3]. Moreover, when these elements are used in an array, surface waves are primarily responsible for scan blindness [68, 69]. These drawbacks limit the range of applications in which these elements can be used. Over the years, several alternatives have been proposed to overcome the gain limitation, usually at the expense of a reduction in the impedance bandwidth. Electromagnetic Band Gap (EBG) or Photonic Band Gap (PBG) surfaces are one of the most popular alternatives, because of their ability to suppress the propagation of electromagnetic waves in a frequency band [70]. The suppression of electromagnetic waves leads to a significant enhancement of the maximum gain when a microstrip patch antenna is placed above one of these surfaces [71, 72]. To increase the impedance bandwidth, EBG/ferrite surfaces and self-structuring configurations have been proposed [73–76]. However, the drawback is the complexity of construction because many of these designs include a large number of vias.

As an alternative to eliminate these drawbacks, a new substrate configuration is proposed as shown in Figure 4.7. This technique consists of incorporating an unbiased ferrite ring into a conventional dielectric. As can be seen from the figure, a conventional dielectric is used below the patch, and the ferrite ring has the same thickness $h$ as the dielectric. The degrees of freedom of this configuration are given by the permittivities, permeabilities, the number of interfaces, and the sizes of the materials. The circular patch and cylindrical configuration were chosen because of their azimuthal symmetry.

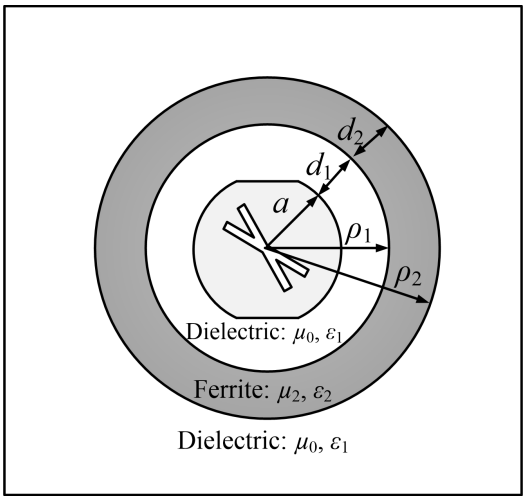


(a)

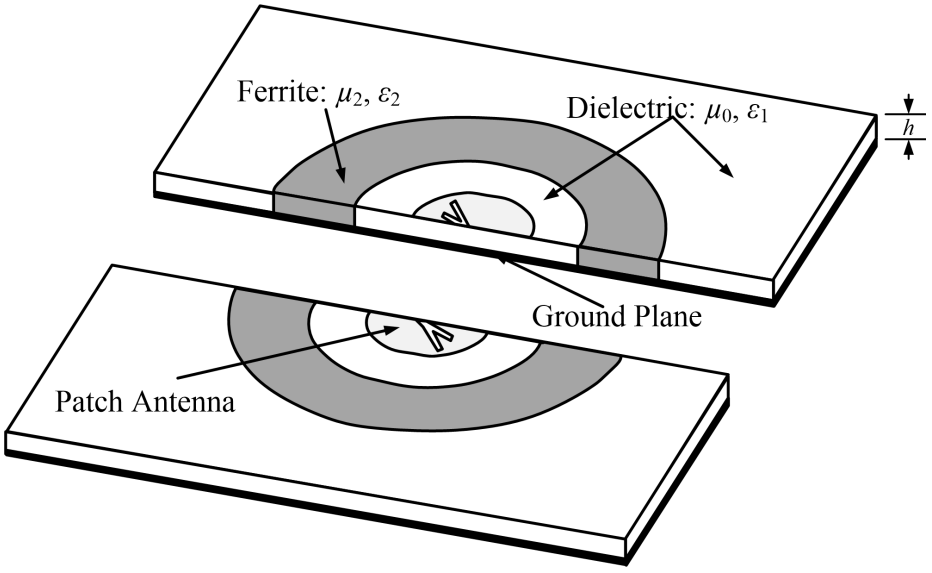


(b)

Figure 4.7: Proposed substrate structure, including the dielectric and a ferrite ring. (a) Top view. (b) Cross section view.

Two interfaces have been created between the dielectric and the ferrite. The first interface, *dielectric-ferrite*, is at a distance $\rho_1$ from the center of the geometry, while the second interface, *ferrite-dielectric*, is at a radial position $\rho_2$. Therefore, $d_1$ ($d_1 = \rho_1 - a$; $a$ is the radius of patch) denotes the distance from the patch circumference to the first interface, and $d_2$ ($d_2 = \rho_2 - \rho_1$) represents the width of the ferrite ring.

When the wave travels out of the antenna encounters an interface between two materials, part of the energy is transmitted, and some is reflected [63]. The reflections, combined with the incident field, create constructive or destructive interference depending on the characteristics of the materials. The reflected field can then enhance the maximum antenna gain by reducing the surface wave propagation in the substrate.

The interference between the incident and reflected waves is created by the permittivities of both materials, the permeability of the ferrite, and the distances $d_1$ and $d_2$.

*Gain and Bandwidth*

To analyze the performance of the proposed configuration, a circular microstrip patch antenna was designed using a Rogers TMM4 substrate (relative permittivity of $\varepsilon_r = 4.5$) with thickness $h = 3.2$ mm, radius $a = 5.5$ mm, and operating frequency of 5.8 GHz. To increase the bandwidth and to create circular polarization with a single feed, two slots were introduced on the circular patch with a width and length of 0.6 mm and 7.0 mm, respectively [71]. This design is shown in Figure 4.8.

Initial values of $d_1$ and $d_2$ of one-quarter of the free-space wavelength ($d_1 = d_2 = \lambda_0/4$) were selected. An unbiased ferrite, with a relative permeability of $\mu_r = 14$, relative permittivity of $\varepsilon_r = 10$, dielectric loss tangent tan $\delta_e = 0.0017$, and magnetic loss tangent tan $\delta_m = 0.0391$ [77], was used.

Using HFSS [78], the results of the patch antenna above a dielectric (i.e., no ferrite ring) and above the proposed substrates were compared. For simplicity, we refer to

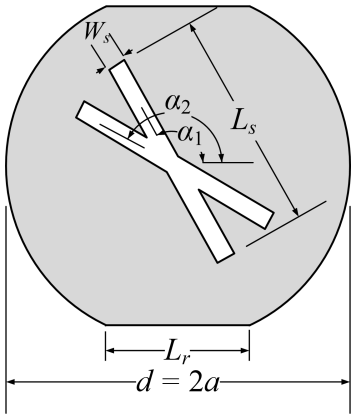


Figure 4.8: The geometry of the circular microstrip patch antenna. For a design frequency of 5.8 GHz: $a = 5.50$ mm, $L_s = 7.00$ mm, $W_s = 0.60$ mm, $L_r = 4.58$ mm, $\alpha_1 = 120^\circ$, $\alpha_2 = 165^\circ$, and $h = 3.20$ mm. Substrate size 100 mm by 100 mm.

the former as the *conventional substrate* and to the latter (dielectric-ferrite) as the *hybrid substrate*.

The 3D gain patterns (not taking into account mismatches) of both configurations are illustrated in Figure 4.9. Clearly, the hybrid substrate results in a more directional pattern compared with the conventional substrate. Two-dimensional E-plane patterns indicate the enhancement of about 3.5 dB when the hybrid substrate is used (see Figure 4.10). From Figure 4.10, it can be observed that the addition of the ferrite ring makes the antenna focus more energy toward broadside and makes it radiate less energy toward low elevation angles, unlike the conventional substrate.

The maximum gain can be impacted by the ferrite magnetic losses as illustrated in Figure 4.11, for values of magnetic loss tangent up to tan $\delta_m = 0.05$. A value of tan $\delta_m = 0.0391$ was selected from [77] to generate the results shown in this chapter. However, as the magnetic losses are reduced, the gain can increase up to a maximum of 9.41 dB. The reason that a significant gain enhancement (compared to the conventional case) can be achieved for values up to tan $\delta_m = 0.05$ is because the ferrite ring is not underneath the

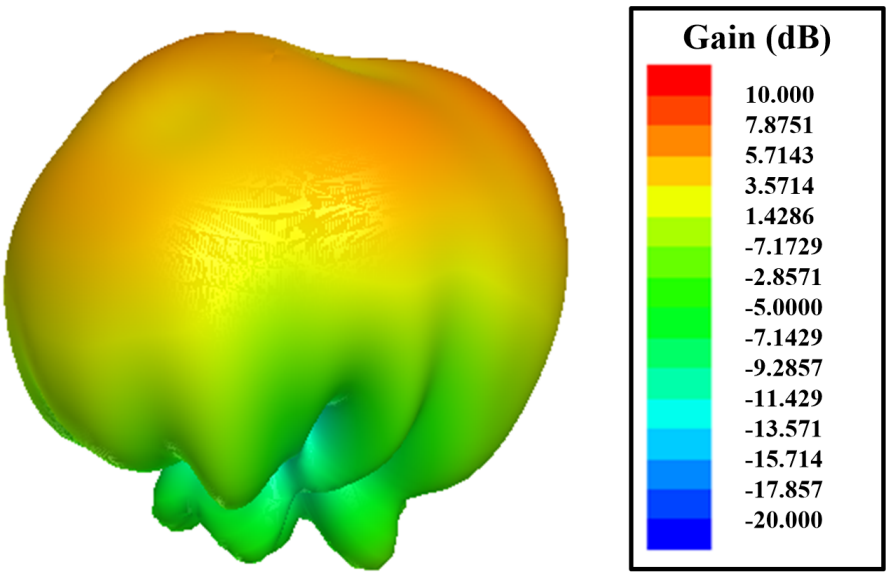


(a)

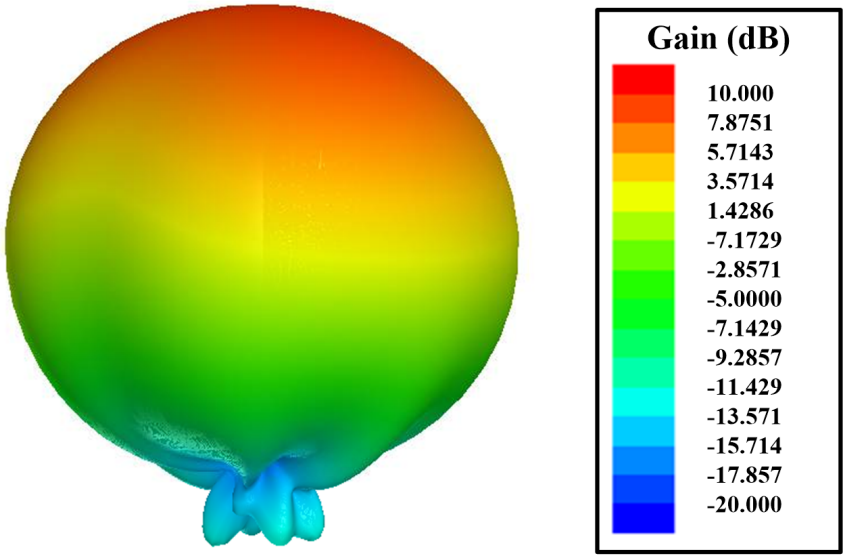


(b)

Figure 4.9: 3D gain pattern of circular microstrip patch. (a) Conventional substrate (maximum gain = 4.61 dB). (b) Hybrid substrate (maximum gain = 8.10 dB).

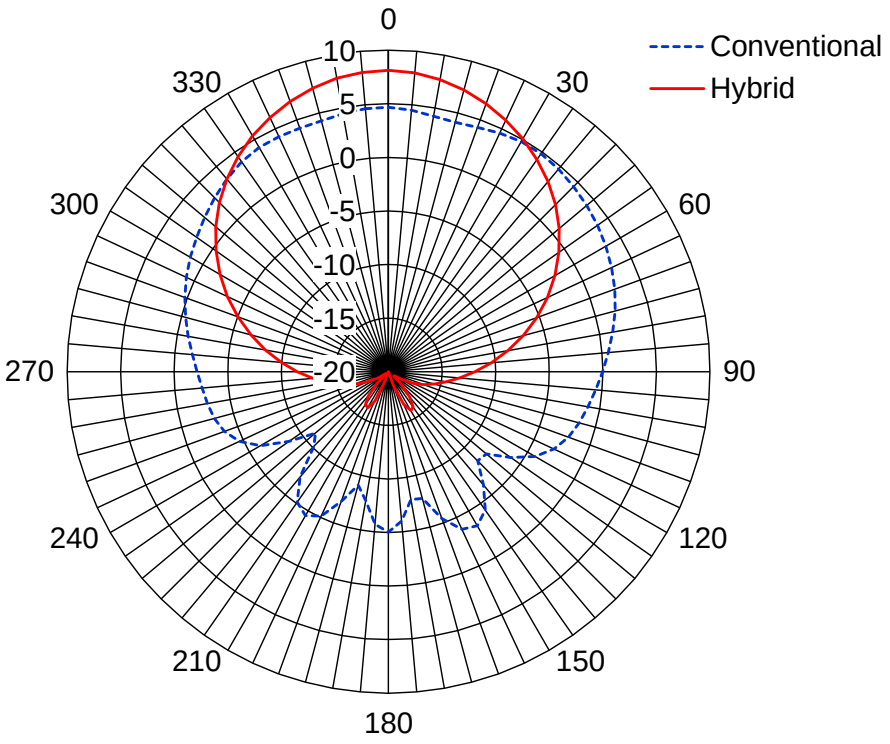


Figure 4.10: E-plane gain pattern (in dB) for conventional (dashed line) and hybrid (solid line) substrates.

patch but rather a distance $d_1$ away from its circumference; thus, the gain degradation is not as large as using an entire ferrite substrate.

The next step was to analyze the electric fields in both substrates (conventional and hybrid). Figure 4.12 shows a top view of the E-field intensity in the two designs. It can be noted from Figure 4.12(a) that, for the conventional substrate, the intensity of the fields is very low. However, using the hybrid substrate [see Figure 4.12(b)], the intensity of the fields is low on the dielectric but significantly higher on the ferrite ring. It is evident that there is constructive interference in the fields inside the ferrite ring.

The normalized field intensity inside the substrate along the E-plane (from the edge of the patch antenna to the end of the substrate) is displayed in Figure 4.13. It can be seen that the field intensity on the ferrite is as high as six times larger than the intensity in the

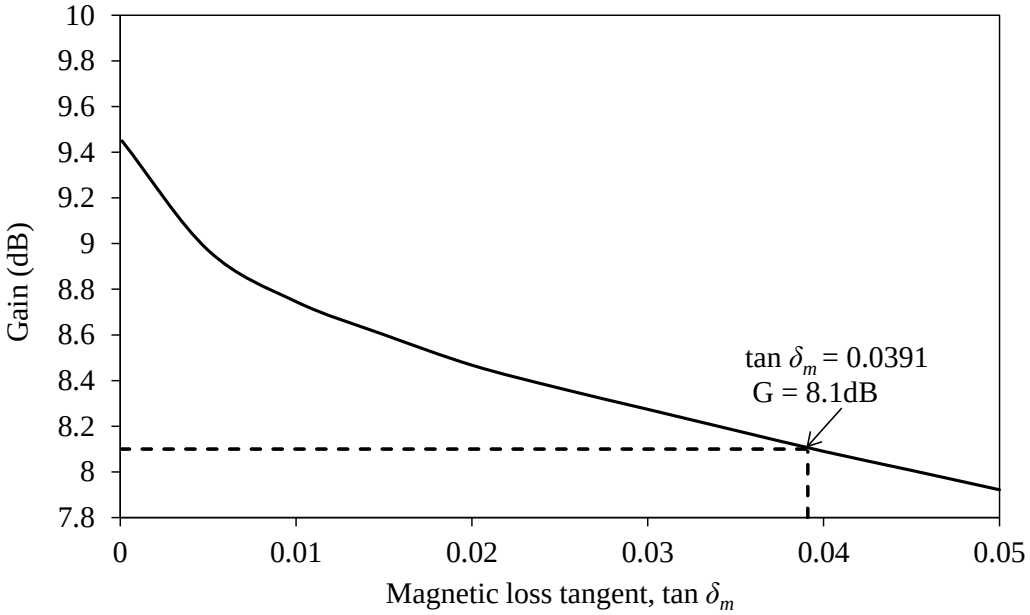


Figure 4.11: Gain variation as a function of the magnetic loss tangent tan $\delta_m$.

conventional substrate. Several simulations (not shown here) demonstrated that, whenever this high intensity is observed, the antenna exhibits a high gain.

Another important characteristic of microstrip patch antennas is the impedance bandwidth, which in most cases is reduced as the gain is increased. However, as shown in Figure 4.14, the bandwidth of the proposed configuration is not reduced but increased. A bandwidth of 7.8% is achieved using the hybrid substrate, while only a 6.7% bandwidth is obtained for the conventional substrate (using $S_{11}$ = -10 dB as a criterion). Therefore, by using the new design, an enhancement of about 1% in the impedance bandwidth is attained.

Furthermore, the hybrid substrate exhibits an even better $S_{11}$ compared to the conventional substrate when a 50Ω coaxial cable is used to feed the microstrip antenna. This improvement in the matching leads to a more efficient design, which also leads to a higher absolute gain [3].

The hybrid substrate achieves a gain greater than 6.50 dB within the frequency range of 5.5 GHz to 6 GHz, with an average of 8.13 dB, as shown in Figure 4.15. On

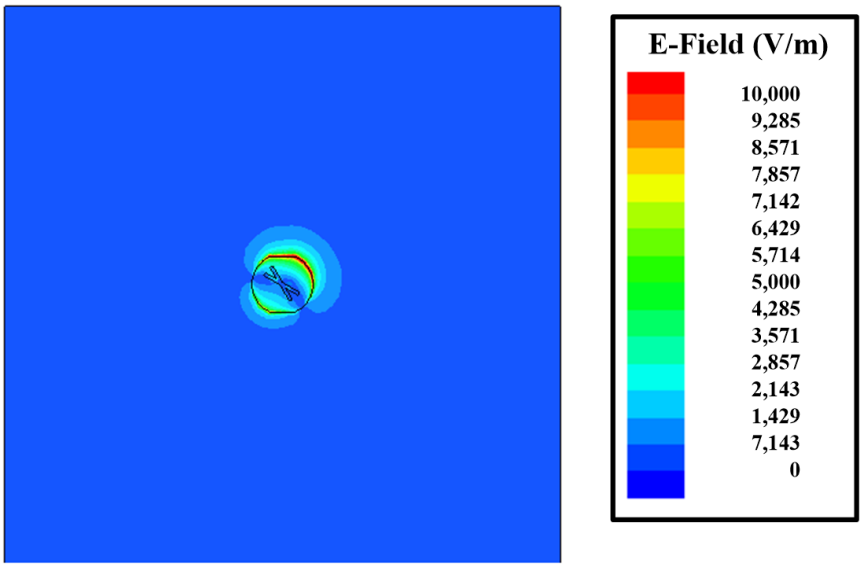


(a)

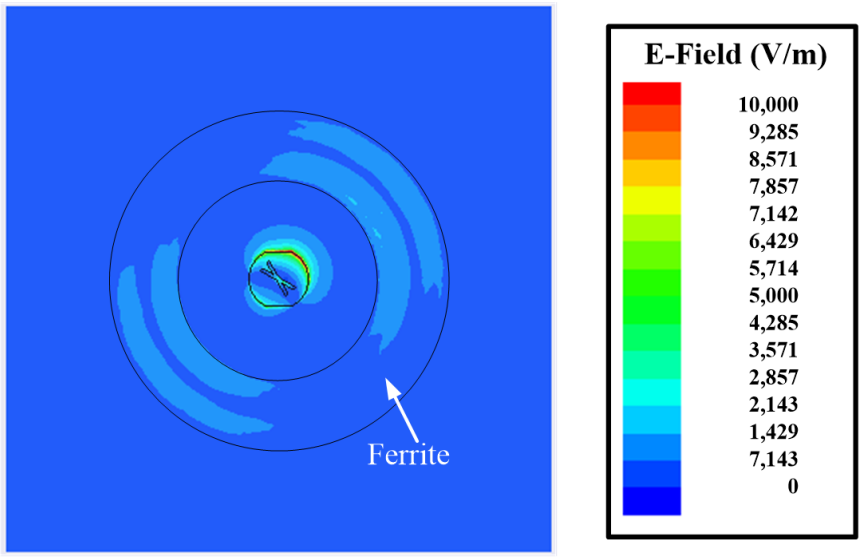


(b)

Figure 4.12: Electric field magnitude on the surface of the microstrip patch and substrate. (a) Conventional substrate. (b) Hybrid substrate.

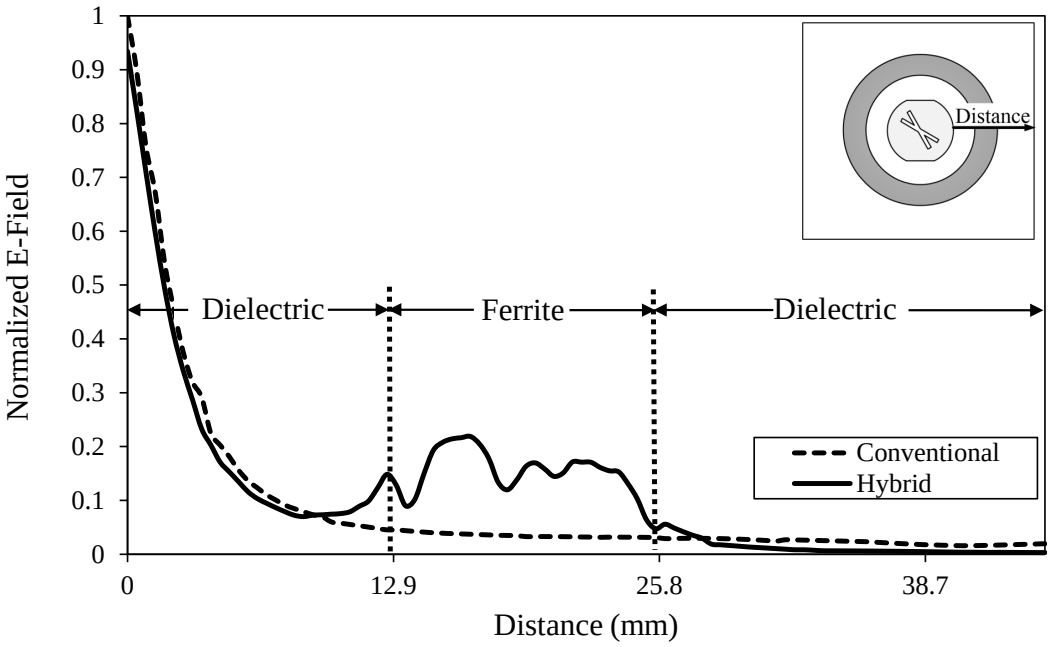


Figure 4.13: E-field normalized magnitude inside the substrate for conventional (dashed line) and hybrid (solid line) configurations.

the other hand, the conventional substrate attains a maximum gain of 5.37 dB in the same frequency range with an average of 4.40 dB. Clearly, the response of the proposed hybrid substrate structure exhibits performance enhancements in the impedance bandwidth as well as the gain.

*Maximum Gain*

A parametric study was performed to determine the optimal distances $d_1$ and $d_2$, using the maximum gain as a criterion. The gain was calculated for values of $d_1$ and $d_2$ from $0.125\lambda_0$ to $0.375\lambda_0$ in steps of $0.0625\lambda_0$. In this case, to reduce the computational time, a circular patch with no slots and radius $a = 6.2$ mm was used. The distance $d_3$ from the outer circumference of the ferrite ring to the edge of the substrate was $\lambda_0/4$.

Figure 4.16 displays the results of the parametric investigation, in which the gain was calculated as a function of $d_2$ for different values of $d_1$. The maximum gain, for all

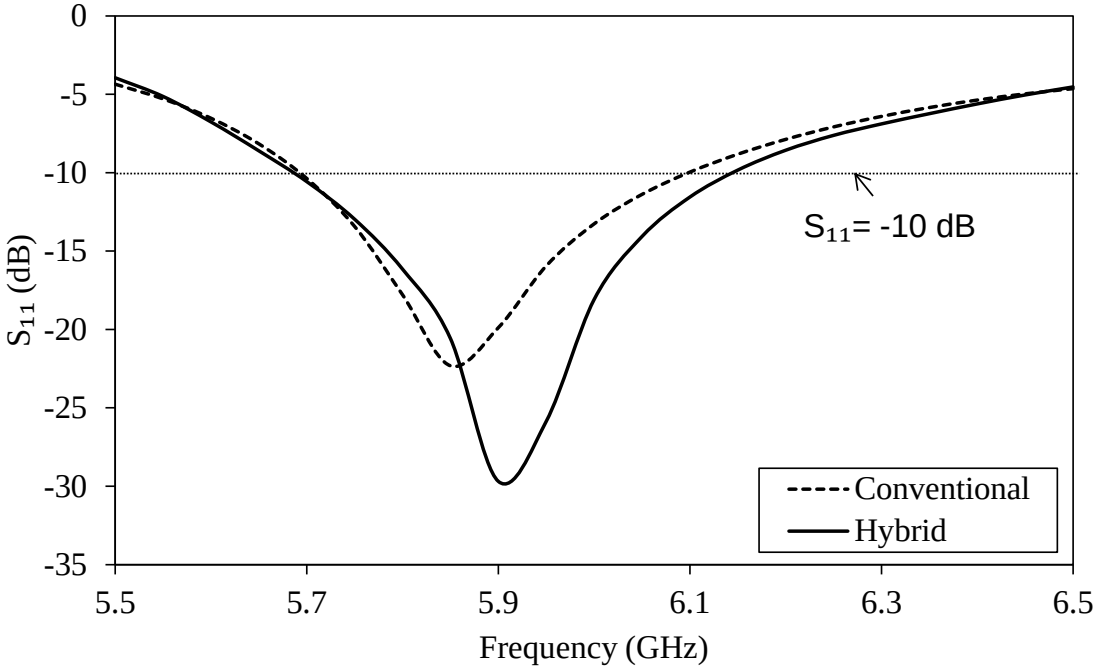


Figure 4.14: $S_{11}$ for a circular patch above conventional (dashed line) and hybrid (solid line) substrates.

the values of $d_1$, is achieved when $d_2$ equals one-quarter of the free-space wavelength. In addition, the maximum gain is achieved when $d_1$ is $3\lambda_0/16$ and $\lambda_0/4$, where $\lambda_0$ is the free-space wavelength. Therefore, the optimal values for $d_1$ as well as $d_2$ are nearly one-quarter of the free-space wavelength.

It is important to observe that the value $d_2$ is more critical than that of $d_1$ in maximizing the gain; i.e., the maximum gain is more sensitive to changes in $d_2$ than to changes in $d_1$. For the results displayed in Figure 4.16, the value of the gain does not change by more than 2 dB when $d_2 = \lambda_0/4$, while for $d_1 = \lambda_0/4$, the change in the gain is more than 6 dB by varying $d_2$.

*Material Selection*

The ferrite was replaced with dielectric material to investigate the combination of different dielectric materials in the hybrid configuration. The process consisted of the selection of

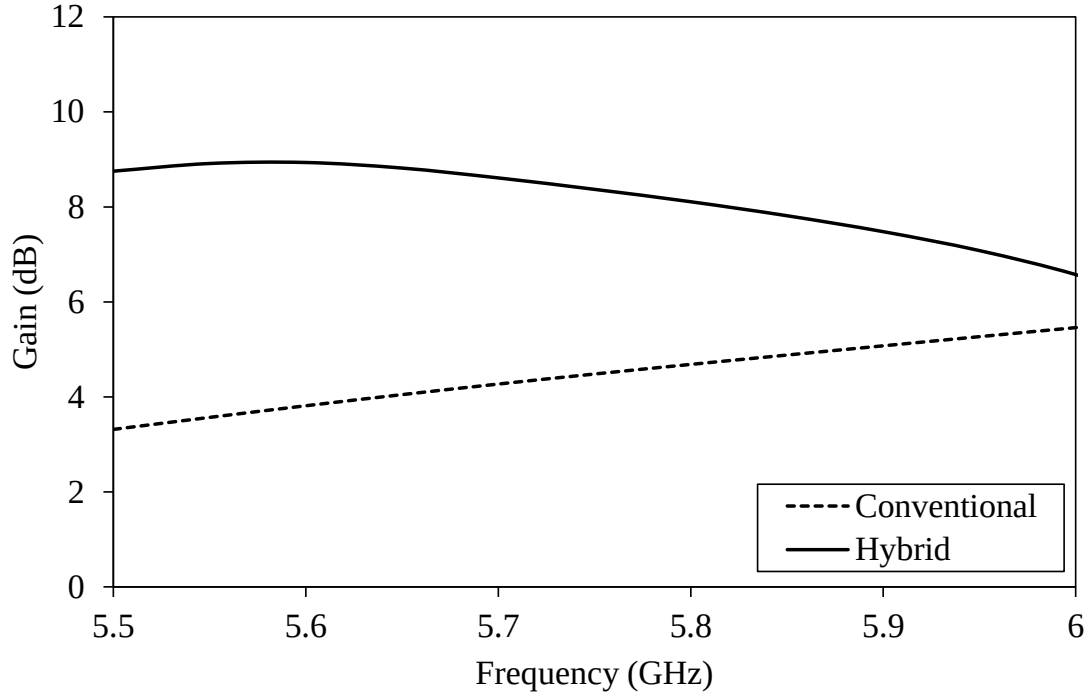


Figure 4.15: Frequency response of the gain using conventional (dashed line) and hybrid (solid line) substrates.

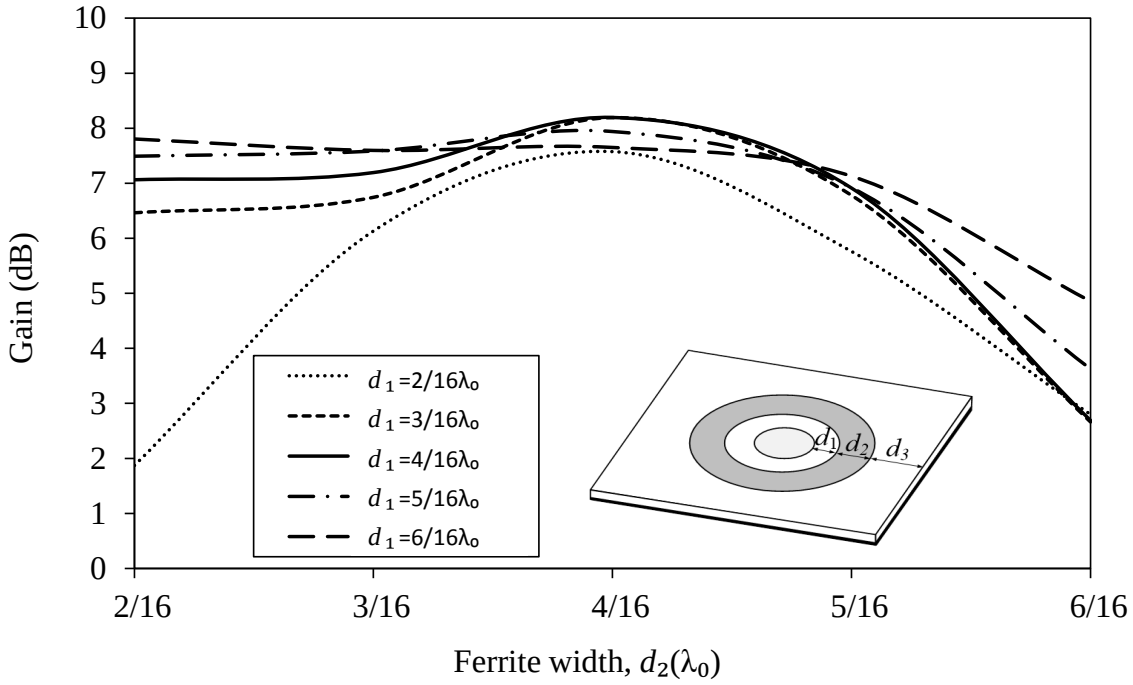


Figure 4.16: Maximum gain as a function of $d_1$ and $d_2$ for a circular patch.

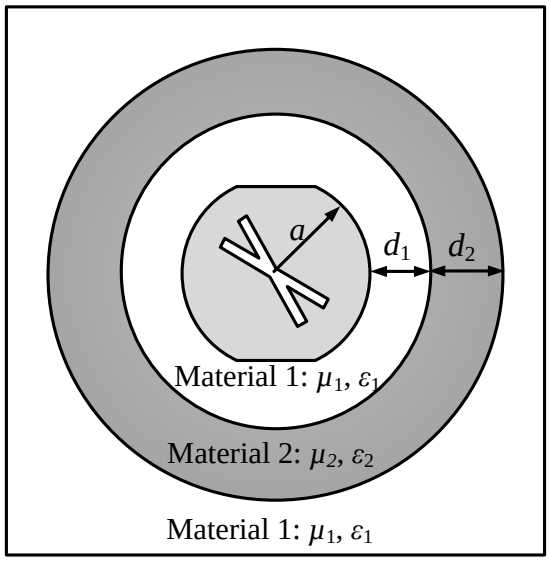


Figure 4.17: Proposed substrate structure to generate constructive interference between the incident and reflected fields.

different permittivities for Material 1 and Material 2 (see Figure 4.17) while using relative permeabilities of unity (i.e., $\mu_1 = \mu_2 = \mu_0$).

The selected relative permittivities for Material 1 are 2.3, 4.5, and 6.15. In the case of Material 2, the values are 2.2, 6.15, and 10.2. These values result in 8 different combinations that generate reflections. These combinations are listed in Table 4.2.

For each one of these combinations, a parametric study was performed to determine the distance $d_2$ that results in the maximum gain for the respective combination.

The first step was to adjust the radius of the antenna to resonate at 5.8 GHz using the conventional dielectric (i.e., no ring) with a permittivity $\varepsilon_1 = \varepsilon_{r1}\varepsilon_0$. In other words, the procedure started with the design of the microstrip circular patch element with a substrate with relative permittivities of 2.3, 4.5, and 6.15.

Table 4.2: Combinations of permittivity values to study hybrid configurations.

| Combination | Permittivity of Material 1 $\varepsilon_{r1}$ | Permittivity of Material 2 $\varepsilon_{r2}$ |
|---|---|---|
| 1 | 2.3 | 2.2 |
| 2 | 2.3 | 6.15 |
| 3 | 2.3 | 10.2 |
| 4 | 4.5 | 2.2 |
| 5 | 4.5 | 6.15 |
| 6 | 4.5 | 10.2 |
| 7 | 6.15 | 2.2 |
| 8 | 6.15 | 10.2 |

Table 4.3: Gain for the conventional dielectric configuration using three different values for the relative permittivity of the substrate.

| Relative permittivity, $\varepsilon_{r1}$ | Radius of the microstrip patch (mm) | Gain (dB) |
|---|---|---|
| 2.3 | 8.7 | 5.85 |
| 4.5 | 5.5 | 4.68 |
| 6.15 | 4.5 | 3.10 |

For these three cases, the broadside gain was calculated, and the results are summarized in Table 4.3. After the calculation of the gain without the ring, the next step was to incorporate the ring and perform the parametric study. The approach to analyze each one of the combinations consisted of selecting a given value of $d_1$ and varying $d_2$ to obtain the maximum gain. The results from the previous section illustrate that $d_2$ has a greater impact on the gain than $d_1$. Therefore, to reduce the computational burden of the parametric study, the distance from the antenna to the ring $d_1$ was fixed to one-quarter of the free-space wavelength.

Figures 4.18 to 4.20 illustrate the results for $\varepsilon_{r1}$ equal to 2.3, 4.5, and 6.15, respectively. In all the simulations, it was observed that the maximum gain was achieved by using

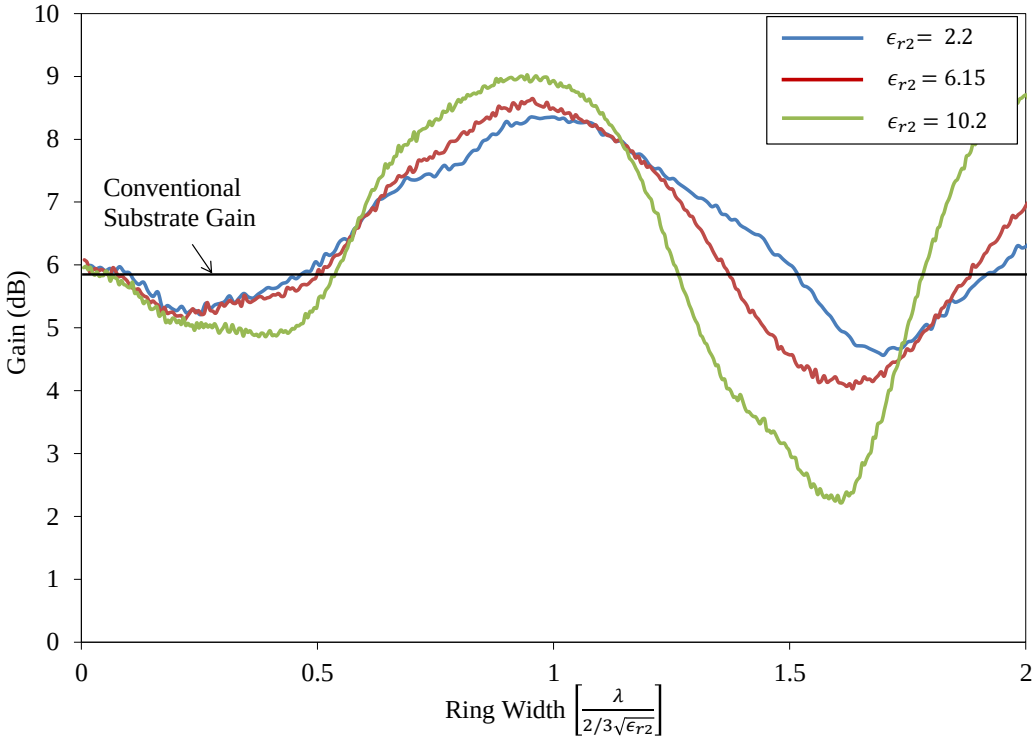


Figure 4.18: Gain for the hybrid configuration when Material 1 has a relative permittivity of 2.33.

a distance of

$$d_2 = 3/2\sqrt{\varepsilon_{r2}}\lambda \tag{4.1}$$

where $\lambda$ is the wavelength in Material 2. Therefore, to simplify the analysis and comparison of the gain enhancement, the ring width $d_2$ (in Figures 4.18 to 4.20) has been normalized by a factor of $2/3\sqrt{\varepsilon_{r2}}$.

Figure 4.18 illustrates the gain when the Material 1 has a relative permittivity of 2.3 (combinations 1-3 in Table 4.2). For this permittivity, the conventional dielectric (i.e., no ring) exhibits a gain of 5.85 dB, as shown in Figure 4.18 by the horizontal black line. By comparing the gain of the conventional configuration with that of the hybrid configuration, an enhancement of the gain can be achieved whenever the normalized ring width is larger than 0.6 and less than 1.2 for any $\varepsilon_{r2}$.

Another important result is that, as $\varepsilon_{r2}$ increases, the range of values of the ring width that enhance the gain is narrower. For example, the normalized ring width values that enhance the gain extend up to 1.6 when $\varepsilon_{r2} = 2.2$, while the maximum is 1.2 when $\varepsilon_{r2} = 10.2$. However, as $\varepsilon_{r2}$ increases, the maximum enhancement in the gain also increases. For instance, the maximum achieved gain with $\varepsilon_{r2} = 2.2$ is around 8 dB, but for $\varepsilon_{r2} = 10.2$, it is 9 dB, resulting in a gain difference of 1 dB by changing the permittivity of Material 2. In addition, multiple gain maxima are generated because, for normalized ring width values of 2, the gain is again larger than the conventional substrate case.

Figure 4.19 shows the results when $\varepsilon_{r1} = 4.5$ (combinations 4-6 in Table 4.2). Similar trends are observed for this permittivity: as $\varepsilon_{r2}$ increases, greater enhancement of the gain is attained. However, the range of values of the ring width over which these increases occur is smaller. It is important to observe that the gain enhancement in this case is larger than the case for $\varepsilon_{r1} = 2.33$. For instance, for $\varepsilon_{r1} = 2.33$, the maximum gain enhancement is around 3.12 dB, while for $\varepsilon_{r1} = 4.5$, the gain enhancement is 3.80 dB.

Similar results are shown in Figure 4.20 when $\varepsilon_{r1} = 6.15$ (combinations 7-8 in Table 4.2). In this case, the enhancement is larger than in the previous two cases, achieving a gain improvement of 5 dB.

Figure 4.21 illustrates the maximum gain enhancement as a function of the relative permittivity for Material 2 using a different relative permittivity for Material 1. From the results of this figure, it is evident that, as the relative permittivity of both materials increases, the gain also increases. This means that the largest gain enhancement can be attained for large permittivities in both materials.

After these material combinations were analyzed, it can be concluded that:

- As the permittivities of the materials increase, the gain enhancement is larger.

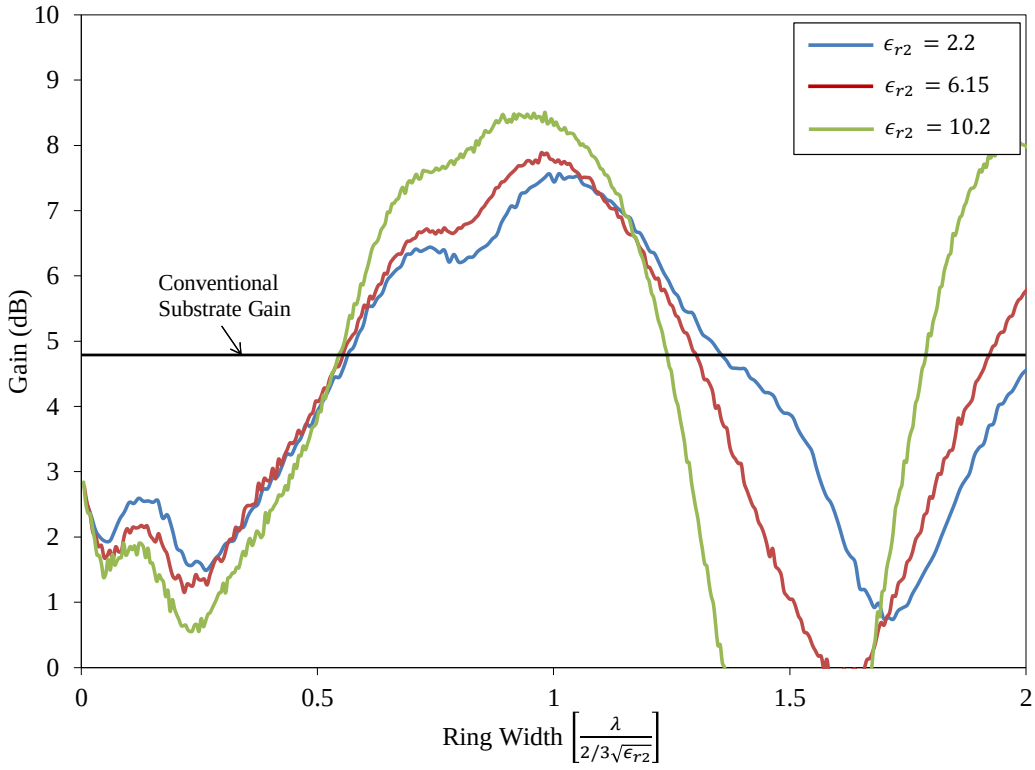


Figure 4.19: Gain for the hybrid configuration when Material 1 has a relative permittivity of 4.5.

- As the permittivity of Material 2 increases, the range of values for the ring width that enhances the gain decreases.
- The maximum gain is achieved for a ring width of

$$d_2 = 3/2\sqrt{\varepsilon_{r2}}\lambda. \tag{4.2}$$

- Multiple gain maxima can be achieved.

However, to achieve these distances (i.e., $d_1 = \lambda_0/4$ and $d_2 = 3/2\sqrt{\varepsilon_{r2}}\lambda$), the size of the substrate should be larger than that of the ferrite case. Therefore, to keep a small size for the single element antenna, the most attractive option is the use of a ferrite ring instead of a dielectric one.

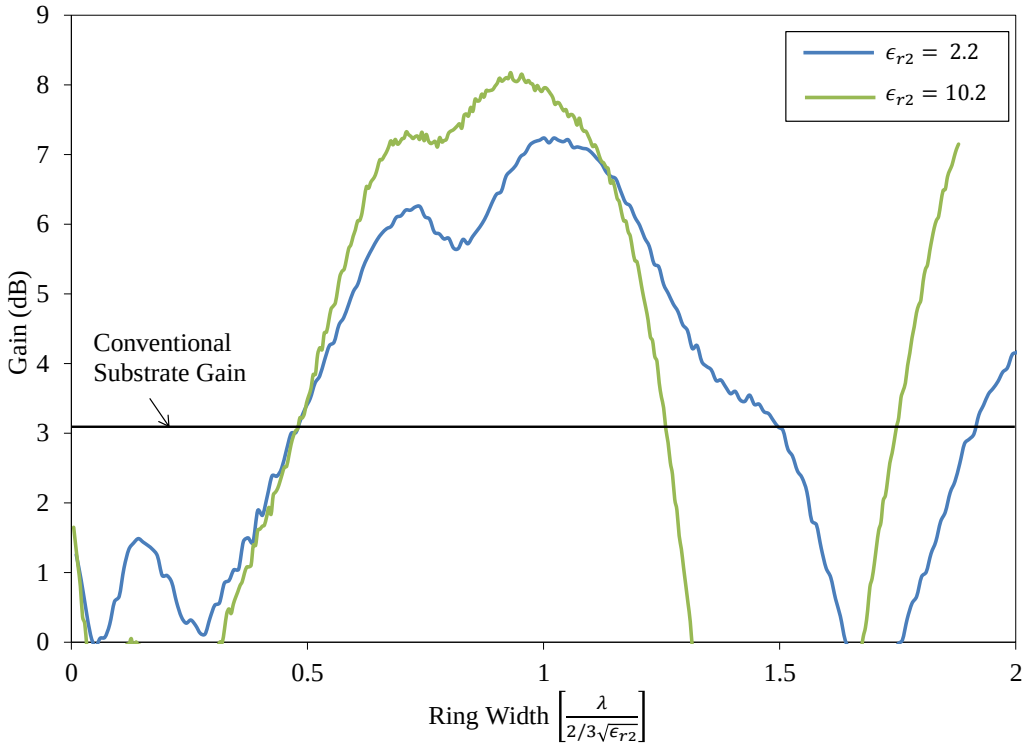


Figure 4.20: Gain for the hybrid configuration when Material 1 has a relative permittivity of 6.15.

*Ring and Patch Shape*

An analysis of combinations of square and circular geometries is performed; i.e., a circular patch with a square ring, a square patch with a circular ring, and a square patch with a square ring. The aim is to investigate which of these configurations attain the largest gain or if there is a significant difference in the performance of different geometries.

A parametric study was performed to analyze each one of the combinations with square and circular geometries. A dielectric material with the relative permittivity $\varepsilon_r = 4.5$ and a ferrite with a relative permittivity of 10 and a relative permeability of 14 were used. Both materials have a thickness $h = 3.2$ mm. The dimensions of the microstrip patch

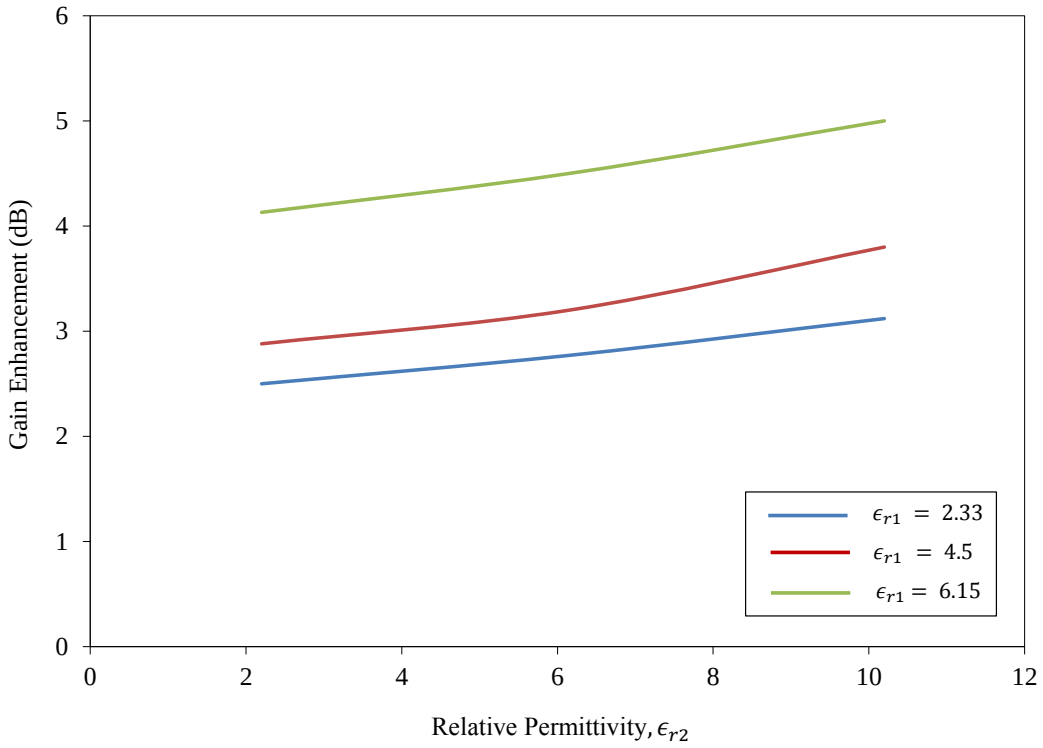


Figure 4.21: Gain enhancement for combinations of different permitivities for Material 1 and Material 2.

antenna were adjusted (for the circular and square geometries) to resonate at 5.8 GHz in the conventional substrate (i.e., no ring). Each configuration and its respective results follow.

Circular Patch with Square Ring

For the first case, the circular ring is replaced by a square ring, as shown in Figure 4.22. It is expected that the optimal dimensions are not necessarily the same as those of the previous cases because of the asymmetry in this configuration (a circular patch with a square ring). However, in the previous sections, it was demonstrated that the distance $d_1$ is not as significant as the distance $d_2$; thus, to simplify the process, $d_1$ was fixed to $\lambda_0/4$.

For the parametric analysis, the gain in the broadside direction was calculated for different values of $d_2$ (from $2/16\lambda_0$ to $6/16\lambda_0$), as displayed in Figure 4.23. It can be observed that, using $d_2 = 0.21\lambda_0$, the gain of this configuration is similar to the gain of the

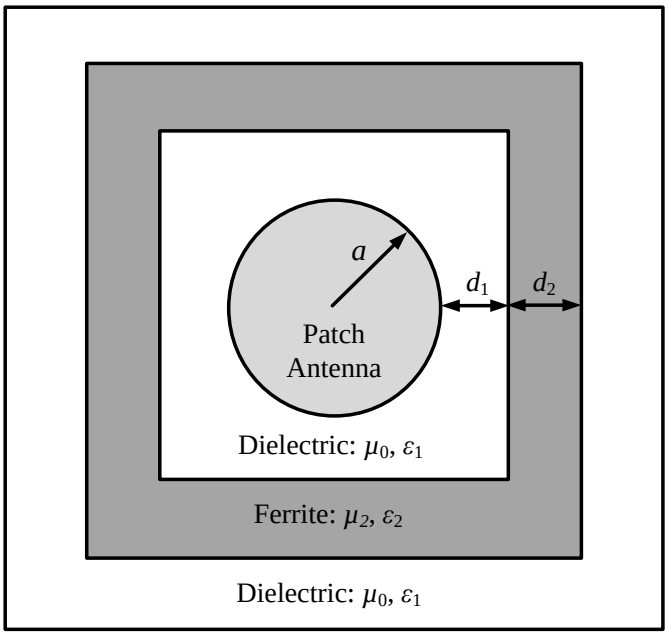


Figure 4.22: Proposed substrate structure for a circular patch and square ring.

circular patch/circular ring case (around 10 dB). However, the distance $d_2$ is smaller for the square ring than for the circular ring ($d_2 = 0.21\lambda_0$ for the square ring versus $d_2 = 0.25\lambda_0$ for the circular ring). This result is expected since the area of the square ring is larger than the area of the circular ring with the same dimension $d_2$. Therefore, to obtain similar performance, the distance $d_2$ of the square ring should be smaller than its equivalent for the circular ring.

For instance, the areas of these two configurations, using a frequency of 5.8 GHz, are summarized in Table 1. As illustrated, the area of the ferrite ring for both cases is almost identical, which results in a similar gain. This comparison suggests that, as long as the ferrite area is identical, the same gain can be achieved with a circular or a square ring. This behavior is similar to that of the scan angle of cavity-backed antennas [69].

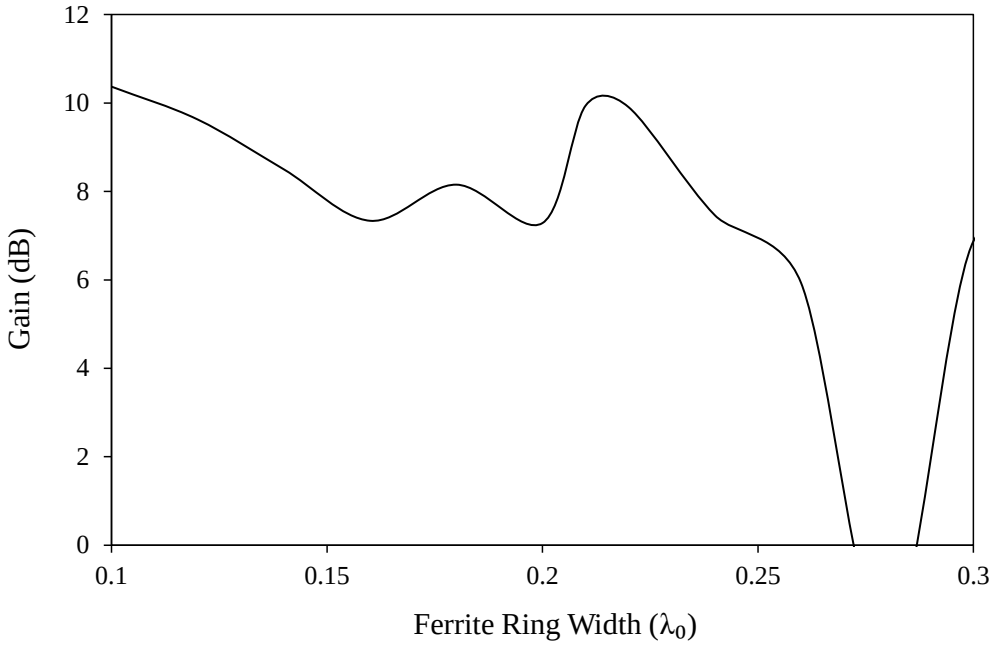


Figure 4.23: Gain for the circular patch and a square ring hybrid substrate.

Table 4.4: Area of circular patch-circular ring and circular patch-square ring hybrid substrates at 5.8 GHz.

| | Circular Ring ($d_2 = 0.25\lambda_0$) | Square Ring ($d_2 = 0.21\lambda_0$) |
|---|---|---|
| Area of dielectric ($cm^2$) | 5.2531 | 6.6884 |
| Area of ferrite + dielectric ($cm^2$) | 21.0124 | 22.6445 |
| Area of ferrite ring ($cm^2$) | 15.7593 | 15.9560 |

Square Patch with Circular Ring

In the second combination, the circular patch was replaced by a square patch. The length of the patch was selected to be 10.2 mm to obtain the same resonant frequency ($f$= 5.8 GHz). A circular ring was incorporated in this hybrid design (see Figure 4.24). Again, to simplify the process, the distance $d_1$ was fixed to $\lambda_0/4$, and the gain toward broadside was calculated for different values of $d_2$.

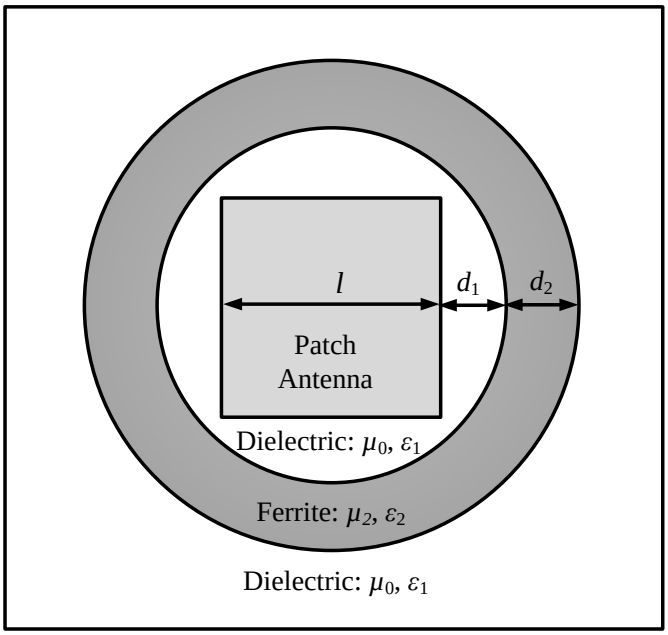


Figure 4.24: Proposed substrate structure for a square patch and a circular ring.

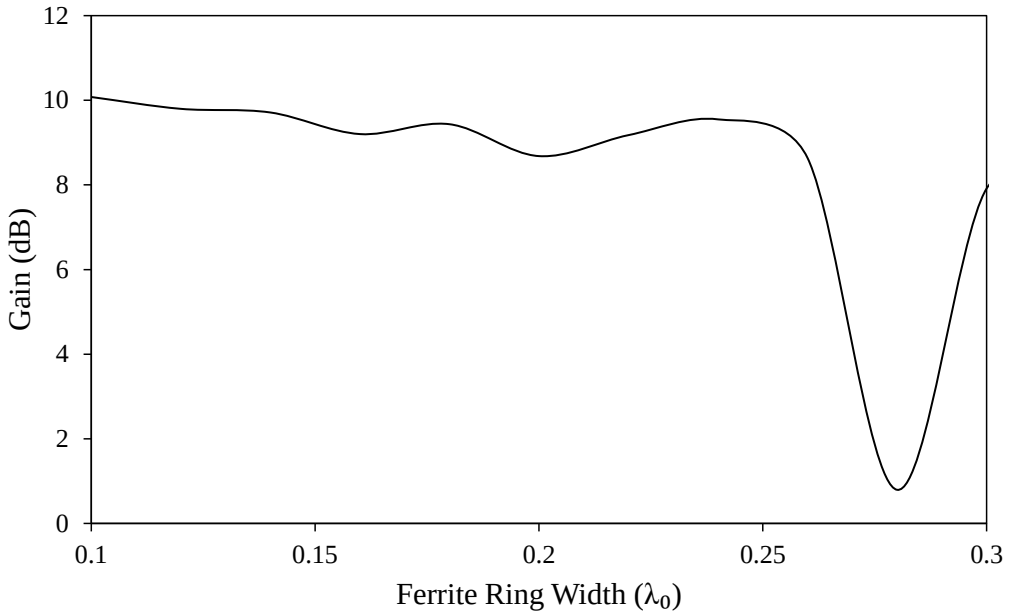


Figure 4.25: Gain for the square patch and circular ring hybrid substrate.

This examination indicates that the optimal value of $d_2$ is $0.24\lambda_0$, for which the gain is around 9.5 dB. When this configuration is compared with the circular patch-circular ring case, it is observed that there is not a significant difference in the value of $d_2$. This suggests that the shape of the patch does not play an important role in the maximum gain of the hybrid substrate.

Square Patch with Square Ring

Finally, a square patch/square ring combination (as displayed in Figure 4.26) was analyzed. The size of the patch antenna is the same as in the previous case ($l = 10.2$ mm), and $d_1$ was fixed to $\lambda_0/4$. For this configuration, the gain as a function of the value $d_2$ is as illustrated in Figure 4.27. In this case, the maximum gain is obtained for a distance $d_2$ around $0.22\lambda_0$ which is a similar value to that obtained with the circular patch/square ring. This reinforces the conclusion that the shape of the patch does not play a significant role in the enhancement of the gain. Furthermore, the most significant property of the hybrid substrate seems to be the area of the ferrite ring, regardless of its shape.

*Anisotropic Ferrite*

In the previous results, we assumed an isotropic ferrite. This means that the permeability has the same values in all directions $x$, $y$, and $z$, or

$$\mu_2 = \mu_{r2}\mu_0 \tag{4.3}$$

where $\mu_0$ is the permeability of free-space and $\mu_{r2}$ is the relative permeability of the material (for the previous cases, $\mu_{r2} = 14$).

To simulate more practical designs, we selected different values for the permeability in the $x$, $y$, and $z$ directions, or

$$\mu_2 = \mu_0 \begin{bmatrix} \mu_x & 0 & 0 \\ 0 & \mu_y & 0 \\ 0 & 0 & \mu_z \end{bmatrix} \tag{4.4}$$

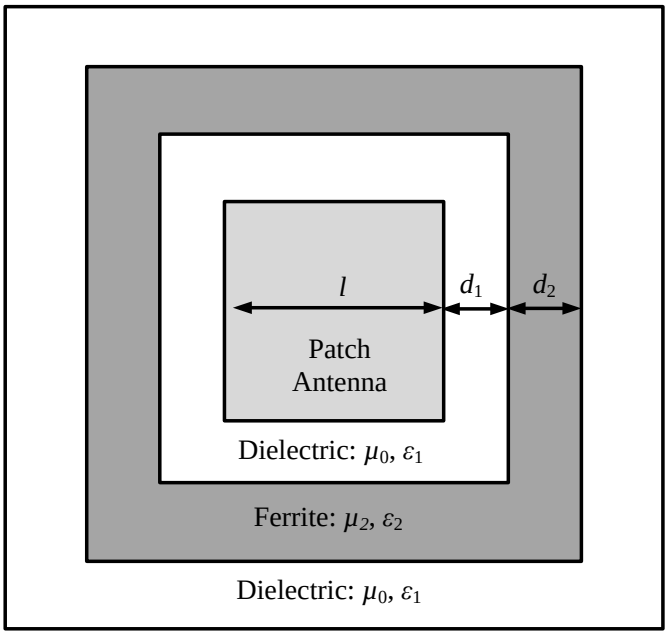


Figure 4.26: Proposed substrate structure for a square patch and a square ring.

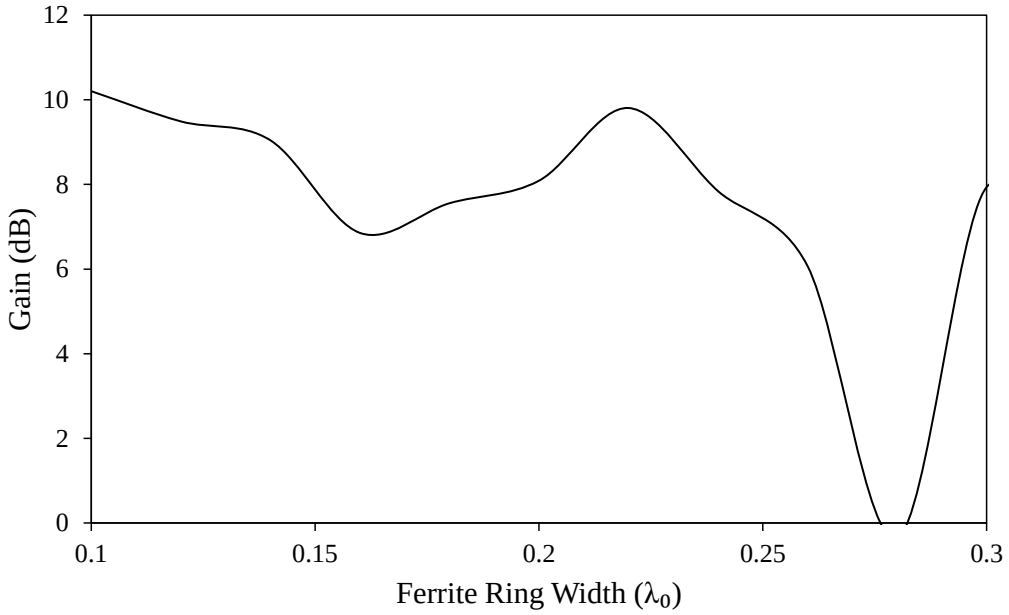


Figure 4.27: Gain for the square patch and square ring hybrid substrate.

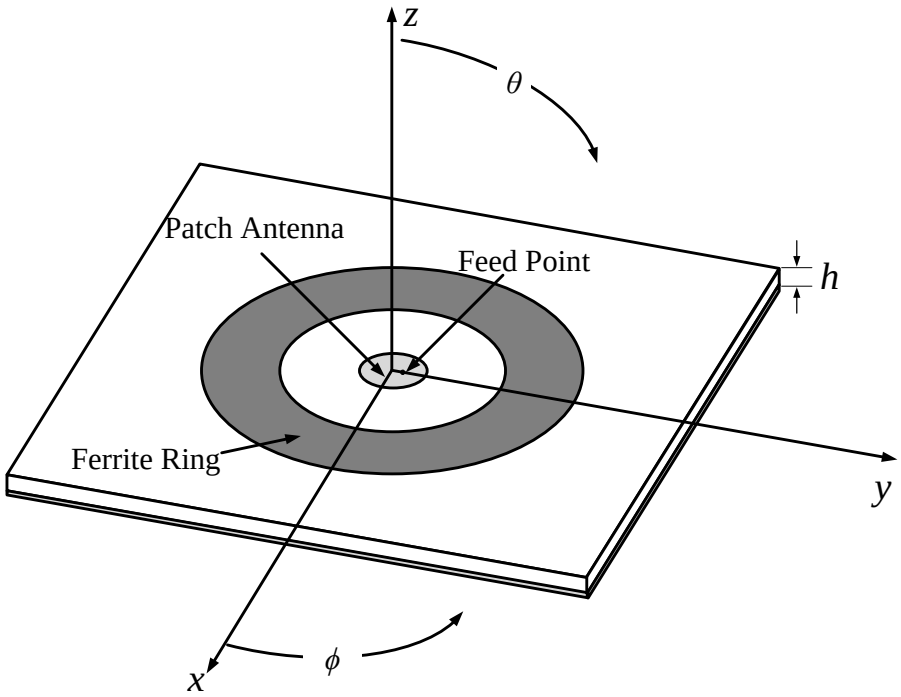

Figure 4.28: Coordinate system to determine the anisotropic permeability tensor.

where $\mu_0$ is the permeability of free space, $\mu_x$ is the relative permeability of the material in the $x$ direction, $\mu_y$ is the relative permeability in the $y$ direction, and $\mu_z$ is the relative permeability in the $z$ direction. The coordinate system is shown in Figure 4.28. It is important to mention that the feed point is along the $y$ axis; this means that the E-plane is the $y$-$z$ plane and the H-plane is the $x$-$z$ plane.

The first step was to select three different values for $\mu_x$, $\mu_y$, and $\mu_z$. To compare the results with the previous results, the chosen values were 14, 7, and 1. Each one of these values was interchanged as the permeability of the $x$, $y$, and $z$ directions, which results in eight permeability tensors.

Using HFSS [78], these tensors were used to analyze the impact of an anisotropic material in the circular patch/circular ring hybrid substrate with $d_1 = d_2 = \lambda_0/4$. The results can be divided into three groups, depending on the component with the highest permeability

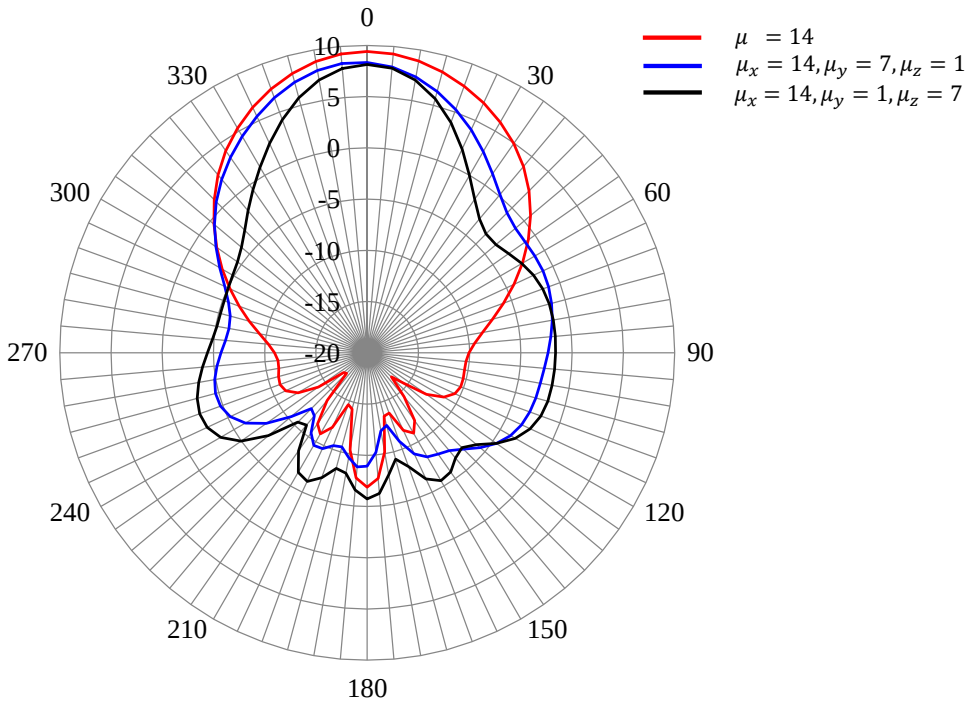


Figure 4.29: E-Plane radiation pattern using a $\mu_x$ larger than $\mu_y$ and $\mu_z$.

value: i.e., (1) $\mu_x = 14$, (2) $\mu_y = 14$, and (3) $\mu_z = 14$. The objective is to compare which one of the directions ($x$, $y$, or $z$) impact more the gain of the antenna.

In the first group, when the relative permeability in the $x$ direction is 14, two combinations are possible: (a) $\mu_y = 7$ and $\mu_z = 1$ or (b) $\mu_y = 1$ and $\mu_z = 7$. The E-plane gain ($y-z$ plane or $\phi = 90^\circ$) of these two cases is displayed in Figure 4.29. For comparison, the gain of the isotropic case is also illustrated. This figure shows a significant difference in the pattern shape between the isotropic and anisotropic cases. However, in terms of the broadside gain ($\theta = 0^\circ$), it is observed that the gain of the two anisotropic cases is similar to the gain of the isotropic case.

The second group is given by a relative permeability of 14 in the $y$ direction and two different combinations: (a) $\mu_x = 7$ and $\mu_z = 1$ or (b) $\mu_x = 1$ and $\mu_z = 7$. When this group is analyzed, the results are those shown in Figure 4.30. The two anisotropic cases exhibit

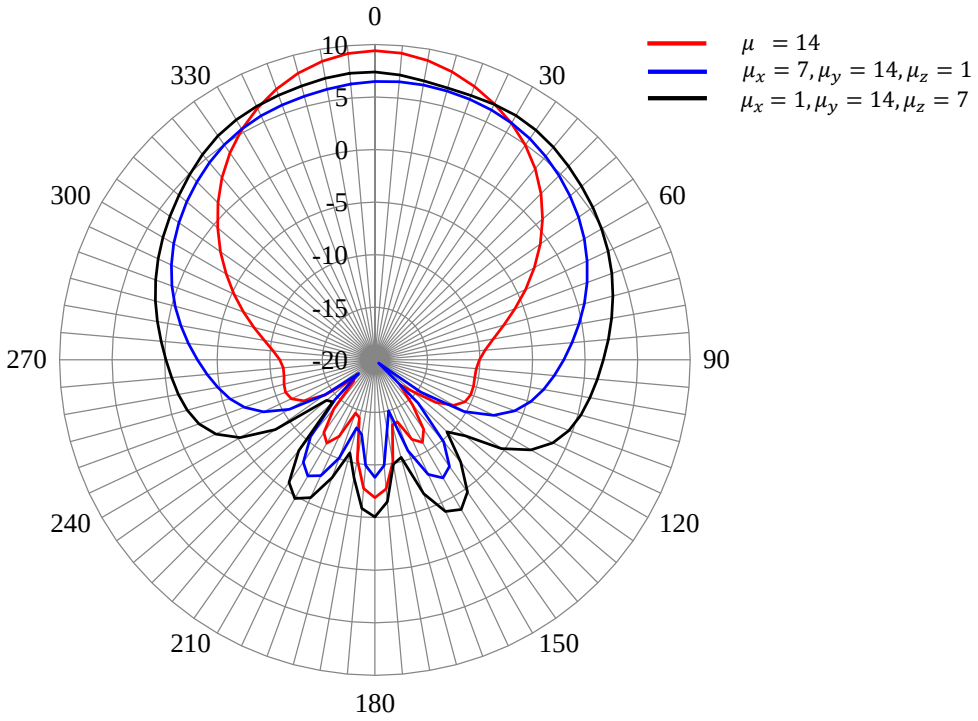


Figure 4.30: E-Plane radiation pattern using a $\mu_y$ larger than $\mu_x$ and $\mu_z$.

a broader pattern than the isotropic case. Furthermore, in this case, there is a significant reduction in the maximum gain (around 2 or 3 dB less than the isotropic material).

The last group is composed by $\mu_z = 14$ and (a) $\mu_x = 7$ and $\mu_y = 1$ or (b) $\mu_x = 1$ and $\mu_y = 7$. The results from this group are displayed in Figure 4.31. These cases show the worst scenario: less than 1 dB of gain enhancement compared to the conventional case (i.e., no ring). A reduction of 3 to 4 dB in the maximum gain is obtained by using these permeability tensors, in contrast to the isotropic case.

After the analysis of the three groups, it can be noted that, in terms of the maximum gain, the most significant component is the $x$ component value, or the component in the H-plane. In addition, the patterns and the maximum gain are similar for the two anisotropic cases in each group; thus, there is not a significant difference by interchanging the two low values in each group.

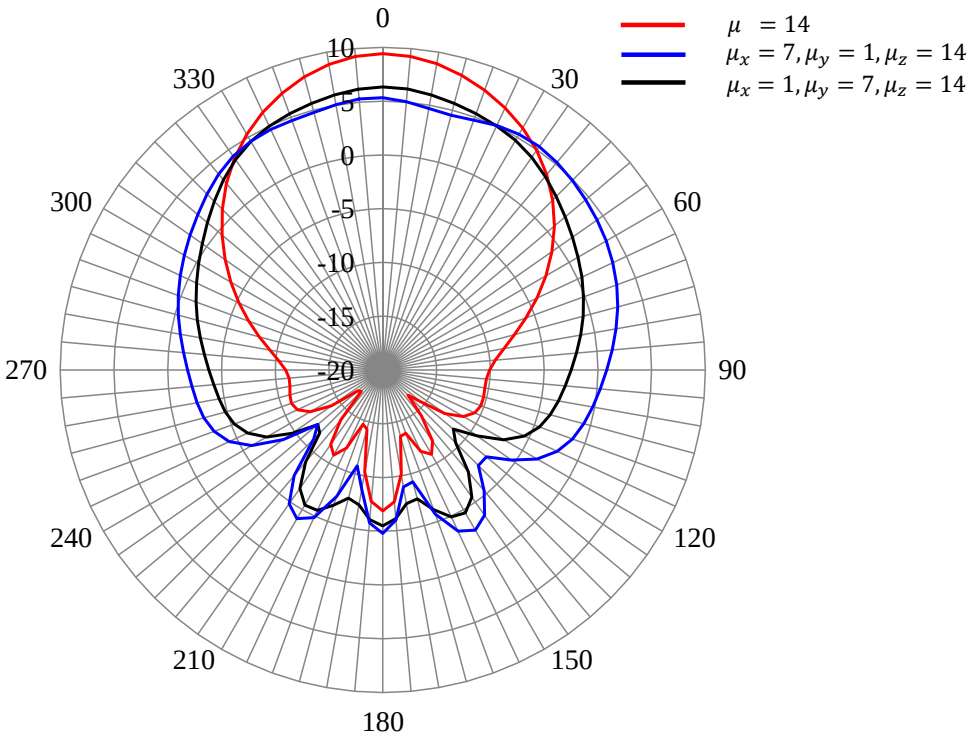


Figure 4.31: E-Plane radiation pattern using a $\mu_z$ larger than $\mu_x$ and $\mu_y$.

To obtain a better concept of the performance of these permeability tensors, the 3-D patterns for group 1 and 2 are shown in Figures 4.32 and 4.33, respectively. It is interesting to observe that the maximum gain is obtained in the direction of the largest permeability component. For instance, in the first group, the largest component of the permeability tensor is in the $x$ direction, and the largest gain is aligned with the $x$ axis. Similar results can be noted in the second group, where the largest gain is in the $y$ axis.

## 4.2 MICROSTRIP ELEMENT ARRAYS

Microstrip patch antennas are commonly used in array configurations to achieve high gain, as shown in Figure 4.34. Their simple configuration makes them an excellent alternative to be integrated with microwave circuits or to conform to different platforms. However, when the main beam is scanned, the surface waves can cause a detrimental impact in the absolute gain. The reason is a change in the input impedance and, as consequence, an increase in the reflection coefficient, $\Gamma$, of each antenna element.

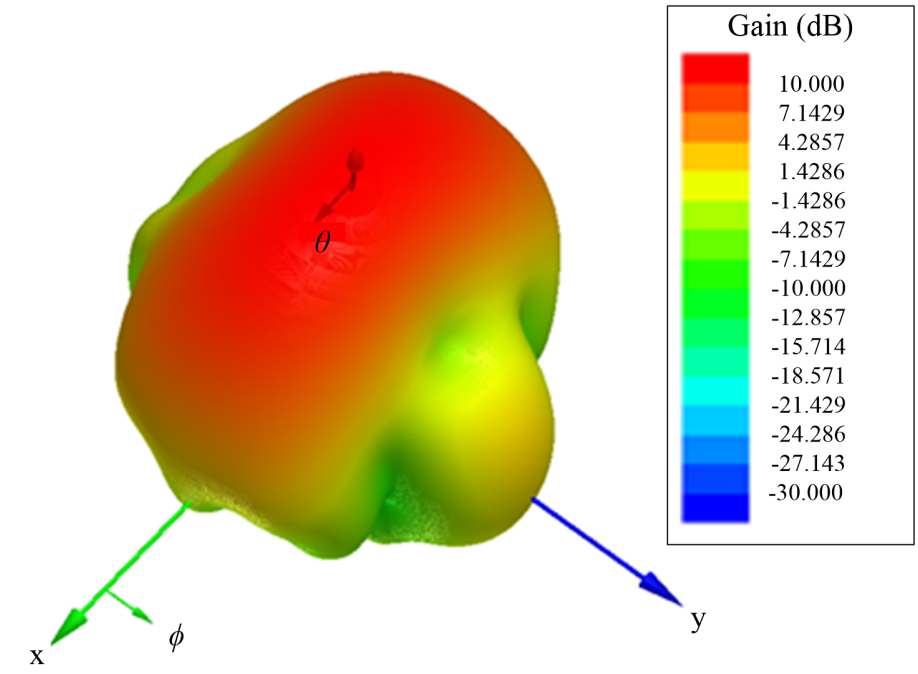


(a)

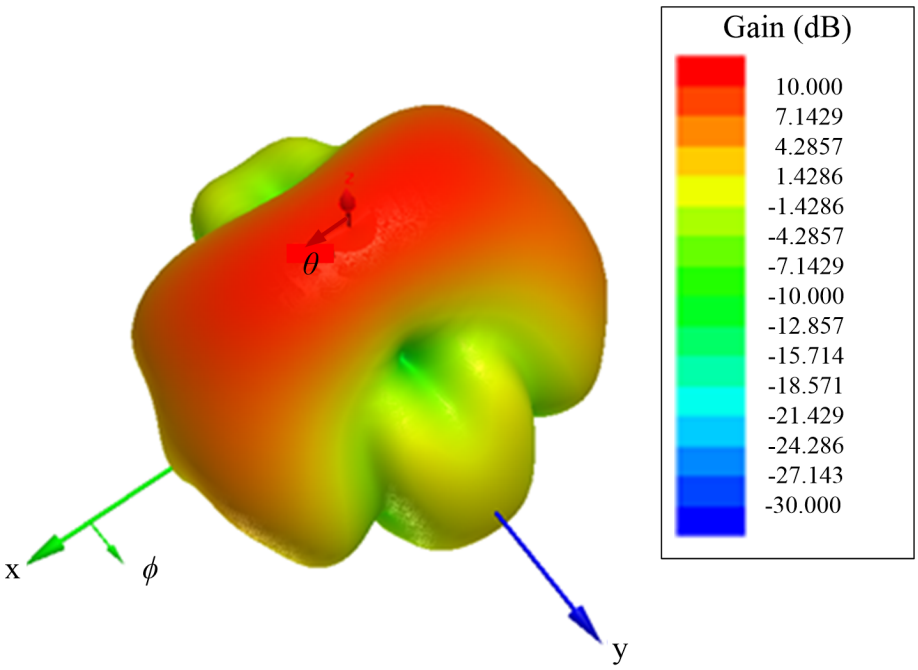


(b)

Figure 4.32: Relative permeability in the $x$ direction is $\mu_x = 14$ and (a) $\mu_y = 7$, $\mu_z = 1$, and (b) $\mu_y = 1$, $\mu_z = 7$.

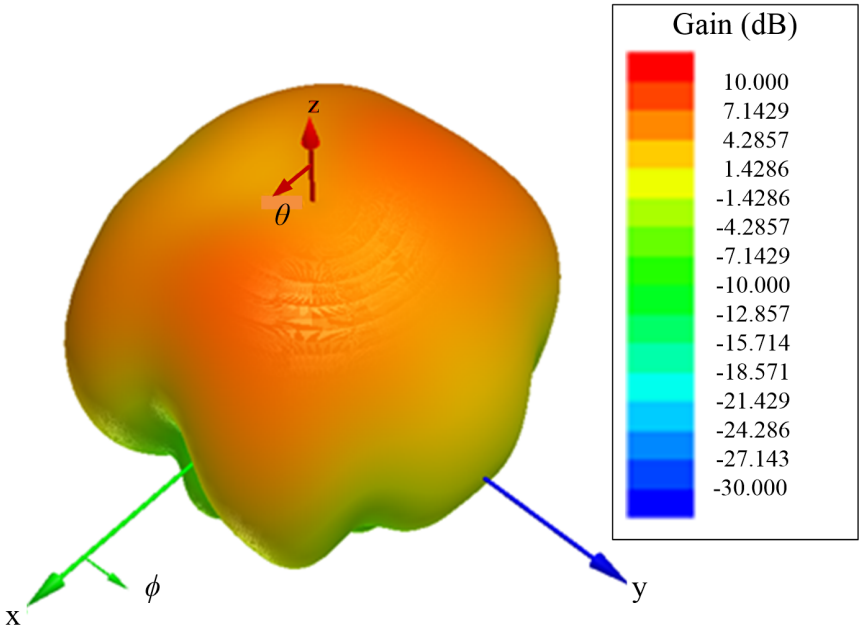


(a)

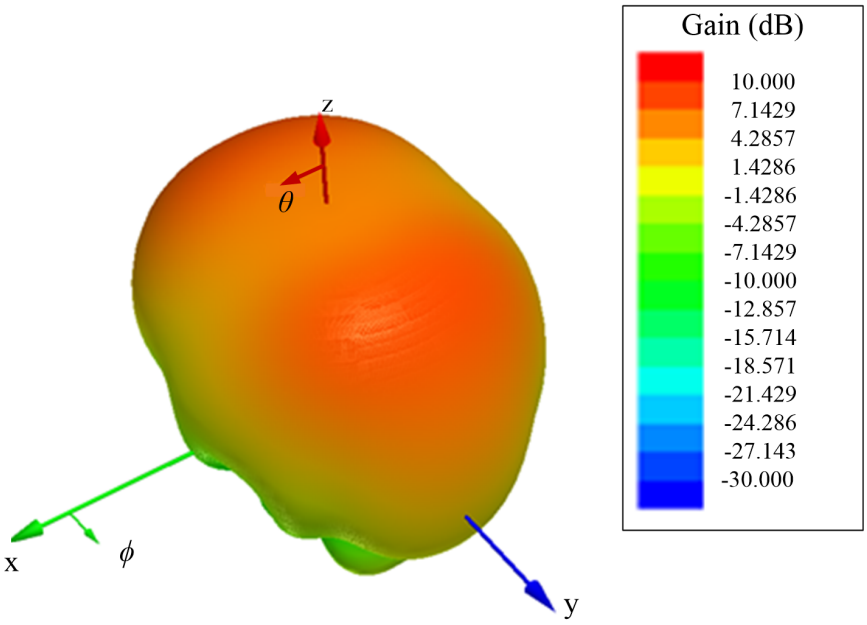


(b)

Figure 4.33: Relative permeability in the $y$ direction is $\mu_y = 14$, and (a) $\mu_x = 7$, $\mu_z = 1$, and (b)$\mu_x = 1$, $\mu_z = 7$.

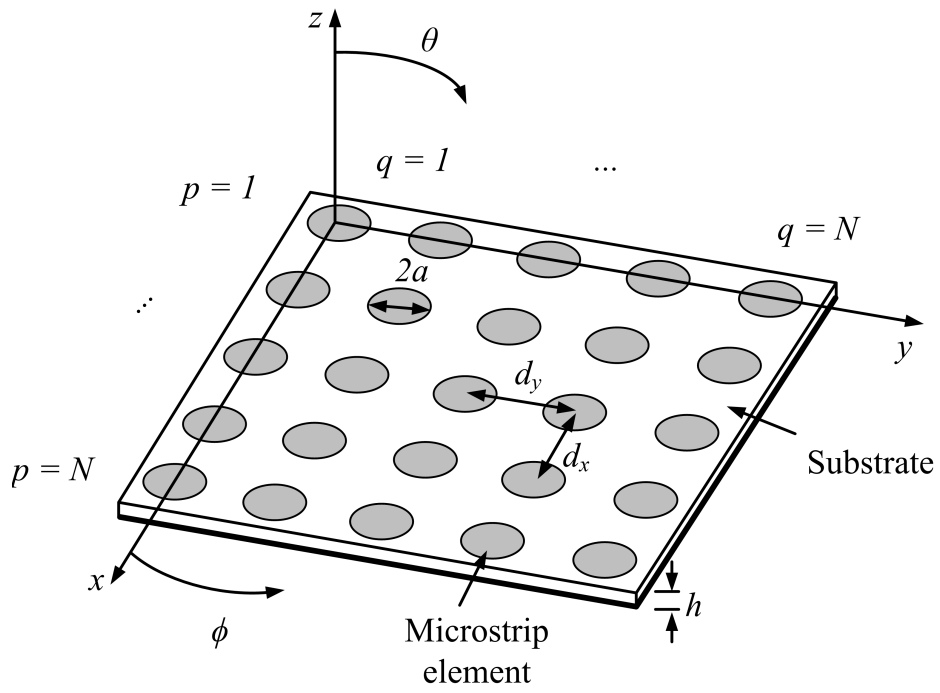


Figure 4.34: Microstrip patch array configuration.

The reflection coefficient can achieve a magnitude of unity, as the array is scanned from broadside to endfire [68], [69]. This condition is known as scan blindness [3], and it is an undesirable behavior in phased arrays since no electromagnetic wave can be received/transmitted in that direction. Scanning at other angles (especially those near the blind direction) can also exhibit high reflections, resulting in a low absolute gain. Commonly, $\Gamma = 1/3$ (VSWR of 2:1) is selected to define the scan range of the array; any magnitude above 1/3 will introduce significant mismatches.

It has been shown that, as the thickness of the substrate increases, the scan range decreases since more surface waves propagate in the dielectric. This behavior has been widely studied for infinite arrays for dipoles and microstrip patch elements [68], [69]. The analysis has been based on a unit cell approximation, whose difficulty to solve is similar to the single element. However, less attention has been paid to finite arrays due to the difficulty and time consumption of their analysis, which must take into account the edge of

the substrate [79], [80]. For those cases, it has been demonstrated that the array has to be larger than a 7 x 7 element array to exhibit behavior similar to that of an infinite array. In any case, the scan range of microstrip patch element arrays is highly limited by the surface wave propagation.

A popular technique to increase the scan range is called cavity-backed antennas. The method consists of placing metallic walls around the microstrip element to suppress the propagation of the surface waves in the dielectric [69]. Therefore, the magnitude of the reflection coefficient, compared to the conventional substrate, can be reduced, and scan blindness can be eliminated. However, high reflections are still noticeable for angles near endfire.

The analysis of a finite array can be very difficult since each patch will be impacted differently, depending on its relative position inside the array. Moreover, as the main beam is scanned, the surface waves impact each of the patches differently. Several assumptions can simplify the analysis of arrays: an infinite array (no edges), and all elements are equally spaced.

Based on the previous assumptions, the analysis of a conventional array can start with the calculation of the probe excitation current at each antenna element:

$$I_i^p(\theta,\phi) = e^{-j[d_x(p-1)u+d_y(q-1)v]} \tag{4.5}$$

$$u = \sin(\theta)\cos(\phi)$$
$$v = \sin(\theta)\sin(\phi)$$

where $d_x$ and $d_y$ are the $x$ and $y$ distances between the patches and $p$ and $q$ are the column and row of the patch in the array, respectively.

The voltage at each patch can be found by using [81]

$$V = I_i^p \frac{j\eta_0 k_0 z'}{\varepsilon_r} \sqrt{\frac{2}{\pi(x_{11}'^2 - 1)}} \int_0^\infty \left[\xi_1(\beta) - \frac{j(\varepsilon_r - 1)\xi_2(\beta)}{\beta^2}\right] \frac{x_{11}'^2}{k_0 a} \left[\frac{B_1'(k_0 a\beta)}{(x_{11}'/k_0 a)^2 - \beta^2}\right] B_0(k_0\rho_0\beta) B_0\left(\frac{k_0 d_0 \beta}{2}\right) \beta^2 d\beta \tag{4.6}$$

When all the elements in the array are excited, the current at each patch will be a superposition of the currents of all elements:

$$I_i = \sum_{p=1}^{N^2} I_i^p \tag{4.7}$$

Using these relations, the active input impedance is easily found by [79]

$$Z_i n(\theta, \phi) = \frac{V_i^i {I_i}^2}{I_i^p} + jX_L \tag{4.8}$$

where $X_L$ is the reactance of the feed.

If a broadside-matched array is assumed, the reflection coefficient in the scan direction $(\theta, \phi)$ can be calculated by

$$\Gamma(\theta, \phi) = \frac{Z_{in}(\theta, \phi) - Z_{in}(0,0)}{Z_{in}(\theta, \phi) + Z_{in}^*(0,0)} \tag{4.9}$$

where $*$ indicates the complex conjugates. To obtain a higher value of the absolute gain $G_{abs}(\theta, \phi)$, the reflection coefficient $\Gamma(\theta, \phi)$ needs to be reduced, according to [3]:

$$G_{abs}(\theta, \phi) = G(\theta, \phi)[1 - |\Gamma(\theta, \phi)|^2] \tag{4.10}$$

where $G(\theta, \phi)$ is the gain of the antenna without taking into account mismatches [not to be mistaken for the absolute gain, which actually takes into account reflections, as can be seen from (4.10)].

As mentioned previously, for infinite arrays using conventional substrates, the reflection coefficient toward some angles can achieve a magnitude of unity, resulting in

$G_{abs} = 0$. Therefore, the antenna is blind toward that direction. If the substrate is modified, the currents and the voltages of the previous equations are modified. This means that, by properly changing the characteristics of the substrate, the reflection coefficient can be significantly reduced. Hybrid substrates are options to change the properties of the substrate and reduce the reflection coefficient in phased arrays. In the next section, we will show how the reflection coefficient can be modified by using the cavity-backed and hybrid configurations.

### *Results*

The results are presented in two parts. The first part is devoted to the analysis of arrays based on the assumption that the array is infinite. This analysis is performed by modeling a unit cell and neglecting the impact of the edges of the substrates. For the second part of the results, a more practical analysis is performed by simulating a finite array and including the impact of the edges of the substrates.

#### Infinite Array

To demonstrate the use of hybrid substrates to eliminate scan blindness, an example from [69] is borrowed to analyze the performance of the proposed substrate and compare it to the conventional and cavity-backed configurations. In the example, the conventional configuration consists of a microstrip circular antenna with a radius $a = 0.164\lambda_0$ above a dielectric with a relative permittivity of 2.5, as shown in Figure 4.35(a). The same dielectric and antenna element is used for the cavity-backed and the hybrid substrates. The remaining dimensions for the cavity-backed and the hybrid substrates are displayed in Figure 4.35(b) and Figure 4.35(c), respectively.

The three configurations were simulated in HFSS [78] using a unit cell with master and slave boundary conditions and a floquet port (as shown in Figure 4.36) to obtain the performance of an infinite array. The size of the unit cell for the three configurations was

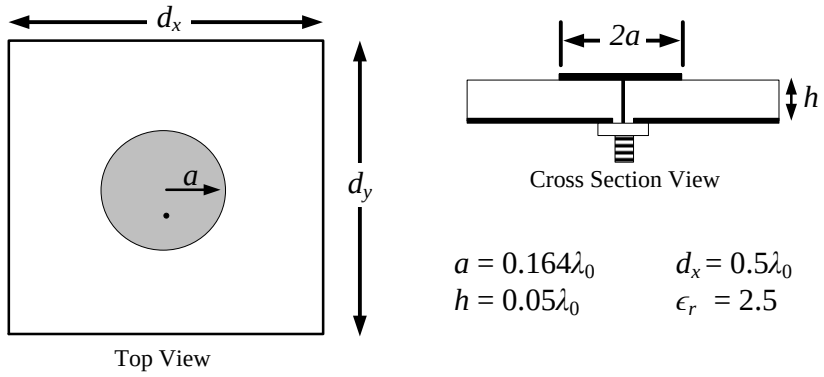


$a = 0.164\lambda_0$ $\quad d_x = 0.5\lambda_0$
$h = 0.05\lambda_0$ $\quad \epsilon_r = 2.5$

(a)

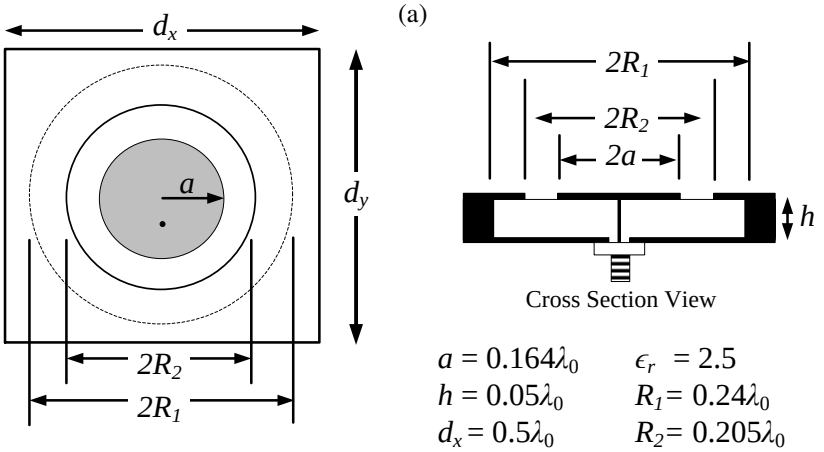


$a = 0.164\lambda_0$ $\quad \epsilon_r = 2.5$
$h = 0.05\lambda_0$ $\quad R_1 = 0.24\lambda_0$
$d_x = 0.5\lambda_0$ $\quad R_2 = 0.205\lambda_0$

(b)

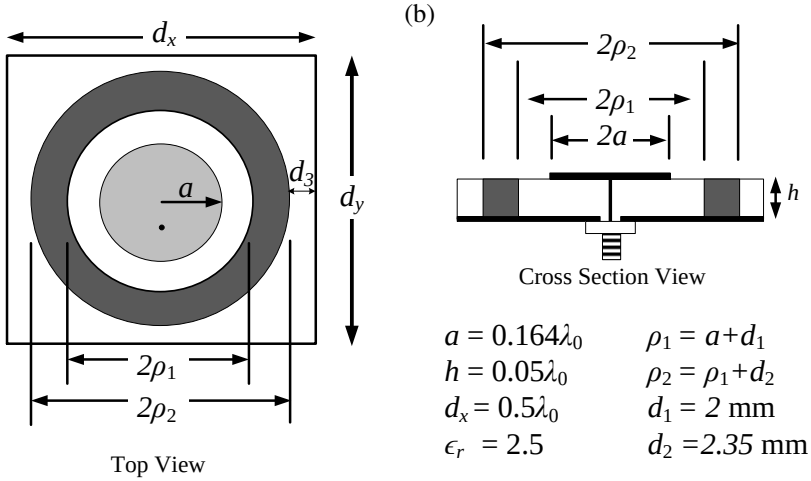


$a = 0.164\lambda_0$ $\quad \rho_1 = a + d_1$
$h = 0.05\lambda_0$ $\quad \rho_2 = \rho_1 + d_2$
$d_x = 0.5\lambda_0$ $\quad d_1 = 2$ mm
$\epsilon_r = 2.5$ $\quad d_2 = 2.35$ mm

(c)

Figure 4.35: Unit cell of different microstrip patch configurations used to calculate the scan angle of infinite arrays. (a) Conventional substrate. (b) Cavity-backed antenna. (c) Hybrid substrate.

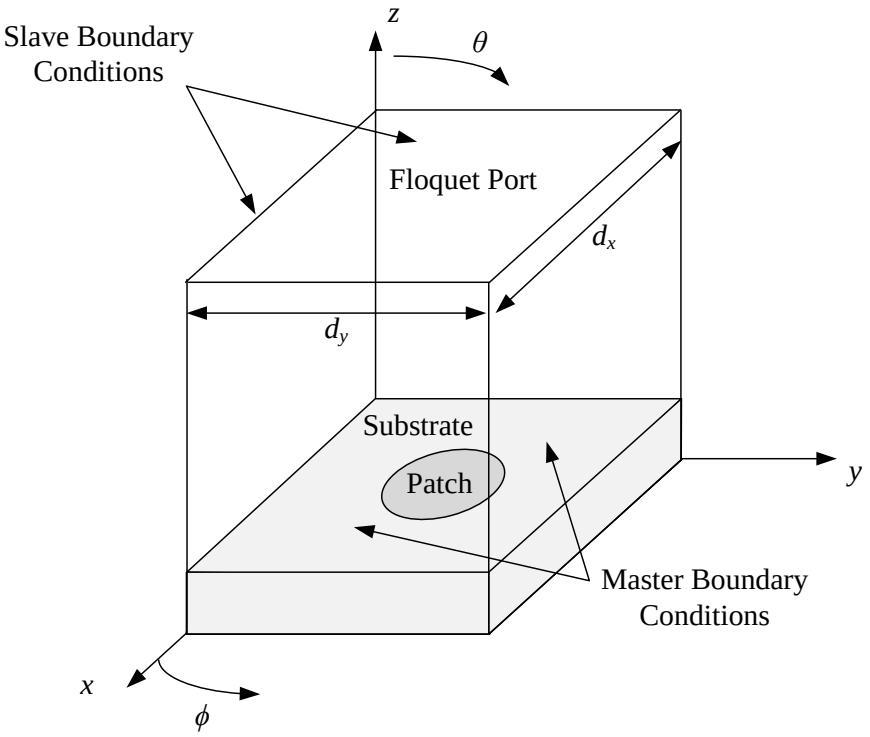


Figure 4.36: Unit cell configuration used to simulate the performance of infinite arrays with conventional, cavity-backed, and hybrid substrates.

fixed at $d_x = d_y = 0.5\lambda_0$. For the hybrid substrate, the dimensions $d_1$ and $d_2$ were optimized to obtain the lowest reflection coefficient using a distance of $d_3 = 0.1$ mm.

The simulations demonstrate that the hybrid configuration can significantly reduce the reflection coefficient compared to the conventional and cavity-backed configurations. As can be seen from Figure 4.37, the usable scan range for the conventional substrate is only 55 degrees (using a VSWR 2:1), and scan blindness is almost observed at 80 degrees. The cavity-backed antenna technique increases the scan range to 65 degrees, and the reflection coefficient at 80 degrees is significantly reduced. However, at 90 degrees, the magnitude is still very high (0.72), reducing the absolute gain to only 48% of the gain. The results for the hybrid substrate demonstrate a completely different performance: the scan range increases to 90 degrees (i.e., the magnitude of the reflection coefficient is lower than 0.33

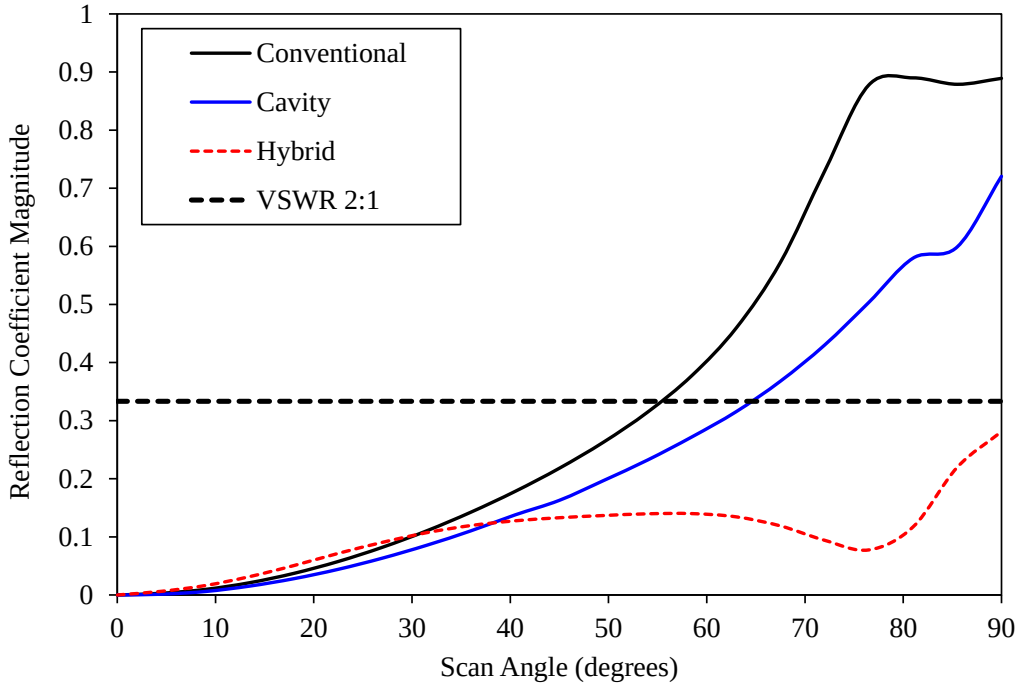


Figure 4.37: E-Plane reflection coefficients versus the scan angle of infinite arrays of circular microstrip patches.

for scan angles up to 90 degrees). This means that more than the 89% of the gain is still available at any angle from broadside to endfire.

In [82], it was demonstrated that the distances $d_1$ and $d_2$ have to be around a quarter-wavelength to enhance the gain of the antenna. However, if these values are utilized in an array configuration, the array will be extremely large, and side lobes can appear in the radiation pattern of the element. Therefore, to avoid this, the unit cell size was fixed at $0.5\lambda_0$. In this case and based on the results from [82], we cannot expect to enhance the gain of the hybrid array compared to the conventional or cavity-backed. A tradeoff has to be made between the gain and reflection coefficient, since both impact the absolute gain.

To analyze the impact on the gain of the three configurations, the array setup tool from HFSS and the unit cell model were used to simulate a 9 x 9 element array. As expected, the gain of the hybrid substrate is reduced compared to the conventional and cavity-

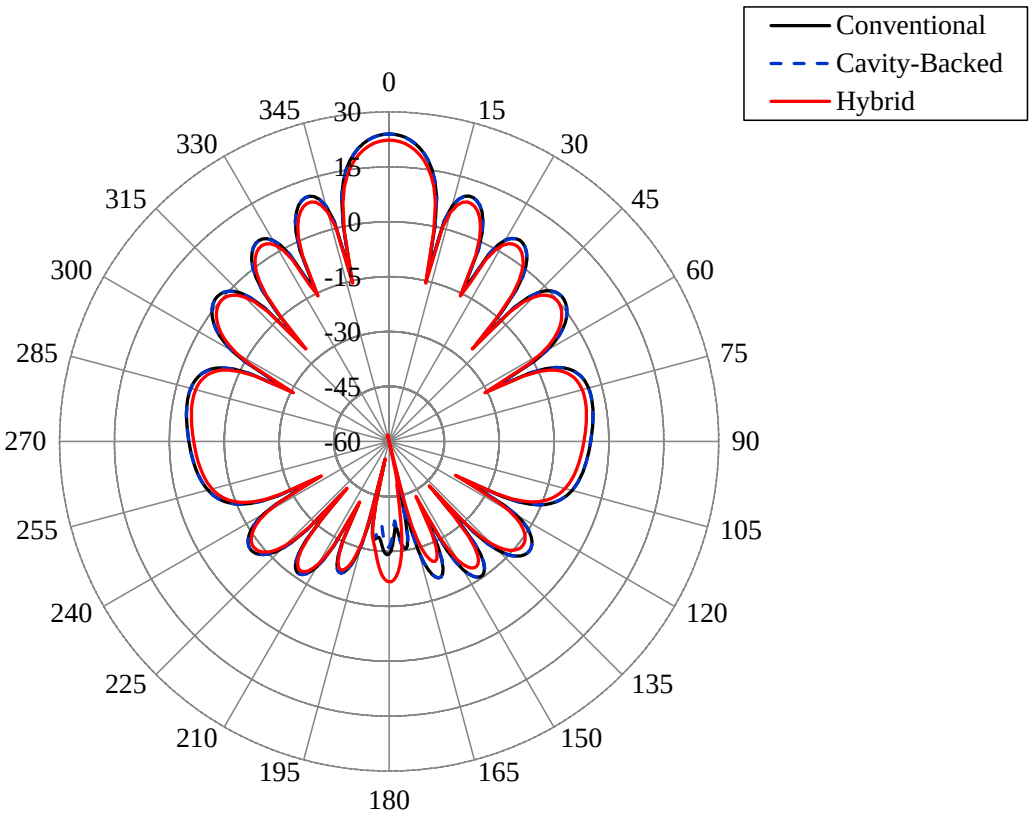


Figure 4.38: E-plane gain pattern (in dB) for conventional, cavity-backed, and hybrid substrates.

backed, as shown in Figure 4.38. However, the reduction is less than 2 dB (24.00 dB vs. 22.33 dB), which is a good tradeoff when a significant reduction in the reflection coefficient is achieved.

### Finite Arrays

To analyze the impact of the finite size in arrays, 9 x 9 microstrip element arrays were simulated in HFSS using the three techniques: conventional, cavity-backed, and hybrid substrates. The first step was to calculate the broadside-matched reflection coefficient of the center element of the array. The results for this analysis are shown in Figure 4.39. It can be observed that the magnitude of the reflection coefficient for the hybrid substrate is equal to or less than 1/3 for scan angles from 0 to 90 degrees, which results in a scan range

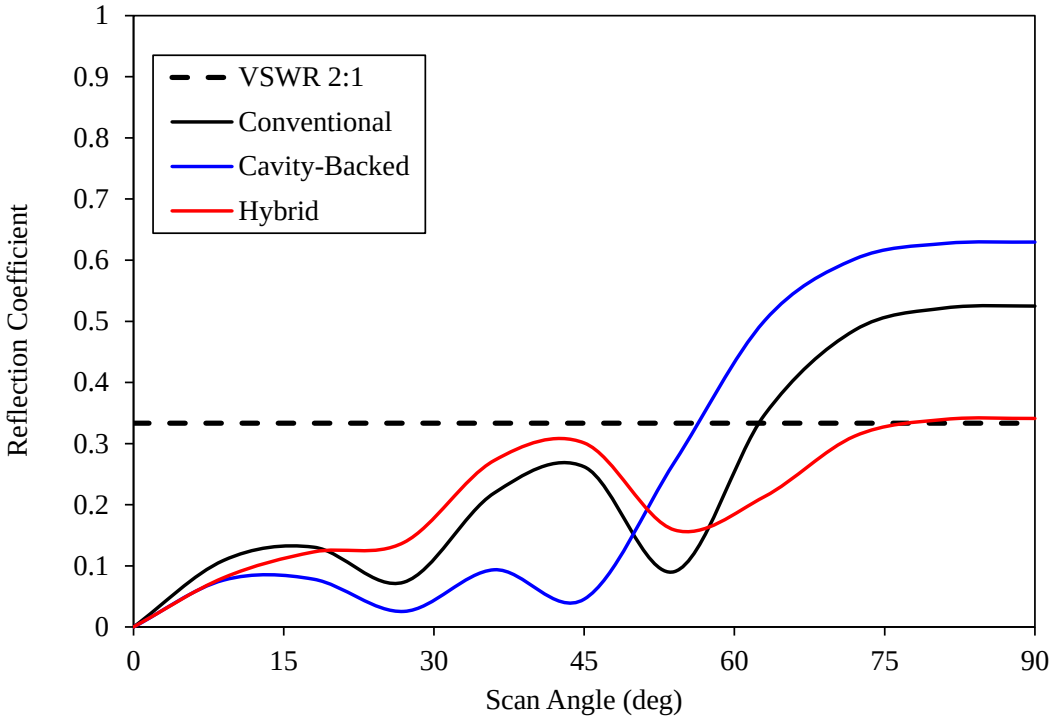


Figure 4.39: Reflection coefficient for the center element of a 9 x 9 microstrip element array.

of 90 degrees. On the other hand, the scan range for the conventional is only 62 degrees, and for the cavity-backed, it is 58 degrees. These results validate our previous statement that hybrid substrates are an excellent alternative to increase the scan range.

In addition to the reflection coefficient, an analysis of the gain of the antenna was performed. To do this, the main beam was scanned from 0 to 90 degrees, and the gain versus the scan angle was obtained. The results are shown in Figure 4.40. It is important to observe that the gain of the hybrid substrate is lower than those of the cavity-backed and conventional configurations. This is due to the losses in the ferrite, and it is more evident as the main beam is scanned near endfire, where the gain of the hybrid configuration decreases faster than for the other designs.

The absolute gain was also calculated using the broadside-matched reflection coefficient, as shown in Figure 4.41. In this case, we can see that the absolute gain of the

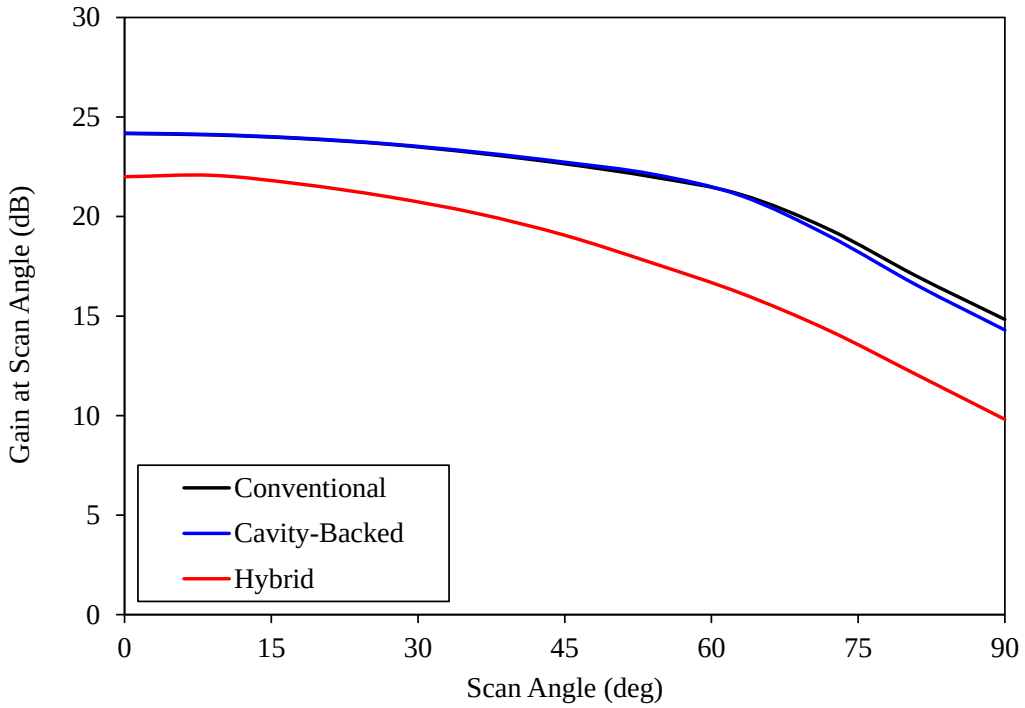


Figure 4.40: Gain at the scan angle of a 9 x 9 microstrip element array using conventional, cavity-backed, and hybrid substrates.

hybrid configuration is not as high as those of the other two designs due to the losses in the substrate.

## 4.3 SUMMARY

This chapter describes a new hybrid substrate structure based on the addition of a ferrite ring to a conventional dielectric that enhances the gain performance of a circular microstrip patch. An enhancement of about 4 dB in the gain and nearly 1% in the impedance bandwidth were obtained.

The analysis of the fields in the substrate shows that constructive interference is created in the ferrite ring. The maximum gain is obtained when both distances $d_1$ and $d_2$ are nearly one-quarter of the free-space wavelength.

Simulations of the reflection coefficient for infinite arrays demonstrated that the hybrid substrate is also a great alternative to increase the scan range in microstrip arrays.

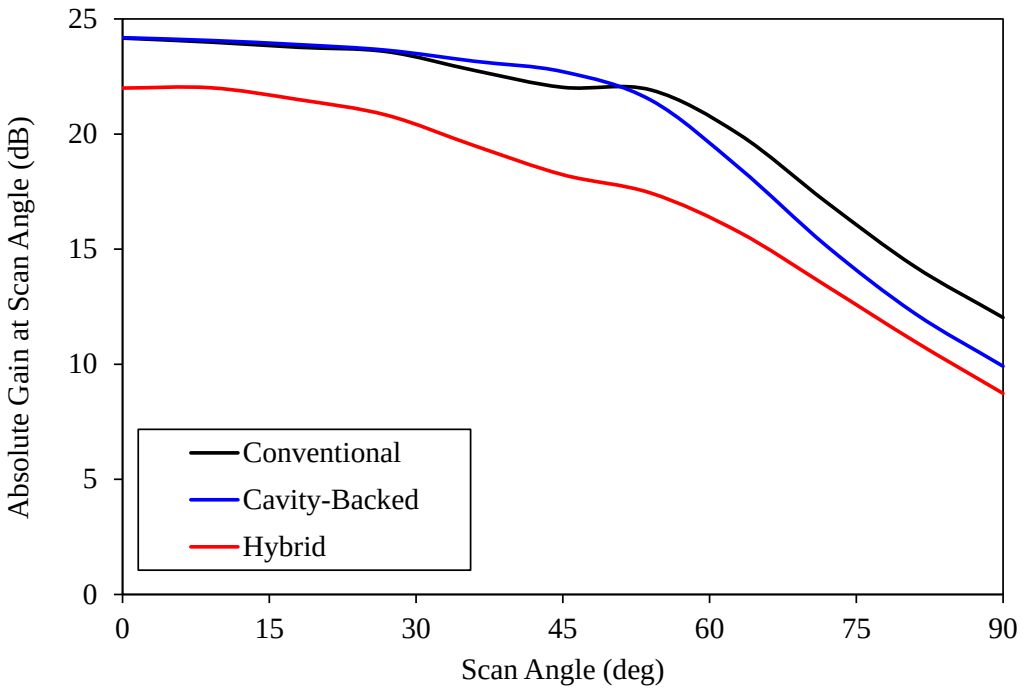


Figure 4.41: Absolute gain at the scan angle of a 9 x 9 microstrip element array using conventional, cavity-backed, and hybrid substrates.

For a substrate with a height of $0.05\lambda_0$, the scan range increases from 55 degrees (in a conventional array) to 90 degrees for the hybrid configuration.

The analysis of finite arrays shows that a tradeoff has to be made between the gain and the reflection coefficient when using different substrates. The hybrid substrate exhibits excellent performance, reducing the reflections as the main beam is scanned, but due to the losses in the ferrite ring, the gain is also reduced.

# Chapter 5

# CONCLUSIONS AND RECOMMENDATIONS

This chapter summarizes, concludes and suggests some future work based on the topics discussed in the previous chapters.

## 5.1 Conclusions

A space-time adaptive processing configuration to improve the system performance in GPS applications has been described. The system consists of a spherical array, the use of the MVDR algorithm, and the implementation of fixed non-uniform spaced time delays. Although a spherical array was designed to increase the LOS coverage and the MVDR algorithm was used to null the high-power interferers, the focus of this dissertation can be summarized in three steps: analyze and improve the adaptive algorithm, implement non-uniformly spaced time delays, and improve the performance of the antenna array.

A modified PU-LMS algorithm optimized for a seven-element GPS spherical antenna array was integrated. This algorithm updates the weight of the top element of our antenna array and one more weight at each iteration. A critical condition is that the step size for the weight of the top element should be larger than the step size for the other weights (but not larger than 10 times to provide stability). Several scenarios demonstrated that our proposed algorithm achieves low computational cost, fast convergence, and good stability. Furthermore, the proposed algorithm maintains the simplicity of the classic LMS with fixed step sizes while compensating (i.e., returning to a low MSE) easily for any disturbance in the system.

The proposed time processing incorporates fixed non-uniform tap delays (i.e., exponential, Rician, Rayleigh, and Gaussian distributions). In contrast to the time-consuming tap delay tracking algorithms, the proposed non-uniform tap delays do not increase the complexity of the signal processing compared to those of the uniformly spaced delays.

Multipath channels, developed by an intense campaign of the DLR, were used to simulate multipath propagation. Using the standardized channel models, it was shown that, for a BER of $10^{-3}$, the system can operate with a 1 to 2 dB lower SNR when an exponential distribution is used, instead of the uniform distribution [50]. Based on these results, it was demonstrated that the exponential distribution is an excellent tradeoff between the simplicity of the uniform distribution and the good performance of the computationally intensive tap tracking algorithms.

To improve the performance of the antenna array, a new microstrip patch design was proposed. The design incorporates a hybrid substrate that includes a ferrite ring around the patch antenna to create a constructive interference in the fields inside the substrate. A ferrite ring, with a permittivity of 10 and a permeability of 14, was initially examined. The distance from the circumference of the ring to the ferrite was selected to be quarter wavelength and the thickness of the ferrite was also set to quarter wavelength. For these parameters, the constructive interference enhances the antenna gain by about 3.5 dB and increases the impedance bandwidth by nearly 1%.

The ferrite was replaced with a dielectric material to analyze the impact of dielectric combinations (instead of ferrite/dielectric). Combinations of different dielectric materials were used, demonstrating that the use of dielectric rings can also enhance the gain of the microstrip patch antenna due to the reflections in the interfaces of the materials. It can be noted that, as the permittivities of the materials increase, the gain enhancement is larger, and as the permittivity of the material of the ring increases, the range of values for the ring width that enhances the gain decreases. However, in these cases, the substrate has to be larger than the one for the ferrite ring due the required ring dimensions to increase the gain.

It was demonstrated that the shape of the ring plays an important role in the dimensions of the optimal geometry. Combinations of square and circular ring and patch were used: square patch with circular ring, circular patch with square ring and square patch with

square ring structures. The results suggested that, as long as the area of the ferrite ring is maintained constant, the gain of the hybrid configuration is similar, regardless the geometry. In addition, the incorporation of anisotropic ferrites demonstrated that the maximum energy aligns along the direction of the largest permittivity component. The highest gain was attained when the highest permeability component is that of the H-plane direction.

It was demonstrated that, for infinite arrays, the scan angle range increases from 55 degrees (in a conventional array) to 90 degrees for the hybrid configuration. This investigation suggests that a tradeoff has to be made between gain and reflection coefficient when using different substrates. The hybrid substrate exhibits an excellent performance by reducing the reflection coefficient as the main beam is scanned, but, due to the losses in the ferrite ring, the gain is also reduced.

## 5.2 Recommendations

The use of GPS systems seems to be growing very rapidly, as nowadays they can be found almost in every cell phone, camera, car, etc. However, as it is discussed in this dissertation, the performance of the GPS receiver can be highly impacted by the environment. Several modifications were proposed in the previous chapters to improve the reception of the desired signal. These modifications can be summarized as:

- Improve the weighting algorithm to null high-power interferences.
- Use non-unform taps or time delay distributions.
- Improve the performance (gain and bandwidth) of the microstrip patch elements by using hybrid substrates.

Based on the results of these proposed modifications, several recommendations for future work are discussed next.

*Time Processing*

In Chapter 3, it was demonstrated that the use of non-uniform taps or time delays can improve the reception of the GPS signal. In particular, the exponential distribution outperforms the uniform without degrading its computational efficiency. The investigation was performed by Monte Carlo simulations using MATLAB and different channels models, including stochastic and channels developed by measurements. Although it has been demonstrated that the Monte Carlo technique is an excellent tool to analyze the performance of communication channels, it is important to use non-uniform taps delays in real-time GPS receivers. This step will help to validate the use of non-uniform tap delays in real environments.

*Microstrip Patch Antennas*

The use of hybrid substrates to increase the gain of GPS antennas was proposed in Chapter 4. It was demonstrated that a significant gain enhancement can be achieved without degrading the bandwidth of the antenna. For future work, guidelines to select the materials and distances should be developed. The guidelines will help to select the appropriate materials and dimensions to attain the desired performance. In addition, validation of the results with experimental data is still required.

The use of hybrid substrates can be expanded to other antenna designs, such as the Planar Inverted F Antenna (PIFA), which is widely used in mobile communications due to its small size (around half of a microstrip antenna). The gain of PIFA is lower than the gain of a conventional microstrip antenna, but the use of hybrid substrates can enhance it. Therefore, the use of PIFA elements with hybrid substrates may lead to a performance similar to that of a conventional microstrip array, but with half of the size. It may be an excellent alternative for military hand-held GPS devices.

*Microstrip Patch Arrays*

The analysis of microstrip patch arrays using hybrid substrates can be expanded to include other ferrites and/or dielectrics. A different dielectric/ferrite combination may lead to low reflection coefficients and high gains. Other antenna elements or ring shapes may also be examined to obtain high gains/low reflection coefficients.

REFERENCES


[1] I. Corvallis Microtechnology. (1996) Introduction to the Global Positioning System for GIS and TRAVERSE. [Online]. Available: http://www.cmtinc.com/gpsbook/

[2] D. Lu, R. Wu, Z. Su, and W. Huang, "A two stage GPS anti-jamming processor for interference suppression and multipath mitigation," in *2007 IEEE Radar Conference*, Apr. 2007, pp. 746–749.

[3] C. A. Balanis, *Antenna Theory: Analysis and Design*. 3rd Edition, John Wiley & Sons, 2005.

[4] Y. Lu, J. Yang, Z.-M. Ding, and Z.-Z. Tan, "The orthogonal weighted algorithm for GPS receiver anti-jamming," in *2001 CIE International Conference on Radar*, 2001, pp. 1190–1194.

[5] W. C. Cheuk, M. Trinkle, and D. A. Gray, "Null-steering LMS dual-polarised adaptive antenna arrays for GPS," *Journal of Global Positioning Systems*, vol. 4, no. 1, pp. 258–267, 2005.

[6] H.-W. Tseng and S. Atterberg, "Small controlled reception pattern antenna (S-CRPA) design and test results," in *26th JSDE Conference*, Oct. 2000.

[7] W. Kunysz, "Advanced pinwheel compact controlled reception pattern antenna (AP-CRPA) designed for interference and multipath mitigation," *Proceedings of the 14th International Technical Meeting of the Satellite Division of The Institute of Navigation (ION GPS 2001)*, pp. 2030–2036, Sept. 2001.

[8] D. S. De Lorenzo, J. Gautier, J. Rife, P. Enge, and D. Akos, "Adaptive array processing for GPS interference rejection," *Proc. ION GNSS 2005*, pp. 618–627, 2005.

[9] C. C. Counselman, "Multipath-rejecting GPS antennas," *Proceedings of the IEEE*, vol. 87, no. 1, pp. 86–91, Jan. 1999.

[10] Z. Fu, A. Hornbostel, J. Hammesfahr, and A. Konovaltsev, "Suppression of multipath and jamming signals by digital beamforming for GPS/Galileo applications," *GPS Solutions*, vol. 6, no. 4, pp. 257–264, 2003.

[11] B. Van Veen and K. Buckley, "Beamforming: a versatile approach to spatial filtering," *IEEE ASSP Mag.*, vol. 5, no. 2, pp. 4–24, April 1988.

[12] M. Casabona and M. Rosen, "Discussion of GPS anti-jam technology," *GPS Solutions*, vol. 2, no. 3, pp. 18–23, 1996.

[13] A. Soloviev and F. Van Graas, "Beam steering in Global Positioning System receivers using synthetic phased arrays," *IEEE Trans. Aerosp. Electron. Syst.*, vol. 46, no. 3, pp. 1513–1522, July 2010.

[14] Y. Zhang and C. Bartone, "Multipath mitigation in the frequency domain," in *2004 Position Location and Navigation Symposium, PLANS 2004*, April 2004, pp. 486–495.

[15] R. Fante and J. Vaccaro, "Wideband cancellation of interference in a GPS receive array," *IEEE Trans. Aerosp. Electron. Syst.*, vol. 36, no. 2, pp. 549–564, April 2000.

[16] J. Proakis, *Digital Communications*. McGraw Hill Higher Education, 2008.

[17] P. Xiong, M. Medley, and S. Batalama, "Spatial and temporal processing of GPS signals," *Proceedings of the Tenth IEEE Workshop on Statistical Signal and Array Processing*, pp. 524–528, 2000.

[18] P. Xiong, M. Medley, and S. Batalama, "Spatial and temporal processing for global navigation satellite systems: the GPS receiver paradigm," *IEEE Trans. Aerosp. Electron. Syst.*, vol. 39, no. 4, pp. 1471–1484, Oct. 2003.

[19] A. Abbott, "Antijamming and GPS for critical military applications." [Online]. Available: http://www.aero.org/publications/crosslink/summer2002/06.html

[20] R. Klemm, *Applications of Space-Time Adaptive Processing*. Institution of Engineering and Technology, 2004.

[21] R. Klemm, *Principles of Space-Time Adaptive Processing*. Institution of Engineering and Technology, 2002.

[22] W. Lijun, Z. Huichang, and Y. Xiaoniu, "Adaptive array antenna for GPS interference mitigation and its performance analysis," in *International Conference on Microwave and Millimeter Wave Technology, 2007*, April 2007, pp. 1–4.

[23] A. Paulraj and C. Papadias, "Space-time processing for wireless communications," *IEEE Signal Process. Mag.*, vol. 14, no. 6, pp. 49–83, Nov. 1997.

[24] T. Moore, "Analytic study of space-time and space-frequency adaptive processing for radio frequency interference suppression," Ph.D. dissertation, The Ohio State University, 2002.

[25] S.-J. Kim and R. Iltis, "STAP for GPS receiver synchronization," *IEEE Trans. Aerosp. Electron. Syst.*, vol. 40, no. 1, pp. 132–144, Jan. 2004.

[26] J. Lambert, C. A. Balanis, and D. DeCarlo, "Spherical cap adaptive antennas for GPS," *IEEE Trans. Antennas Propag.*, vol. 57, no. 2, pp. 406–413, Feb. 2009.

[27] S. Applebaum, "Adaptive arrays," *IEEE Trans. Antennas Propag.*, vol. 24, no. 5, pp. 585–598, Sept. 1976.

[28] S. Applebaum and D. Chapman, "Adaptive arrays with main beam constraints," *IEEE Trans. Antennas Propag.*, vol. 24, no. 5, pp. 650–662, Sept. 1976.

[29] W. Sun and M. Amin, "Maximum signal-to-noise ratio GPS anti-jam receiver with subspace tracking," in *IEEE International Conference on Acoustics, Speech, and Signal Processing*, vol. 4, Mar 2005, pp. 1085–1088.

[30] L. Griffiths, "A simple adaptive algorithm for real-time processing in antenna arrays," *Proceedings of the IEEE*, vol. 57, no. 10, pp. 1696–1704, Oct. 1969.

[31] B. Widrow, P. Mantey, L. Griffiths, and B. Goode, "Adaptive antenna systems," *Proceedings of the IEEE*, vol. 55, no. 12, pp. 2143–2159, Dec. 1967.

[32] O. Frost, "An algorithm for linearly constrained adaptive array processing," *Proceedings of the IEEE*, vol. 60, no. 8, pp. 926–935, Aug. 1972.

[33] P. Anderson, M. Ingram, and J. Goldstein, "The performance of spatial smoothing techniques using the LMS algorithm," in *1994 IEEE Military Communications Conference, 1994. MILCOM '94*, vol. 1, Oct. 1994, pp. 112–116.

[34] D. Lu, R. Wu, Z. Su, and W. Huang, "A space-frequency anti-jamming algorithm for GPS," in *2007 IEEE Antennas and Propagation Society International Symposium*, June 2007, pp. 4216–4219.

[35] R. A. Monzingo and T. W. Miller, *Introduction to Adaptive Arrays*. SciTech Publishing, 2004.

[36] W. Gabriel, "Adaptive arrays; An introduction," *Proceedings of the IEEE*, vol. 64, no. 2, pp. 239–272, Feb. 1976.

[37] B. Widrow, "A review of adaptive antennas," in *IEEE International Conference on Acoustics, Speech, and Signal Processing*, vol. 4, April 1979, pp. 273–278.

[38] H. L. Van Trees, *Optimum Array Processing - Part IV, Detection, Estimation, and Modulation Theory*. John Wiley & Sons, 2002.

[39] F. Gross, *Smart Antennas for Wireless Communications*. McGraw-Hill Professional, 2005.

[40] L. Yan and W. Xinan, "A modified VS LMS algorithm," in *The 9th International Conference on Advanced Communication Technology*, vol. 1, 2007, pp. 615–618.

[41] F. Vook and R. Compton, "The bandwidth performance of linear adaptive arrays with tapped delay-line processing," in *Antennas and Propagation Society International Symposium*, vol. 4, May 1990, pp. 1692–1695.

[42] B. Widrow and M. Hoff, "Adaptive switching circuits," *IRE WESCON Convention Record*, vol. 4, pp. 96–104, 1960.

[43] S. Gelfand, Y. Wei, and J. Krogmeier, "The stability of variable step-size LMS algorithms," *IEEE Transactions on Signal Processing*, vol. 47, pp. 3277–3288, 1999.

[44] S. M. Kay, *Fundamentals of Statistical Signal Processing: Estimation Theory*. Prentice Hall, 1993.

[45] A. Khong, W.-S. Gan, P. Naylor, and M. Brookes, "A low complexity fast converging partial update adaptive algorithm employing variable step-size for acoustic echo cancellation," in *IEEE International Conference on Acoustics, Speech and Signal Processing, 2008. ICASSP 2008*, 2008, pp. 237–240.

[46] M. Godavarti and A. Hero, "Stability analysis of the sequential partial update LMS algorithm," in *2001 IEEE International Conference on Acoustics, Speech, and Signal Processing*, vol. 6, 2001, pp. 3857–3860.

[47] M. Godavarti and A. Hero, "Partial update LMS algorithms," *IEEE Transactions on Signal Processing*, vol. 53, pp. 2382– 2399, 2005.

[48] A. L. A. Steingass, "Measuring the navigation multipath channel," in *ION GNSS 2004*, Sept. 2004, pp. 1157–1164.

[49] A. Rivera-Albino and C. A. Balanis, "Adaptive spherical array with non-uniformly spaced taps for GPS signal processing," in *2011 IEEE AP-S International Symposium on Antennas and Propagation*, July 2011, pp. 2837–2840.

[50] A. Rivera-Albino and C. A. Balanis, "Non-uniform tap spacing in a GPS spherical adaptive array," *IEEE Antennas and Wireless Propagation Letters*, vol. 11, pp. 822–825, 2012.

[51] P. Voois, I. Lee, and J. Cioffi, "The effect of decision delay in finite-length decision feedback equalization," *IEEE Trans. Inf. Theory*, vol. 42, no. 2, pp. 618–621, Mar. 1996.

[52] W. Rodgers and R. Compton, "Adaptive array bandwidth with tapped delay-line processing," *IEEE Trans. Aerosp. Electron. Syst.*, vol. AES-15, no. 1, pp. 21–28, Jan. 1979.

[53] R. T. Compton, "The relationship between tapped delay-line and FFT processing in adaptive arrays," *IEEE Trans. Antennas Propag.*, vol. 36, no. 1, pp. 15–26, Jan. 1988.

[54] C.-C. Yeh, Y. Hong, and D. Ucci, "Use of the tapped delay line adaptive array to increase the number of degrees of freedom for interference suppression," *IEEE Trans. Aerosp. Electron. Syst.*, vol. 23, no. 6, pp. 809–813, Nov. 1987.

[55] R. T. Compton, "The bandwidth performance of a two-element adaptive array with tapped delay-line processing," *IEEE Trans. Antennas Propagat.*, vol. 36, pp. 5–14, 1988.

[56] S. Qureshi, "Adjustment of the position of the reference tap of an adaptive equalizer," *IEEE Trans. Commun. Technol.*, vol. 21, pp. 1046–1051, 1973.

[57] S. Raghavan, J. Wolf, L. Milstein, and L. Barbosa, "Non-uniformly spaced tapped-delay-line equalizers," *IEEE Trans. Commun.*, vol. 41, pp. 1290–1295, Sept. 1993.

[58] S. Raghavan, J. Wolf, and L. Milstein, "On the power of non-uniformly spaced tapped-delay-line equalizers," in *1990 Conference Record Twenty- Fourth Asilomar Conference on Signals, Systems and Computers*, vol. 2, Nov. 1990, p. 696.

[59] I. Lee, "Optimization of tap spacings for the tapped delay line decision feedback equalizer," *IEEE Commun. Lett.*, vol. 5, pp. 429–431, Oct. 2001.

[60] C. Niessen and D. Willim, "Adaptive equalizer for pulse transmission," *IEEE Trans. Commun. Technol.*, vol. 18, pp. 377–395, 1970.

[61] D. George, R. Bowen, and J. Storey, "An adaptive decision feedback equalizer," *IEEE Trans. Commun. Technol.*, vol. 19, pp. 281–293, 1971.

[62] "Satellite navigation multipath channel models." [Online]. Available: http://www.kn-s.dlr.de/satnav/

[63] C. A. Balanis, *Advanced Engineering Electromagnetics*. 2nd Edition, John Wiley & Sons, 2012.

[64] P. Bevelacqua and C. Balanis, "Optimizing antenna array geometry for interference suppression," *IEEE Trans. Antennas Propag.*, vol. 55, no. 3, pp. 637–641, Mar. 2007.

[65] P. Bevelacqua and C. Balanis, "The influence of array geometry on system performance," in *IEEE Antennas and Propagation Society International Symposium 2006*, July 2006, pp. 3327–3330.

[66] M. Lu, J. Wang, R. Babu, D. Li, and Z. Feng, "A novel antenna array for GPS/INS/PL integration," *Journal of Global Positioning Systems*, vol. 4, pp. 160–165, 2005.

[67] M. Reese, C. Balanis, C. Birtcher, and G. Barber, "Modeling and simulation of a helicopter-mounted antenna using WIPL-D," in *IEEE Antennas and Propagation Society International Symposium, 2009. APSURSI '09*, June 2009, pp. 1–4.

[68] D. Pozar and D. Schaubert, "Scan blindness in infinite phased arrays of printed dipoles," *IEEE Trans. Antennas Propag.*, vol. 32, pp. 602–610, 1984.

[69] S. Zavosh, "Analysis of circular microstrip patch antennas backed by circular cavities," Master's thesis, Department of Electrical, Computer and Energy Engineering, ASU, 1993.

[70] D. Sievenpiper, "High-impedance electromagnetic surfaces," Ph.D. dissertation, Department of Electrical Engineering, UCLA, 1999.

[71] H. Boutayeb, T. Djerafi, and K. Wu, "Gain enhancement of a circularly polarized microstrip patch antenna surrounded by a circular mushroom-like substrate," in *2010 European Microwave Conference (EuMC)*, Sept. 2010, pp. 1734–1737.

[72] H. Boutayeb, T. A. Denidni, K. Mahdjoubi, A. C. Tarot, A. R. Sebak, and L. Talbi, "Analysis and design of a cylindrical EBG-based directive antenna," *IEEE Transactions on Antennas and Propagation*, vol. 54, pp. 211– 219, 2006.

[73] J. Bell and M. Iskander, "Effective propagation properties of an enhanced hybrid ebg/ferrite ground plane," *IEEE Antennas Wireless Propag. Lett*, vol. 7, pp. 74–77, 2008.

[74] J. Bell and M. Iskander, "Equivalent circuit model of an ultrawideband hybrid ebg/ferrite structure," *IEEE Antennas Wireless Propag. Lett*, vol. 7, pp. 573–576, 2008.

[75] Y. Liu, C. G. Christodoulou, P. F. Wahid, and N. E. Buris, "Analysis of frequency selective surfaces with ferrite substrates," in *Antennas and Propagation Society International Symposium*, Jun. 1995, pp. 1640–1643.

[76] L. Greetis and E. Rothwell, "A self-structuring patch antenna," in *IEEE Antennas and Propagation Society International Symposium*, Jul. 2008, pp. 1–4.

[77] L. Yang, L. Martin, D. Staiculescu, C. P. Wong, and M. M. Tentzeris, "Comprehensive study on the impact of dielectric and magnetic loss on performance of a novel flexible magnetic composite material," in *European Microwave Conference (EuMC)*, Oct. 2008, pp. 131–134.

[78] A. HFSS, ver. 14.0.0, ANSYS, Canonsburg, PA, USA, 2011. [Online]. Available: http://www.ansys.com

[79] M. D. Deshpande and M. C. Bailey, "Analysis of finite phased arrays of circular microstrip elements," *IEEE Trans. Antennas Propag.*, vol. 37, pp. 1355–1360, 1989.

[80] D. Pozar, "Finite phased arrays of rectangular microstrip patches," *IEEE Trans. Antennas Propag.*, vol. 34, pp. 658–665, 1986.

[81] M. C. Bailey and M. D. Deshpande, "Analysis of elliptical and circular microstrip antennas using moment method," *IEEE Trans. Antennas Propag.*, pp. 954–959, 1985.

[82] A. Rivera-Albino and C. A. Balanis, "Gain enhancement in microstrip patch antennas using hybrid substrates," *IEEE Antennas Wireless Propag. Lett.*, vol. 12, pp. 476–479, 2013.